ADDIS ABABA UNIVERSITY
COLLEGE OF NATURAL AND COMPUTATIONAL SCIENCES
SCHOOL OF EARTH SCIENCES

FLOOD DETECTION AND MAPPING USING MICROWAVE REMOTE SENSING; A CASE STUDY ON LAKE KOKA CACHMENT, AWASH RIVER BASIN, ETHIOPIA

A Thesis Submitted to

The School of Graduate Studies for Partial Fulfillment of the Requirements for Degree of Masters of Science in Remote Sensing and Geo-informatics

BY
GETU TESSEMA TASSEW
(GSR /0473/2008)

Advisor
Dr. Binyam Tesfaw

Addis Ababa University
JULY, 2017

FLOOD DETECTION AND MAPPING USING MICROWAVE REMOTE SENSING; A CASE STUDY ON LAKE KOKA CACHMENT AWASH RIVER BASIN, ETHIOPIA

A THESIS SUBMITTED TO THE SCHOOL OF GRADUATE STUDIES FOR PARTIAL FULFILLMENT OF THE REQUIREMENTS FOR DEGREE OF MASTER OF SCIENCE IN REMOTE SENSING AND GEO-INFORMATICS

BY

GETU TESSEMA TASSEW

(GSR /0473/2008)

Addis Ababa University

JULY, 2017

Addis Ababa University

School of Graduate Studies

This is to certify the thesis prepared by Getu Tessema entitled as "***Flood Detection and Mapping using Microwave Remote sensing; a case study on Lake Koka catchment Awash River basin, Ethiopia***" is submitted in partial fulfilment of the requirements for the degree of master of science in Remote Sensing and Geo-informatics compiles with the regulations of the university and meets the accepted standards with respect to originality and quality.

Signed by the examining committee:	Signature	Date
Dr. Binyam Tesfaw Advisor	_______________	/__________________
Prof. Tigistu Haile Chairman	___________________	/________________
Dr. Seyfu Kebede Examiner	___________________	/______________
Prof. Tigistu Haile Examiner	___________________	/______________

Addis Ababa University

JULY, 2017

ACKNOWLEDGMENTS

I express my deep sense of gratitude and indebtedness to my thesis advisor Dr. Binyam Tesfaw, School of Earth Sciences, Remote Sensing and Geoinformatics stream, Addis Ababa University, for his guidance and valuable suggestions, comments, helpful discussions and appreciations during my research work.

I would like to express my sincere thanks to European Space Agency (ESA) for providing me with the free SAR data to carry out the research work.

It is my great pleasure to present my thankfulness to architect planner Lealem Berhanu, Deputy Manager of Addis Ababa City Planning Project Office (ACPPO) for his benevolence of my academic improvement. It was unique for me that you were courageous and optimist. I hearty thank you. I am very thankful to Architect Tamirat Eshetu, senior architect planner, ACPPO, for letting me concentrate on my thesis work for the time being. Thank you for your helps and encouragement. Without your cooperation, I would not have completed this thesis in time. I am also very thankful to ACPPO staffs. I am especially grateful to thank Saba Mekonin, Esayas Teshome and Mahilet for their consistent help and encouragement. I really proud of you.

I am greatly indebted to my beloved Mariya for her helpful appreciations and financial support throughout my assignment. I also glad to thank my sister Agere (JiJi) for her help.

The great gratitude must have to go to the school of Earth Sciences, Addis Ababa University that provided me with the necessary facilities during my thesis work. I would like to thank Ethiopian Meteorological Agency for providing me the necessary data for my research work.

I also wish to thank the Geological Survey of Ethiopia for the generous cooperation of providing the important geological data. The last but not least thank goes to all my families and friends, whose names could not be mentioned separately because of limitations; for their constant encouragement and cooperation.

Getu Tessema

July, 2017

TABLE OF CONTENTS

Contents **Pages**

LIST OF TABLES

LIST OF FIGURES

LIST OF APPENDICES

Pages

ACRONYMS

AMRSA	Active Microwave Remote Sensing
CADS	Calibration Annotation Dataset
CCRS	Canadian Center for Remote Sensing
CSO	Create Stack Operator
Dd	Drainage density
dB	Decibel
DEM	Digital Elevation Model
DN	Digital Numbers
DWA	Discrete Wavelet Transform
ENL	Equivalent Number of Looks
ENVI	Environment for Visualizing Image
EO	Earth Observation
ERDAS	Earth Resource Data Analysis System
ERS	European Remote Sensing
ESA	European Space Agency
EU	European Union
FAO	Food and Agricultural Organization
GMAP	Gamma Map Aposteriori
GPS	Global Positioning System
GRD	Ground Range Detection
HH	Horizontal transmission and Horizontal reception
HV	Horizontal transmission and Vertical reception
ID	Image Differencing
IDW	Inverse Distance Weighting

IOM	International Organization for Migration
IWS	Interferometric Wide Swath
LULC	Land-Use Land-Cover
LUT	Look Up Tables
MR	Merge
MRS	Microwave Remote Sensing
OCHA	Office for Coordination of Humanitarian Affairs
OLI	Operational Land Imagery
PCD	Principal Component Differencing
PMRS	Passive Microwave Remote Sensing
RADAR	Radio Detection and Ranging
RADARSAT	Radar Satellite
REG	Registration
RGB	Red, Green, Blue
ROI	Region of Interest
SAR	Synthetic Aperture Radar
SEASAT	Seafaring Satellite
SLC	Single Look Complex
SNAP	Sentinel Application Platform
SRTM	Shuttle Radar Topography Mission
TOPSAR	Terrain Observation with Progressive Scans Synthetic Aperture Radar
UN	United Nations
VH	Vertical transmission and Horizontal reception
VV	Vertical transmission and Vertical reception

ABSTRACT

Sentinel-1 is a microwave remote sensing mission providing continuous all-weather and day-night time radar data. The main goal of the present study is to evaluate microwave remote sensing data for flood detection and to develop the flood extent map from a series of radar SAR images. The study area is on Lake Koka catchment, Awash River basin which has an increased agricultural investment interests. This area was frequently affected by flood during the "belg" and summer seasons in 2016 caused by the over flow of Awash River and the flash flood of the surrounding tributary streams. For the present study, Sentinel-1 SAR time series images, covering the same scene but at different times were utilized in order to achieve the research objectives. These images were: i) before flooding i.e. acquired on 22 March, 2016 and ii) after the flood event; acquired on 15 April and 09 May, 2016. The images were de-speckled using various filtering algorisms. After comparison of the image quality based on the algorisms, the gamma map 7×7 kernel size speckle filtering method was selected and used as speckle removal for the study. The backscatter properties of five different feature classes in the context of flood extent extraction were derived from time series SAR images. These feature classes were open water, flooded area, agriculture, vegetation and bare soil. From such backscatter properties of test class features on the SAR image, appropriate change detection threshold value was set by visual interpretation and image histogram analysis. Based on the threshold value the changed and unchanged areas were identified for inundated area delineation. Change detection algorithms were applied to extract the flood extent from the processed SAR images. Of all other change detection methods, the band subtraction, band ratioing and principal component differencing (PCD) techniques were utilized. The results of each technique was compared with one another. The band subtraction and band rationg algorithms showed similar flood extent map. The flood extent extracted from band subtraction method was 24.12 km^2 for 15 April, 2016 and 17.63 km^2 for 09 May, 2016 flood events. The band ratio method has resulted 23.22 km^2 and 17.3 km^2 flood extent of 15 April, 2016 and 09 May, 2016 respectively. The other method, the PCD accounted for 20.67 km^2 area of 15 April, 2016 and 15.7 km^2 of 09 May, 2016 flood extent. The flood extent maps were presented separately for each flood detection method. The SAR images was also used for land-use/land-cover classification with Landsat 8 optical sensor image. Based on these stacked different sensor images, the land-use/land-cover of the study area was classified in to six classes. Theses six land-cover classes were; 1) agriculture field, 2) bare land, 3) irrigated land, 4) water body, 5) settlement and 6) vegetation. The overall classification accuracy was 90% with 0.86 kappa statistics value. Generally, this research has observed that space-born SAR satellite data is an outstanding technology for near real time flood detection and mapping. It provided promising flood extent map that could help in the preparation of flood monitoring and management processes.

Keywords: Microwave remote sensing, Sentinel-1, SAR, Awash River, Change detection, Flood, Backscatter analysis, Speckle filtering

CHAPTER ONE

1. INTRODUCTION

1.1 Background

Natural hazards happen every year and their frequency, intensity and impact seem to have greatly increased in recent decades (Mata and Alvino, 2013). Hazards are natural phenomenon that could have a negative effect on people and the environment. Natural hazards can be grouped into two very broad categories. The first category is the geophysical hazards which encompass the geological and metrological phenomena such as earthquake, volcanic eruption, drought, wildfire and floods (Kusky and Timothy, 2003). And the other category is the biological hazards.

Among the geophysical hazards, floods are the frequent and costly natural geophysical hazards in terms of human and economic loss. Flooding is a global environmental threat causing large amounts of economic loss every year (Jongman, 2014). According to Jongman (2014) annual economic casualties caused by floods may exceed one trillion USD by 2050. By definition flood is a covering of land by water not normally covered with water (EU Floods Directive, 2007 as cited in Giustarini, 2015).

Flood is one of the major natural hazards in Ethiopia that affects lives and livelihoods in different parts of the country. Flooding in Ethiopia is mainly linked with torrential rainfall and the topography of the highland mountains and lowland plains with natural drainage systems formed by the principal River basins (Daniel, 2007). Topographically, Ethiopia is composed of highlands and lowlands which bring nine drainage systems, of which originate from the centrally situated highlands and make their way down to the peripheral or outlying lowlands. In most cases floods occur in the country as a result of prolonged heavy rainfall causing Rivers to overflow and inundate areas along the River banks in lowland plains (Wubet, 2007).

A threatening flood hazard has been occurred in different parts of the country that brings extensive damages to human lives, economy and environment in the year 2016. International Organization of Migration (IOM, 2016) announced that around 120,000 people or 19,557 households have been displaced since the start of the Belg rainy seasonof 2016. The affected regions include Afar (with 671 households), Amhara (420), Harari (287), Oromiya (5,322), SNNP (2,972) and Somali (9,885 households). The UN Office for the Coordination of Humanitarian Affairs (OCHA, 2016) also reported that almost 20,000 families have been displaced by exceptional and extensive flooding across the country from the current “Belg/ spring’’ rains.

One of the important problems associated with flood monitoring is a real time flood extent extraction and mapping since it is impractical to acquire the flood area through field observation (Kussul et al., 2008). Thus, the efficient monitoring of floods and risk management is impossible without the use of Earth Observation (EO) data from space. Flood monitoring and mapping using (EO) data can help authorities and non-governmental organizations in disaster management and coordination of humanitarian efforts (Schlaffer et al., 2014).

Previously, few researches have been conducted on flood detection and risk assessment in Ethiopia which were entirely based on optical remote sensing (e.g. Wubet, 2007 ; Daniel, 2007). However, optical remote sensing which operates in the visible, infrared or thermal range of the electromagnetic spectrum has limitations in detecting floods under thick cloud cover during the rainy time.

Microwave remote sensing on the other hand, offers some clear advantages in the field of real time flood monitoring. The active imaging microwave instrument provides its own source of illumination in its spectrum range (Bakker et al., 2001). Unlike optical sensors, it is characterized by near all-weather and day-night acquisition capabilities as the microwave signal is able to penetrate clouds and the imaging process is independent from solar radiation (Alexandridis et al., 2010). Microwave sensor capabilities strongly enhance the monitoring of frequency (six days) and therefore the near real-time utilization for emergency situations. This technology provides new potential for flood detection and mapping.

The European Space Agency (ESA) developed a SAR system called the Sentinel-1 mission that was designed as a two polar-orbiting satellite constellation. These satellites are Sentinel-1A and Sentinel-1B that were launched on April 3, 2014 and 22 April 2016, respectively. The Sentinel-1 mission provides an independent operational capability for continuous radar mapping of the Earth. It was designed to provide enhanced revisit frequency, coverage, timeliness and reliability for operational services and applications (ESA, 2013). These capabilities of the SAR system has now attracted many researchers in the field of flood monitoring and management.

1.2 Statement of the Problem

The ever increasing flood hazard entails due attention to manage and control its frequent impact on the lives and the economy of Ethiopia. Conventional hydrological monitoring systems such as River gaging, flood intensity map etc. have limited use in flood forecasting, mapping, and emergency response. For large countries like Ethiopia, the cost of maintaining rain and stream gauging stations is a limiting factor (Klemas, 2015). This leads to a 'must use' of other innovative technologies and clear technical methods such as remote sensing (satellite image analysis) rather than a traditional ways that has been involved in flood extent mapping.

Several researches have been conducted on flood extent mapping using satellite derived information specifically using optical remote sensing, which is using visible and infrared wavelength of electromagnetic radiation. These optical remote sensing data are the preferred data for flood mapping due to their straightforward interpretability and rich information content (Sandro, 2010). They have been frequently used in the past to derive inundation areas (Klemas, 2015).

However, as flooding often occurs during long-lasting precipitation and persistent cloud cover periods, in many cases, a systematic monitoring using optical imaging instruments was not successful in detection real time flood events (Sanyal and Lu, 2004). This is because of the influence of clouds, precipitation and water vapor during the raining season. In addition to this, as flooding conditions are relatively in a very short time duration or sudden event, it needs a frequent revisit time from the sensors of remote sensing technologies. Therefore, microwave remote sensing enables the possibilities to monitor floods during almost under all weather conditions and at day - night with considerably at a short revisit time comparing with the images from optical remote sensing sensors (Mason et al., 2014). The Synthetic Aperture Radar (SAR) sensor that is mounted on radar satellites like the Sentinel-1 can acquire images in all-weather conditions and penetrate clouds and as well heavy rain. The SAR system has also a short revisit time (six days) that is important to capture the flooding incidence. These facts drastically decrease the regular usability of optical sensors in an operational rapid flood detection and mapping. Therefore, due to the difficulties of the in-situ observations and less capabilities of the optical remote sensors to detect the flood occurrence at a time of bad weather, it is important to use a stand-alone all-weather capable microwave remote sensing to detect the near real-time flood events and map its extent.

1.3 Research Objectives

1.3.1 General Objective

The main objective of this research is to develop a flood extent map from a time series of SAR images for specific flood event of Lake Koka catchment Awash River basin, Ethiopian Rift Valley.

1.3.2 Specific Objectives

The specific objectives of the research were:

- Evaluating the application of microwave remote sensing data (SAR) for flood extent mapping
- Identifying a real-time flood event and map its extent using microwave remote sensing for Lake Koka catchment of Awash River basin.
- To verify flood extent map using ancillary data sets

1.4 Research Questions

1. Are SAR data applicable to flooding detection?
2. Which areas in the Awash River of Lake Koka catchment were flooded and are prone to future flooding?
3. Is the microwave remote sensing method robust in extracting flood events from time series of SAR images?

1.5 Scope of the Study

The study is intended to evaluate microwave remote sensing technology application in the flood management as it is the only stand-alone technology for near real-time flood detection during bad weather condition. The study covers the smaller area of Awash River basin of the Lake Koka catchment. The aim was to apply the methods and procedures for larger area in advance. However, this might require some further development of the methodology as the study area will then be more heterogeneous. This thesis only focused on the smaller area and tried to optimize the methods applicable for that specific area using SAR satellite data.

1.6 Limitation of the Study

The major limitations concerned to this study were the data availability at the relevant acquisition mode and the specific time of flood occurrence. The first limitation was that, the used imagery was VV (Vertical transmission and Vertical reception) polarization which is subjected to the effect of diffuse reflection by vegetation on the flooded area than the HH (Horizontal transmission and Horizontal reception) polarization. Although VV polarization is promising to detect flood particularly in rural areas, it is highly detectable by HH transmission and reception method than the VV polarization due to the horizontal nature of flood water. Therefore, because of unavailability of HH polarization during the time of flood occurrence on the study area, the study was limited to the use of VV polarization of radar signal recording system.

Secondly, as flooding stays for a short period of time, the on target availability of the radar sensor to record the occasion at that particular time is highly important. In the case of the present study the available data was shortly after hours which resulted discontinuity of the flooded area that may has resulted the missed flooded area and reduce the total flood affected area which can be detected.

1.7 Thesis Chapters Outline

This thesis is composed of five Chapters. The First Chapter is about introduction to the subject and presents the statement of problem, research objectives, scope and limitation of the study. Chapter Two gives an overview of microwave remote sensing as a field of study for flood management and the theory behind the methods used in flood detection and mapping. It also introduces the previous studies' techniques applied in the study of flood detection. Chapter Three presents the methods and materials applied and used in the study. It gives detail description about the study area, the datasets that were used in the study and the overall explanation of the methodologies that were applied to conduct the different experiments of the research. Chapter Four explains the results and discussion, which mainly introduces the results of preprocessed and the post-processed findings primarily leading to flood extent mapping of the study area. Finally, Chapter Five gives conclusion and recommendations about future works related to flood hazard monitoring in the field of microwave remote sensing.

CHAPTER TWO

2. LITERATURE REVIEW

2.1 Microwave Remote Sensing

Remote sensing is a technique to observe the earth surface or the atmosphere from space using satellites (space borne) or from the air using aircrafts (airborne). Remote sensing uses a part or several parts of the electromagnetic spectrum. It records the electromagnetic energy reflected or emitted by the earth's surface (Aggarwal, 2013).

A remote sensing, either airborne or space borne using microwave radiation with wavelength from about 1centi meters to 1metres that enables observation in all weather conditions without restriction by cloud or rain is a microwave remote sensing-MRS (Fig.2.1a). The MRS has a less sensitive signals to clouds and rainfalls (Fig.2.1b). It has a longer wavelength radiation which can penetrate through cloud cover, haze, dust, and all but the heaviest rainfall (CCRS, 2013). The MRS can also operate both at night and day, independent of sun illumination.

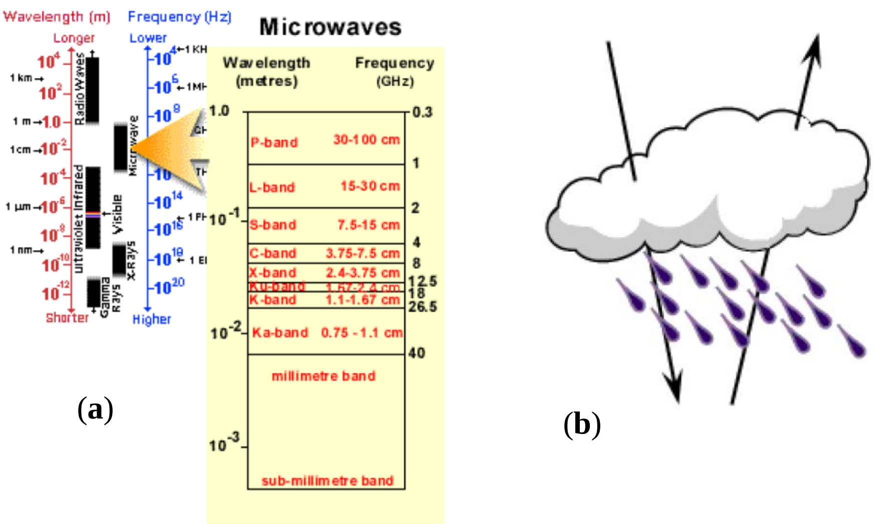

Figure 2.1: **a**) Electromagnetic spectrum of microwave and **b**) the microwave radiation that penetrates the cloud and rainfall (CCRS, 2013).

The MRS encompasses both active and passive forms of remote sensing. A passive microwave sensor detects the naturally emitted microwave energy within its field of view. This emitted energy is related to the temperature and moisture properties of the emitting object or surface (O'Neill et al., 1996). The passive microwave remote sensing (PMRS) illustrated in Fig. 2.2, records the energy (1) emitted from the atmosphere, (2) reflected from the Earth Surface, (3) emitted from the surface and (4) transmitted from the subsurface.

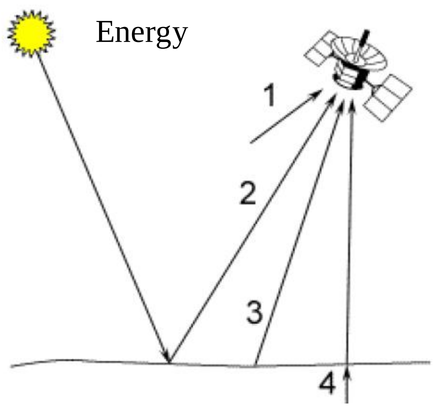

Figure 2.2: Passive microwave remote sensing. (CCRS, 2013).

In the case of active microwave remote sensing the sensors provide their own source of energy to illuminate the target. They are not depend on external energy source rather providing themselves.

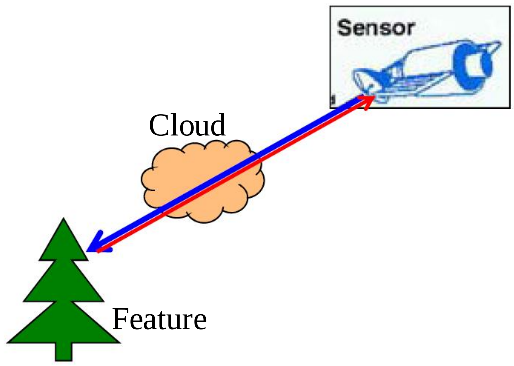

Figure 2.3: Active microwave remote sensing, (CCRS, 2013).

Active microwave remote sensors (AMRS) are generally grouped in to two. The first one is imaging active microwave sensors. In this category, the most common form of imaging active microwave sensor is the radar. Radar stands for RAdio Detection And Ranging. This sensor transmits a microwave (radio) signal towards the target and detects the backscattered portion of the signal. The second group is non-imaging active-microwave remote sensing. As opposed to imaging sensors these group of sensors are two dimensional representations.

The active MRS uses the scattering properties of the terrains and targets for analysis of the data obtained and differentiating one target from the other. The scattering properties are manifested in the scattering coefficient of the target. Scattering coefficient is a function of the angle of incidence, the frequency of operation and polarization. It also depends on the electrical properties of the target like dielectric constant and conductivity as well as on the physical properties like texture, surface type, etc. Radar is the common microwave remote sensing technology. In the active MRS the two important parameters, i.e., capability to produce very high resolution imagery and to measure the distance/altitude with high accuracy are very imperative aspects to be exploited (Calla, 2013).

Applications of Microwave Remote Sensing

Microwave remote sensing has various applications. As countries economy growth has now encounter many natural and human induced problems, the MRS has ample potential to help the economy growth and solve problems (Calla, 2013). The broad applications of microwave remote sensing are for land, ocean and atmosphere. It can also be used for study of the different target properties on Earth. This technique has been successfully used for study of natural materials like soil, water and snow on the Earth. Different land based applications that can be studied are flood mapping, soil moisture estimation, crop identification, snow studies, geology, forestry, urban land-use, etc.

The powerful microwave sensors provide virtually real-time day-night and all-weather coverage of land surfaces and bodies of water in the globe. The radar mission enables the implementation of many operational services and scientific monitoring (Arianespace, 2016) in a variety of areas. The area of applications could also be surveillance of maritime ice, icebergs, icecaps; maritime surveillance (including detection of oil pollution), the sea state (waves, wind and currents); agriculture; forestry; hydrology; as well as the highly accurate detection of ground movement for applications related to subsidence, volcano monitoring, the analysis of earthquakes, etc. They are also highly useful in atmospheric water vapor and temperatures, vegetation classification and stress in the hydrological characteristics, and management of emergencies, such as flooding (Carver et al., 1985).

2.2 RADAR

RAdio Detection And Ranging (RADAR) is an imaging active microwave sensor. According to Bhattacharya (2014), it has three basic functioning systems. It transmits microwave signals towards the scene; receives the portion of the transmitted energy backscattered from the illuminated target and observes the strength (detection) and the time delay of the return signal by which the distance of an object from the sensor can be calculated. These functions are also defined in similar ways by Jenn (2015), such that the distance or rang is from pulse delay, velocity from doppler frequency shift and angular direction from antenna pointing. The amount of power reflected (scattered) back to the radar antenna can be quantified using the radar equation (Skolnik, 2008). It is given as:

$$p_r = \frac{\pi^3 p_t g^2 \theta \varphi h |K|^2 \, l \, z}{1024 \ln(2) \, \lambda^2 r^2} \quad (2.1)$$

where;

Pt = power transmitted by radar (watts)

Pr = power received back by radar (watts)

g = gain of the antenna (ratio of power on the beam axis to power from an isotropic i.e., radiating equally in all directions (antenna) at the same point); it is a measure of how focused the radar beam is.

θ = horizontal beamwidth (radians)

φ = vertical beamwidth (radians)

h = pulse length (meter)

$|\kappa|$ = dielectric constant for hydrometeors; usually taken as 0.93 for liquid water, 0.197 for ice.

l = loss factor for attenuation of radar beam, varies between 0 and 1, usually near 1. Since the attenuation of the beam is often unknown, it is often ignored.

λ=wavelength of radar pulse (meter)

r = range or distance to the target (i.e., the distance to an area of position that reflects the originally transmitted pulse back to the radar).

Z = radar reflectivity factor (mm^6/m3) and can be expressed as

$$\mathrm{z} = \sum_{v0l} D^6 \qquad (2.2)$$

Where D is the drop diameter and the summation is over the total number of drops (of varying sizes) within a unit volume of the beam; in the equation it gets multiplied by the radar volume defined by the beam width, height, pulse length and distance from the radar. The radar is usually mounted on a flying platform such as an airplane or a satellite and operates in a side looking geometry with an illumination perpendicular to the flight line direction. It emits microwave radiation to the ground and measures the electromagnetic signal backscattered from the illuminated area.

2.2.1 Radar Imaging Geometry

The antenna of the radar illuminates a surface trip to one side of the nadir track. The direction to where the platform moves is an azimuth direction. The direction that the radar transmits and receives radiation is called the range (CCRS, 2013). The radar transmits the microwave beam to the ground continuously with a side-looking angle (θ) in the direction perpendicular to the flying track- azimuth direction (Fig. 2.4).

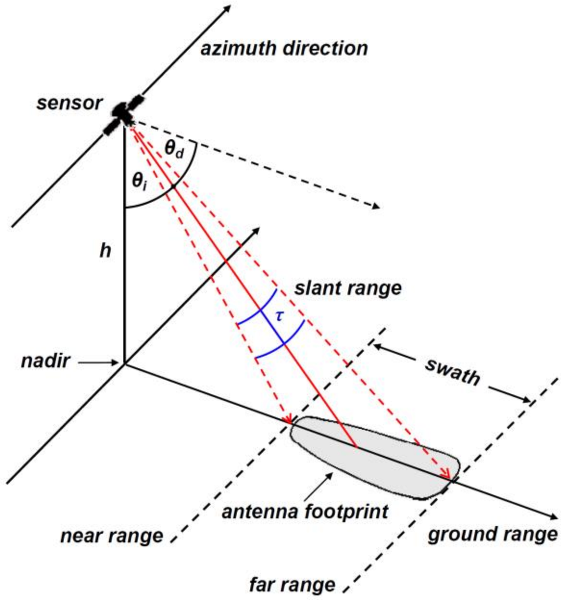

Figure 2.4: Radar imaging geometry (CCRS, 2013).

Radar imagery has different geometry than that produced by most conventional remote sensors system. Therefore, it is important to be careful when attempting radargrammetreic measurements. Uncorrected radar imagery is displayed in what is called slant-range geometry, i.e. is based on the actual distance from the radar to each of the respective features in the scene. It is important to convert the slant- range display into true ground range display on the x-axis so that features in the scene are in their proper planimetric (x, y) position relative to one another in the final radar image.

2.2.2 Synthetic Aperture Radar (SAR)

Synthetic aperture radar is an active microwave remote sensing instrument which can provide high-resolution images of the Earth's surface during both at day and night and virtually under all- weather conditions (Sanyal and Lu, 2004). It is side-looking radar system that makes a high-resolution image of the earth's surface. It is a radar which moves along its path and accumulates data. In this way, continuous strips of the ground surface are "illuminated" parallel and to one side of the flight direction. The across-track dimension is referred to as "range". Range is the distance between the radar and the target surface in the direction perpendicular to the flight. There are two ranges: The near range edge which is closest to nadir (the points directly below the radar); and the second is the far range where its edge is farthest from the nadir (Skolnik, 2008). The along-track dimension is referred to as azimuth.

The fact for the need of SAR is that, there is a physical limit to the length of the antenna, the aperture that can be carried on an air craft or satellite (Buchele, 2006). And on the other hand, shortening of the wavelength has its limitations in penetrating the cloud. Therefore, an approach in which the apertures increase synthetically is applied. One possibility is to increase pulse duration to transmit sufficient energy to receive a certain backscattered energy. However, a long pulse, corresponds to a narrow bandwidth which results in a poor range resolution. Thus, in order to have a high detection ability and a high resolution, a pulse with characteristics of large τ(pulse length) and large B (band width) is needed (Vanzyl, 2006). This is possible in SAR technology, i.e. using several backscattered signals including the same object to simulate a very long antenna.

Moving along its path, the radar illuminates one side of the flight direction (Fig. 2.5), with continuous strips parallel to each other and accumulates information from reflected microwaves (signals). The signal is recorded on board, properly processed to form a digital image. The aim of SAR signal processing is to synthesize a 2-D high spatial resolution image of the earth's surface reflectivity from all the received signals (Akbari, 2013).

Radar uses time delay to separate signals from different objects. The range to each object is determined by the time delay between when the pulse was transmitted and received. If there are two objects at different ranges, the time difference between receiving the two pulses is given by the formula (Vanzyl, 2006):

$$\Delta t = 2\Delta R / c \tag{2.3}$$

where: Δt - time difference

ΔR - distance between targets

c - Speed of light (300,000 kilometers per second)

The synthetic aperture radar techniques exploit the motion of the radar in orbit to synthesize a typically about 10 km long antenna in the flight direction (Carver et al., 1985). While the radar is traveling along its path, it is sweeping the antenna's footprint across the ground while it is continuously transmitting and receiving radar pulses. In this scenario, every given point in the "radar swath" is imaged many times by the moving radar platform under constantly changing yet predictable observation geometries (Skolnik, 2008). The SAR defeats the intrinsic resolution limits of radar antennas in the along-track direction. In the cross-track or range direction, orthogonal to the satellite path, the resolution is not defined by the antenna beam width, but rather the width of the transmitted pulse (Fig. 2.5). This is because the transmitted pulse intersects the imaged surface as it propagates in the beam (Ibid, 2008).

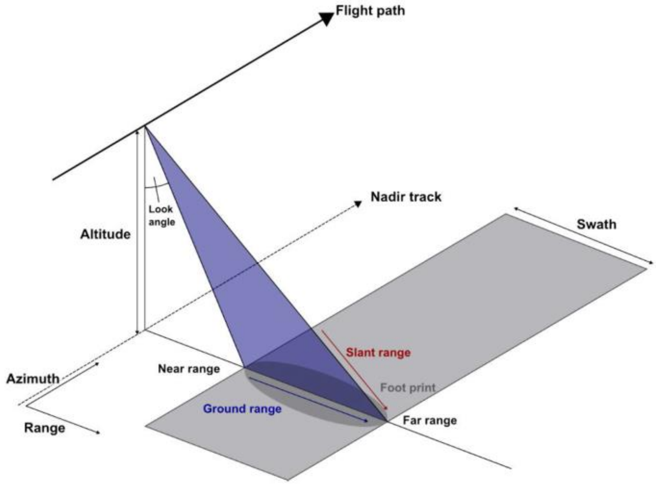

Figure 2.5: The SAR signal recording system (ESA, 2007).

The platform moving along the azimuth direction provides the scanning. The area scanned by the antenna beam is called the radar swath. An antenna, mounted on a platform, transmits a radar signal (Fig. 2.6a) in a side-looking direction towards the earth's surface. The reflected signal, known as the echo (Fig. 2.6b), is backscattered from the surface and received in a fraction of a second later at the same antenna (sarmap, 2009).

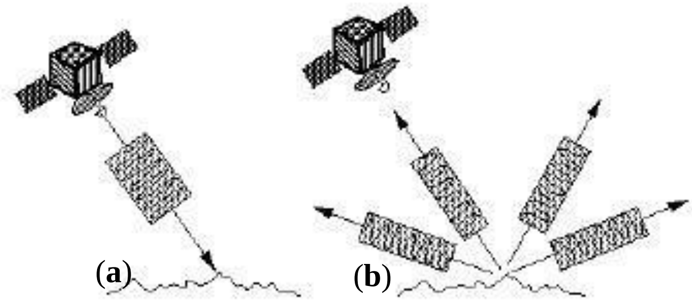

Figure 2.6: **a)** The incoming and **b**) the Backscattering of SAR pulse from the target area (sarmap, 2009).

In the SAR, the amplitude and the phase of the received echo which are used during the focusing process to construct that image are recorded. Aperture is used to collect the reflected energy to form an image. In the case of radar imaging this is the antenna. The resolution of the SAR images is limited fundamentally by the bandwidth of the transmitted pulse (Skolnik, 2008). For instance, a wide bandwidth can be achieved by a short duration pulse, however, the shorter the pulse, the lower the transmitted energy and the poorer the radiometric resolution. To preserve the radiometric resolution, SAR systems generate a long pulse with a linear frequency modulation (Sarmap, 2009).

2.2.3 Synthetic Aperture Radar Spatial Resolution

The resolution of a radar image for earth observation is defined by the azimuth resolution in the flying direction and the ground range resolution in the range direction (Akbari, 2013). Resolution of a SAR sensor should not be confused with pixel spacing which results from sampling done by the SAR image processor (Toan, 2007). Range resolution of a SAR is determined by built-in radar and processor constraints which act in the slant range domain. Range resolution is dependent on the length of the processed pulse. For example, shorter pulses result in "higher" resolution. This is the ability of the radar to distinguish two targets in the range direction.

Therefore, resolution is expressed as the minimum distance that two scatter points must have in order to be discriminated. The slant and ground range resolutions of SAR (Fig. 2.7) can be calculated using pulse duration (τ), sine of look angle (θ) and speed of light (c). If an infinitely short pulse is transmitted toward a point target at a distance 'R' away, an infinitely short echo will be received at time $t = 2R/c$ (Akbari, 2013). Thus two targets are resolved if their returns do not overlap. In this regard the shortest separation between two objects which can be referred as the slant spatial resolution is given as follow (Van, 2006; Sharma, 2006; Akbari, 2013).

$$\delta_\gamma = \frac{c\tau}{2} = \frac{c}{2B} \qquad (2.4)$$

where; δ_γ shortest distance between two targets

B - represents the band width of the signal and τ is the pulse length

2 - represents the fact that the radar signal travels two times the distance R.

c - the speed of light.

If it is to be projected onto the ground (ground resolution) with incidence angle θ_i (Fig. 2.7) the resolution is calculated by;

$$\delta g = \frac{\delta_\gamma}{sin\theta i} = \frac{c\tau}{2 sin\theta i} \qquad (2.5)$$

The smallest time difference that the radar can distinguish is the effective pulse length (τ) and the smallest distance below which two point targets cannot be distinguished in the final image is range resolution. Thus, in order to achieve a resolution as high as possible, a short pulse or a wide bandwidth pulse is required. The energy in a pulse is equal to;

$$E = P\tau \qquad (2.6)$$

Where P is the instantaneous peak power. The energy in a pulse characterizes the capability of the pulse to detect a target, and a high pulse energy is desired. This can be obtained by increasing the peak power P.

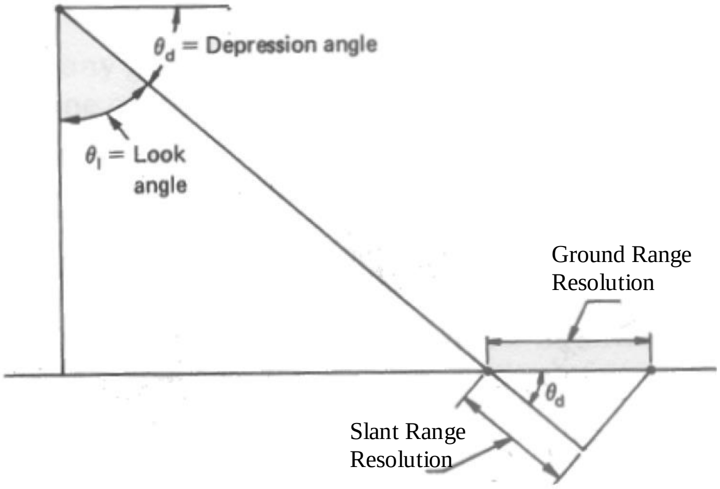

Figure 2.7: SAR resolution (CCRS, 2013).

Radar data are created in the slant range domain, but usually are projected onto the ground range plane when processed into an image. The ground range resolution is coarser than the slant range resolution. This is because of that when the multi look in slant range is converted into a detected product in ground range, the resolution reduces from its multi look high resolution level (CCRS, 2013).

2.2.4 Polarization of SAR Signal

Irrespective of wavelength, radar signals can transmit horizontal (H) or vertical (V) electric field vectors, and receive either horizontal (H) or vertical (V) return signals, or both. The basic physical processes responsible for the like-polarized (HH or VV) return are quasi-specular surface reflection. For instance, calm water (i.e. without waves) appears black. The cross polarized (HV or VH) return is usually weaker, and often associated with different reflections due to, for instance, surface roughness (sarmap, 2009).

When an electromagnetic wave travels in space, the electric field vector describes an ellipse in the plane of the wave (Ibid, 2009). This ellipse defines the state of polarization, which refers to the spatial orientation of the plane of oscillation of the electric field that can be oriented vertically, horizontally or at some other angles. They are described as plane waves or linear waves when it is horizontal or vertical polarization.

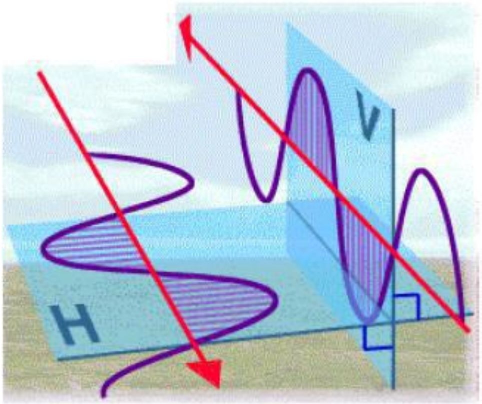

Figure 2.8: Polarization of SAR signal (Vilches, 2013).

The polarization of a SAR instrument refers to the orientation of the transmitted SAR beam's electric field vector. In case of the vector oscillating in the horizontal direction, the beam is said to be "H" polarized. In case of oscillation perpendicular/vertical to the horizontal direction, the beam is known as "V" polarized. The possible combinations of Polarization in microwave remote sensing are: horizontal transmission and horizontal reception (HH), vertical transmission and vertical reception (VV), horizontal transmission and vertical reception (HV) and vertical transmission and horizontal reception (VH) (sarmap, 2009).

2.2.5 Synthetic Aperture Radar Local Incidence Angle

The incidence angle (θ_i) is defined as the angle formed by the radar beam and a line perpendicular to the surface. Microwave interactions with the surface are complex, and different reflections may occur in different angular regions. Returns are normally strong at low incidence angles and decrease with increasing incidence angle. Sentinel-1 satellite data is collected at view angle ranging from 29.1º to 46.0º (Liu, 2016). The sarmap (2009) described local incidence angle as the angle between the normal of the backscattering element and the incoming radiation. The gray tones correspond to the angle and achieve the brightest tones in areas close to shadow (Fig. 2.9). The darkest tones corresponds to areas close to lay-over and shadow which are not significant in the present study area as it has relatively homogeneous topography. The local incidence angle map is used to calculate the effective scattering area (A).

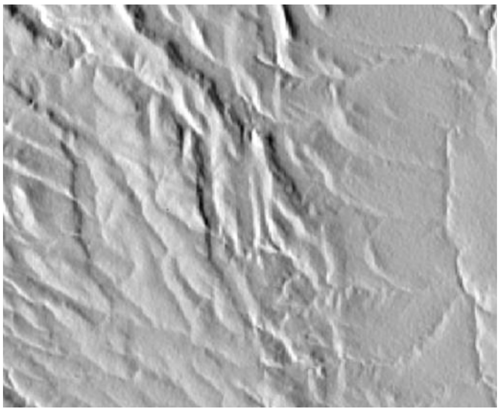

Figure 2.9: SAR local incidence angle (picture: derived from the present study area).

2.3 Microwave Remote Sensing for Flood Detection and Mapping

One of the natural phenomena in the hydrological cycle is flooding. Conventional hydrological monitoring systems have limited use in flood forecasting mapping, and emergency response (Klemas, 2015). For large countries like Ethiopia, the cost of maintaining rain and stream gauging stations can be a limiting factor. Stations mal-functionality can also cause gaps in the hydrographic time series data recording. Rivers are often shared between regions and/or states and as well countries, but information on floods in upstream regions is not always communicated to downstream regions (Ibid, 2015).

Remote sensing techniques have been used to measure and monitor the areal extent of flooding. The availability of multi-temporal near real time satellite data allows monitoring of flooding over large area. Since the launch of the first radar satellite, seafaring satellite (SEASAT) in 1978, microwave sensors have increasingly been used for flood delineation. The two European remote sensing satellite, ERS-1 and ERS-2 were launched in 1991 and 1995, respectively (Chang, 2016). More recently a number of SAR sensors with high resolution as fine as 3meters or higher are available for both urban and rural flood mapping studies, such as RADARSAT-2(C-band), TerraSarX-X-band, COSMO-SkeyMed X-band satellites and sentinels C-band, (Ibid,2016). After a major flood catastrophe, precious information is the delineation of the affected areas. Thus, remote sensing imagery, especially synthetic aperture radar is the better way that allows obtaining a global and complete view of the situation (Morsier et al., 2012). The "before " and "after" flood RADARSAT images are necessary for wide-area flood extent mapping (Pradhan, 2009). Mapping of water surface such as flood using SAR is possible because the backscatter is very low due to the specular reflection when the water surface is smooth (Kudahetty, 2012; Mason et al., 2015). Flood areas appear dark in relation to land surface that has a bright tonal appearance because of the rough soil surface and vegetation. Dry land surface and vegetation produce diffused reflection resulting strong backscatter to the SAR sensor.

The time series SAR images covering two inundation conditions allow evaluating backscatter variations between flood periods and normal water level using different wavelengths. As Sandro (2015) defined that, the flat water surface acts as a specular reflector which scatters the radio energy away from the sensor. Since the sensor receives a low backscatter signal, water appears dark in the images compared to the backscatter signals from vegetation or other land surfaces. Compared to water, microwaves incidence on a rough surface are scattered in many directions which is known as diffuse reflection (Fig. 2.10 c) and result in a brighter tone on the radar imagery (Chang, 2016). This reflection is common in rough surface, vegetation cover and urban areas (Fig. 2.10 b) where double bouncing also occurs in the microwave returning pulse (echo).

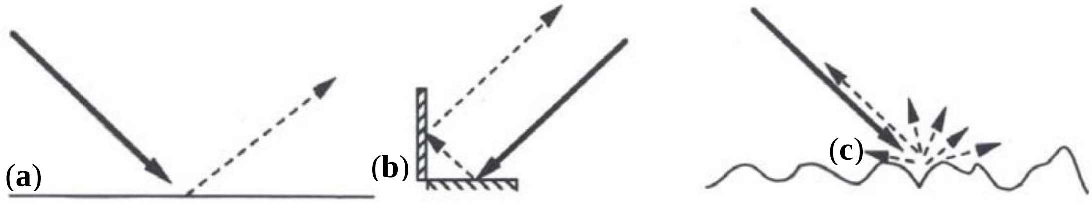

Figure 2.10: **a**) Specular reflection, **b**) double bounce reflection and **c**) diffused reflection (CCRS, 2013).

As sentinel-1 SAR can provide different polarization modes, previous studies conclude that the polarization data HH and VV gave the most informative result for flood mapping. The single polarization HH can also be used for flood mapping better than VV due to that the VV-polarized signal is more sensitive to ripples and waves. However the VV polarization is also promising for flood mapping (Chang, 2016). Many methods have been utilized to detect flood from SAR images. Generally these methods can be grouped into two. The single-image analysis which is performed without considering the change that happens over time for that specific area. As Chang (2016) indicated, single-image analysis can be applied with visual interpretation, image texture analysis, and histogram thresholding and edge detection to detect flooded areas. The other is using multi-temporal images which include before, after and post flood event images by a technique of change detection.

2.3.1 Synthetic Aperture Radar Change Detection with respect to Flood Area Delineation

Detecting regions of change in multiple images of the same scene taken at different times is of widespread interest due to a large number of applications (Prasad and Ravikumar, 2014). Flood detection is one of the areas in disaster management and monitoring applications of SAR remote sensing.

Flood area detection through change detection method usually uses different time series SAR images. Change detection is the process of identifying differences in the state of the object or phenomenon by observing it at different times (Lu et al., 2004). The goal is to identify the set of pixels, or to detect regions of change that are significantly different. It is a technique that identifies changes by analyzing images obtained from the same geographical area at different times. The change detecting in the regions of same area at different periods is of great interest

(MerinAyshu et al., 2013). Change information obtained may be either in the form of simple binary change (i.e. change and no change as in the case of image differencing, image rationing etc.) or detailed from-to change as in the case of using post-classification comparison (Im et al., 2007 as cited in Devi and Jiji, 2015).

There are various types of changing features. Depending on origin and duration of change, they can be categorized into several families of applications, such as land use monitoring, like deforestation or urbanization; land cover monitoring, like detecting the changes in vegetation; and damage mapping, like localization of changes happened due to natural disasters like floods, or earthquake which are usually considered as fast changes (Abubakr et al., 2013). There are different change detection techniques which are applied on SAR images to detect and map the flood extent (Al-doski et al., 2013).

2.3.1.1 Classification based Change Detection

The classification technique which has generally two basic methods is one of the SAR change detections. It passes through post-classification and pre-classification processes. The Post-classification change detection takes place after classification into land-cover or land-use. In post-classification change detection, the classification results of two images are compared. Therefore, the accuracy of post-classification change detection is strongly dependent on the accuracy of classification (Dekker, 2008). Pre-classification techniques operate on the change before classification with the focus of non-coherent change detection techniques (Abubakr et al., 2013). In pre-classification change detection, constant false alarm rate (CFAR) detection, adaptive filtering, multi-channel segmentation and hybrid methods can be applied. The first and the second method are based on the ratio image, which is obtained by dividing the after flood image by the before flood image.

2.3.1.2 Wavelet Fusion Change Detection

Wavelet Fusion is another change detection technique. Image fusion is the technique that combines information from multiple images of the same scene taken over different time intervals (Krishnamal et al., 2013). The result of image fusion is a new image that shows the most desirable information and characteristics of each input image. Image fusion techniques mainly take place at the pixel level of the source images.

Multi scale transform, such as the discrete wavelet transform (DWT) has been extensively used for the pixel-level image fusion. It isolates frequencies in both space and time, allowing detail information to be easily extracted from images. Its simplicity and its ability to preserve image details with point discontinuities make the fusion scheme based on DWT suitable for the change detection task. In order to restrain the unchanged areas and enhance the changed areas, contourlet fusion approach is used for producing the difference image. Among the fusion methods, fusion based on contourlet transform for producing difference image is an edge preserving image fusion method (Merin et al., 2013). This method can provide fused image with better visual quality.

2.3.1.3 Image Differencing based Change Detection

The fused or stacked images can be applied to a mathematical algorism to produce difference image with a technique called image differencing. Image differencing (ID) results in positive and negative values where changes have occurred and zero values on areas where there are no changes (Lu et al., 2004).

Image differencing brings a residual image which represents the change resulting from subtraction of differently dated images. Pixels of small radiance change are distributed around the mean, while pixels of large radiance change are distributed in the tails of the distribution (Singh, 1986 as cited in Berberoglu and Akin, 2009).The difference image algorithm is simple and able to produce a black and white image with very dark areas having extreme negative pixel values and very bright areas having extreme positive pixel values, which represent areas of change (Singh, 1989 as cited in Brown et al., 2000).

2.3.1.4 Histogram Thresholding

Thresholding is a simple and most spread technique of change detection (Bayati and Zaart, 2013). It is one of the most frequently used techniques in active remote sensing to segregate flooded areas from non-flooded one in a radar image (Sanyal and LU, 2004). It is based on classification of image pixels into object and background depend on the relation between the gray level value of the pixels and the threshold.

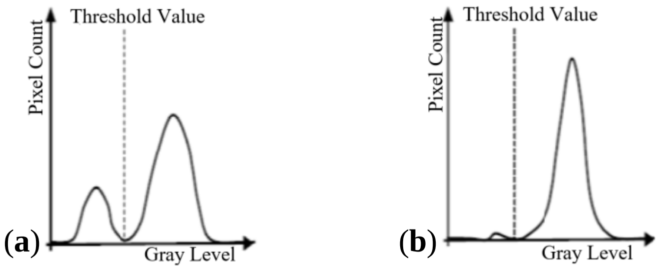

Figure 2.11: Optimal thresholding selection in gray-level histogram: **a**) bimodal and **b**) unimodal histogram (Bayati and Zaart, 2013).

The threshold value of radar backscatter is set in decibel (dB) and a binary algorithm is followed to determine whether a given raster cell is ‘flooded’ or not. It is a point where the changed and unchanged area of a SAR image pixels are discriminated.

2.3.1.5 Principal Component Differencing

Principal Component Differencing (PCD) is the other change detection method used in both SAR and other sensor images (Al-doski et al., 2013).The first principle component (PC1) contains most of the data variance between all the bands which in general is the spatial information. The PCA1 of t_1 and PCA1 of t_2 SAR time series images are frequently used to change detection application.

The present study used the image differencing, principal component differencing and image rationing approaches of change detection dedicated to flood mapping study, i.e., to discriminate the flooded area from the other land surfaces (permanent water and other dry surface).

2.4 Flood Affected Areas in Ethiopia by 2016

Since April, 2016 heavy spring/belg rainfall has caused floods and landslides, resulting in 100 deaths as of 12 May, 2016. The statistics by OCHA (2016), showed that up to 120,000 people have been displaced in six regions. The most affected regions were Somali, Oromia, Southern Nations, Nationalities, and Peoples (SNNP), Afar, Amhara, and Harari which have been already severely affected by the El Niño drought. Table 2.1 below showed the flood affected population in six regions of Ethiopia.

Table 2.1 Flood affected regions by April and May, 2016 (CIA Factbook 2015 cited in OCHA, 2016).

Affected Areas	Resident population	People displaced by floods since April 2016
Somali	5,300,000	50,000
Oromia	27,000,000	27,000
SNNP	14,900,000	15,000
Afar	1,600,000	3,000
Amhara	17,200,000	2,100
Hareri	210,000	1,400
Total six Regions	**66,210,000**	**120,000**

CHAPTER THREE

3. MATERIALS AND METHODS

3.1 Description of the Study Area

3.1.1 Location

The study area for this research is on the Awash River in Lake Koka catchment. It is located in the Central Ethiopian Rift Valley situated between approximately 38º34′30″−39º6′0″E of Longitude and 8º10′30″−8º31′30″N of Latitude (Fig.3.1). It is characterized by different geological, geomorphological, soil and climatic conditions. The study area is mainly defined by floodplain areas in the Awash River at the Lake Koka catchment.

The present study focused on this area as it was hit by the flood hazard that happened in April 15 and May 9, 2016 by over flowing of Awash River and the flash flooding of the surrounding Rivers in the catchment.

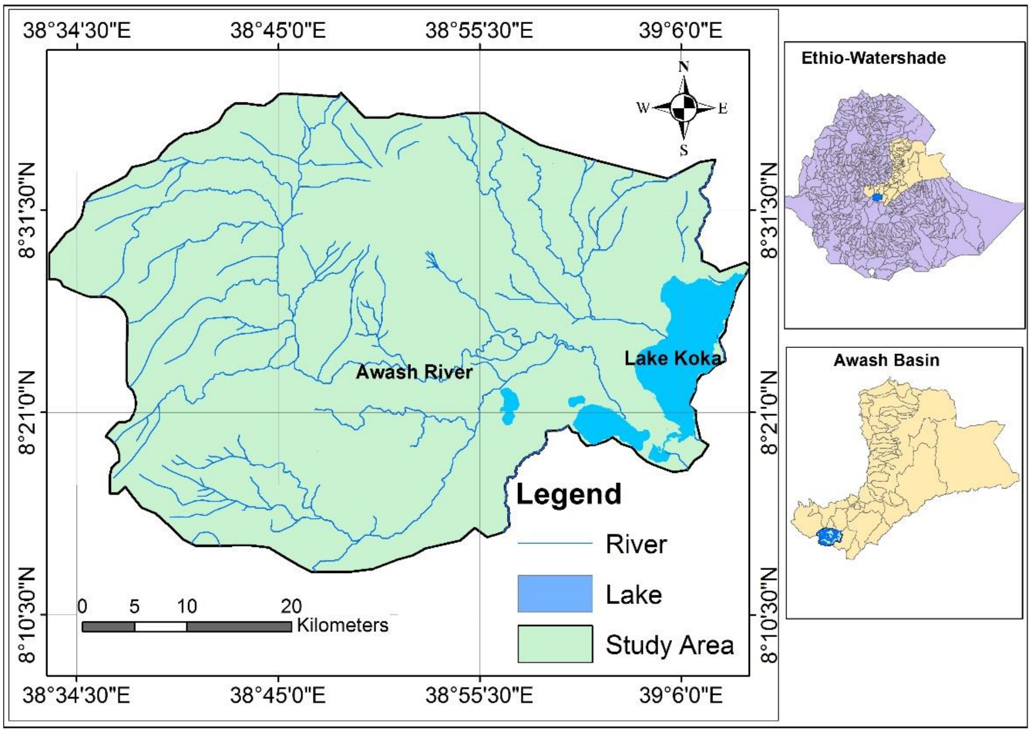

Figure 3.1: Location map of the study area.

3.1.2 Geomorphology

The region is characterized by a relatively wide flat terrain. The elevation of the area decreases downward to the low land region of the Lake Koka from the escarpment of its surrounding (Fig.3.2). The elevation ranges from 1600 at the Lake area up to 3086 meters high at the pick of Ziquala Mountain.

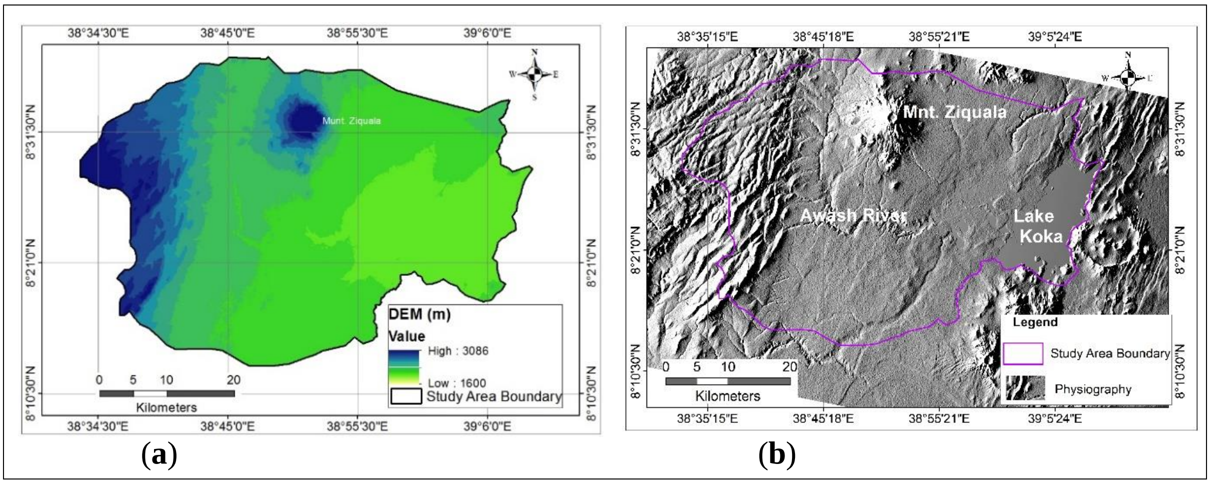

Figure 3.2: **a**) Elevation and **b**) physiography of the study area.

The area has also relatively lower slope (Fig.3.3). It ranges from 0−69 per cent. For the present study purpose it was reclassified in to two categories i.e., from 0–3º and 3–69º. The threshold slope 3º (degree) was used to mask out areas which are not prone to flooding. Usually the actual flood-prone areas may lie lower this threshold (Zwenzner and Voigt, 2009).

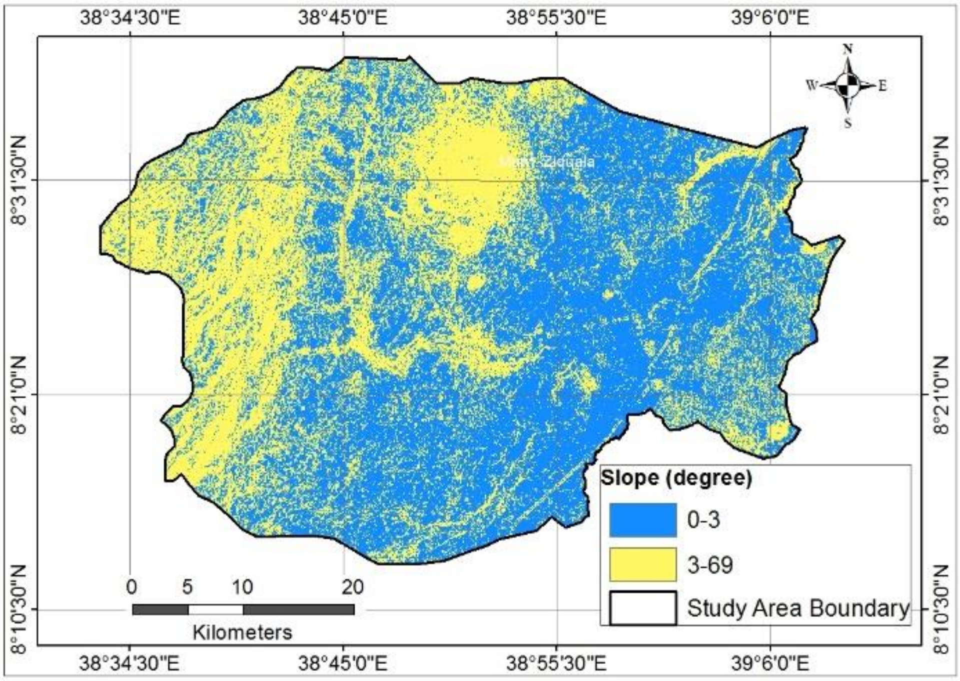

Figure 3.3: Reclassified slope of the study area.

3.1.3 Geology and Soil of the Study Area

3.1.3.1 Geology

Lacustrine sediments in the floodplains and basaltic lava flows at the eastern top lands to the Awash River escarpment slopes dominate the geological setting of the area. The geology of is broadly classified into prerift volcanics, late tertiary volcanos, quaternary volcanics/wonji group and quaternary deposits.

According to the geological survey of Ethiopia (2010), the main rock types which characterize the geology of the area are Precambrian gneiss, Mesozoic sediments, paleogene fissural flood basalts with minor rhyolites, trachyte and pyroclastic flows. It has also Pleistocene-Holocene basic to felsic volcanics and magmatic deposits interrelated with lacustrine and alluvial deposits (Fig.3.4).

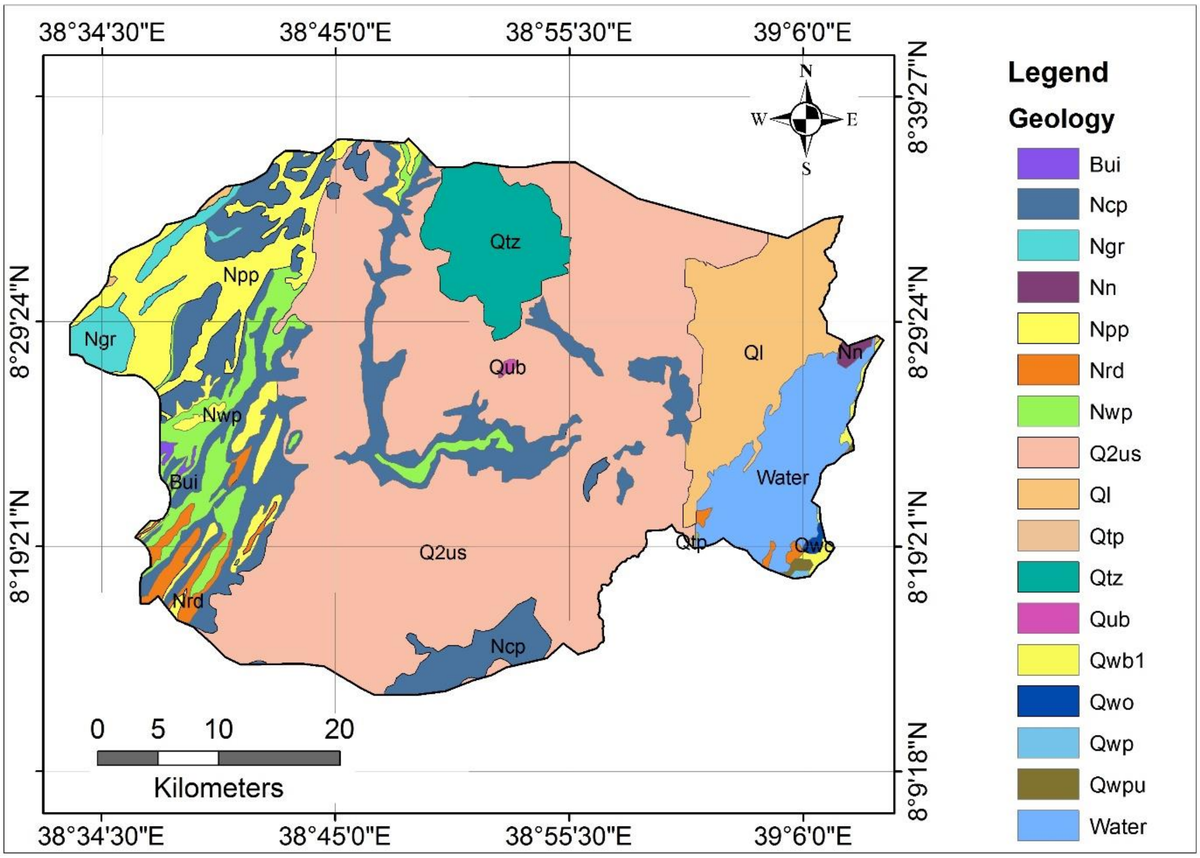

Figure 3.4: Geology of the study area.

The lacustrine sediments cover the largest portion of the low lands of the present study area. The pyroclastic deposits laid to the west part along the Awash River as well as the trachytes of ziquala are also the main geological settings of the area. The description of the geological codes are given below in Table 3.1.

Table 3.1 Geology code description of the study area (Geological Survey of Ethiopia (2010).

Geology Code	Description
Bui	pyroclastic deposits
Npp	Babich-Guder basalts
Ncp	Chefe donsa pyroclastic Deposits
Ngr	Gash megal phyolites
Nn	Anchar Basalts and rhyolites
Nrd	Phyolitic and Trachytic flows
Nwp	Welded to partially welded pyroclastic flows
Q2us	Lacustrine sediments
Ql	Lacustrine sediments and basaltic flow
Qtp	Phyric basaltic flow
Qt2	Zikuala trachytes
Qub	Basaltic lava flows
Qwb1	Trachytic lava flows
Qwo	Obsidias and pitchstones
Qwp	Trachyte and per alkaline rhyolite ignimbrites
Qwpu	Pumic and unwelded tuffs, centeral volcanos

3.1.3.2 Soil

Soils have a major influence on hydrological processes. Their physical properties govern the storage and transmission of water within the soil (Boorman et al., 1995). Soils have different rainwater retaining capacity. This capacity is dependent on the soil type and their texture. Flooding problems will occur even where there is no heavy rainfall if the soil in an area will not hold enough rainwater (Hurstcalderone, 2016). According to the soil data from geological survey of Ethiopia (2010), the study area has 11 major soil types including Lake Surface (Fig.3.5). The dominant soil type is luvic phaezems which covers 33.64% of the soil in the area. It is about 709.49 km^2 area followed by vitric cambisols that accounts 384.09 km^2 area (Table 3.2). The soil type with the least area coverage is vertic andosols that covers 4.76 km^2 (0.97%).

Table 3.2 Major soil type area coverage and proportion.

Soil Type	Area(km^2)	Proportion (%)
Luvic Phaeozems	709.49	33.64
Vertic Cambisol s	384.09	18.21
Chromic Vertisols	200.56	9.51
Eutric Cambisols	198.00	9.39
Eutric Fluvisols	175.50	8.32
Lithosols	162.27	7.69
Pellic Vertisols	104.59	4.96
Eutric Nitosols	17.19	0.86
Mollic Andosol	10.24	0.49
Vitric Andosols	4.76	0.23
Lake	142.34	6.75
Total	**2109.08**	**100**

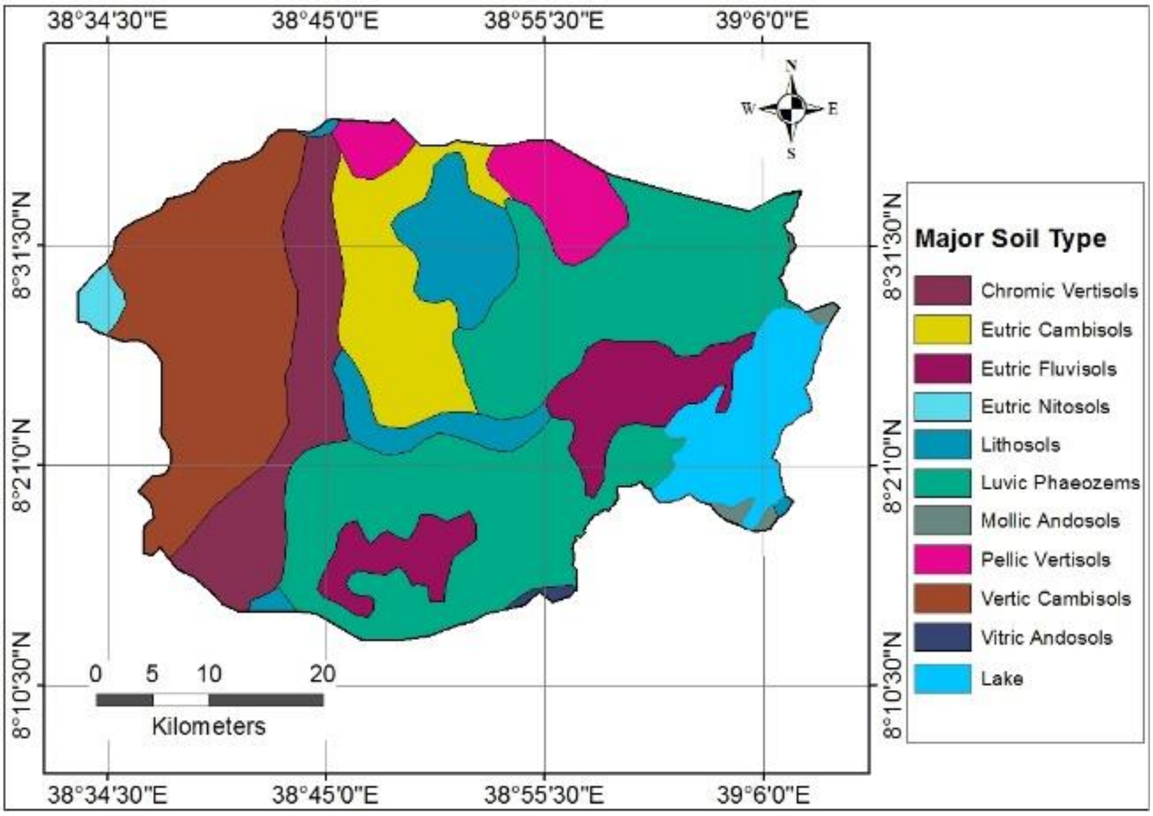

Figure 3.5: Major soil types on the study area (Geological Survey of Ethiopia, 2010).

The soil type and its permeability plays a very crucial role in flood management. The rate of rainfall infiltration can be also affected by soil texture, a commonly used indicator of soil permeability. The soil type area coverage and proportion is depicted in Figure 3.6.

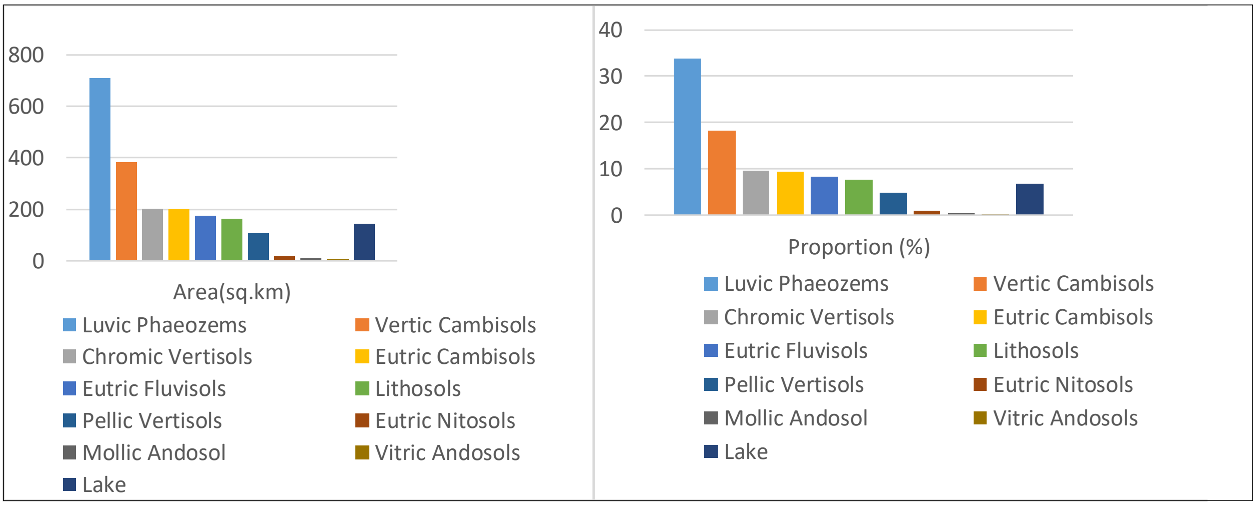

Figure 3.6: Major soil type and area proportion (Geological Survey of Ethiopia, 2010).

According to UNDA soil textural classes, the study area has four dominant soil textures. The clay, clay loam, loam and sandy loam. Clay loam soil texture takes the largest proportion (Fig. 3.7) which covers 987.57 km^2 area. The smallest soil textural class of the study area is sandy loam, accounted for 57.80 km^2 area. By definition soil texture is the relative content of particles of various sizes, such as sand, silt and clay in the soil. It is defined by the particles that make up the soil. The soil texture of clay and to a lesser extent silt can result in low infiltration rates and rapid runoff during intense rainfall. Sandy soils, in contrast, permit greater infiltration because of the wider spaces between particles. As a general rule, runoff from intense rainfall is likely to be more rapid and greater with clay soils than with sand (FAO, 2006).

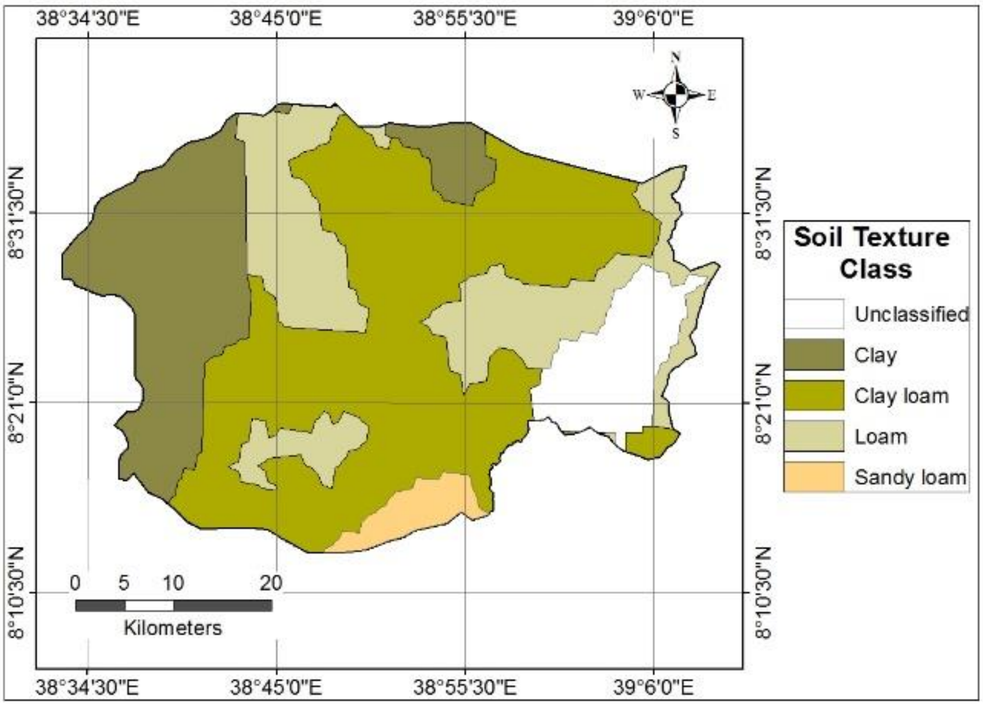

Figure 3.7 Soil texture of the study area (Geological Survey of Ethiopia, 2010).

3.1.4 Climate of the Study Area

The study area is characterized by a semi-arid to sub-humid climate with mean precipitation varying from 600 mm to 1200 mm (Dagnachew and Coulomb, 2003). It has a temperature of 25 °C close to the Lake, and 15 °C on the humid plateaus and escarpment (Ibid, 2003).
In-situ monthly precipitation data for five rainfall stations have been collected from National Meteorology Agency of Ethiopia. The rainfall stations collected were for the 2014, 2015 and 2016 years. According to the rainfall records of these stations, the year 2014 rainfall distribution, where all the rain gauge stations were functional, was nearly with its normal distribution. Where as in the year 2015 and 2016 extreme pick rainfall values were recorded in Meki and Nazret stations respectively (Fig. 3.8).

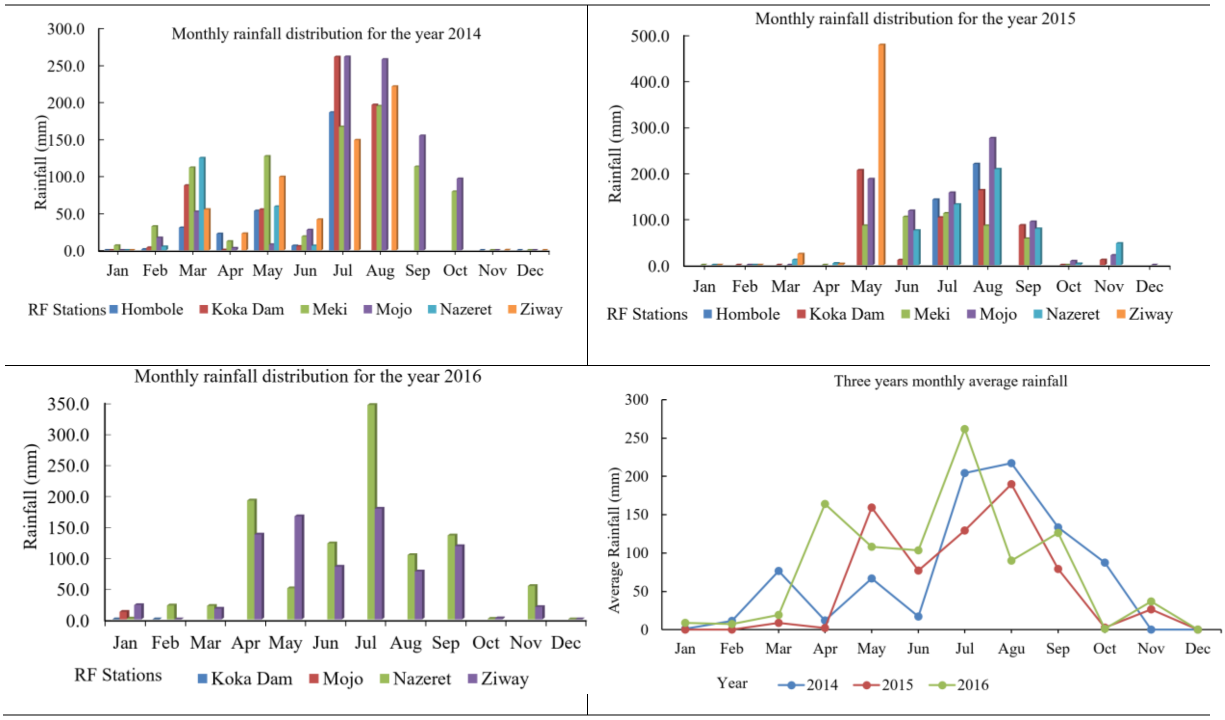

Figure 3.8: Rainfall (in mm) distribution of the study area.

The amount of the rainfall occurred in April and May was unusually highest in the year 2015 of the month May and in the year 2016 both April and May recorded highest value of rainfall. However, the functional rainfall stations were only Nazret and Ziway for the aforementioned rainfall amount record. This year was the time when flood was happening in different parts of Ethiopia on these particular months. The study area was also hit by flood event in April and May by the year 2016.

The rainfall distribution illustrated in Figure 3.9 for the study area was interpolated for un-sampled values from the observed or recognized point (rain gages) values. According to

Charles and Degr´e (2011), spatial interpolation is generally carried out by estimating a regionalized value at un-sampled points from a weight of observed regionalized values. The general formula for spatial interpolation is:

$$Zg = \sum_{i=1}^{ns} (\lambda_i z_{si}) \tag{3.1}$$

Where; Zg is the interpolated value at point g,

Zsi is the observed value at point i,

ns is the total number of observed points (rain gages) and

$\lambda = \lambda i$ is the weight contributing to the interpolation.

The interpolating method used in the present study was inverse distance weighting (IDW). This method estimates values at unsampled points by the weighted average of observed data at surrounding points. Inverse distance weighting relies on the theory that the unknown value of a point is more influenced by closer points than by points those further away (Charles and Degre, 2011).

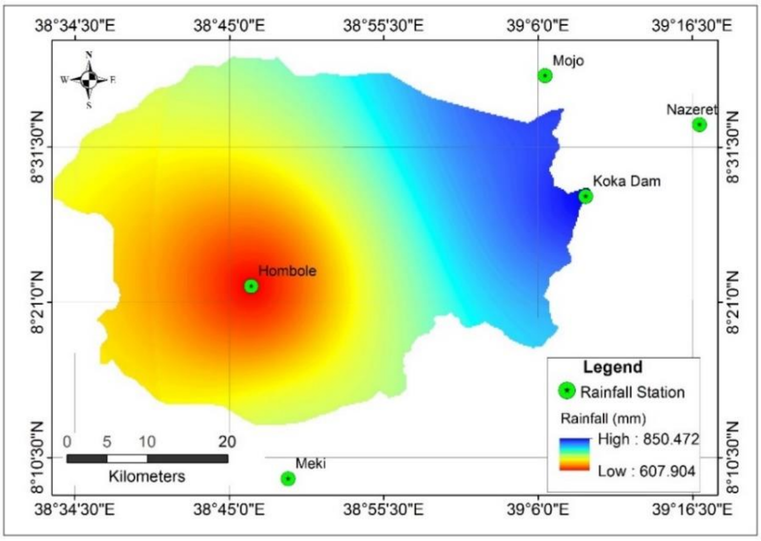

Figure 3.9: Rainfall stations and interpolated rainfall distribution.

Table 3.3 Location of rainfall stations in the study area.

Station Name	Latitude	Longitude	Elevation
Hombole	38.77483	8.36816	1743
Koka dam	39.4542	8.46933	1618
Mojo	39.10817	8.60533	1763
Meki	38.817	8.151	1662
Nazret	39.28333	8.55	1622

3.1.5 Drainage of the Study Area

Drainage is a process that streams and Rivers flow into a point of destination usually a sea or a Lake. The drainage pattern of the study area is a dendritic at the lower part towards the Lake Koka with parallel tributaries in the north western part. It has a drainage density (D_d) of 0.349 km^{-1}. This value is calculated as the total length of all the streams and Rivers in a drainage basin divided by the total area of the drainage basin/watershed.

$$Drainage\ Density(Dd) = \frac{total\ length\ of\ the\ stream}{total\ area\ of\ the\ drainage\ basin} \tag{3.2}$$

It is a measure of how well or how poorly a watershed is drained by stream channels (Pallard et al., 2009). Drainage density depends upon both climate and physical characteristics of the drainage basin. Soil permeability (infiltration difficulty) and underlying rock type affect the runoff in a watershed. Impermeable ground or exposed bedrock will lead to an increase in surface water runoff and therefore to more frequent streams. The value D_d (0.349) seems that the drainage density of the study area is not as such high.

Therefore, a decreasing D_d generally implies decreasing flood volumes (Pallard et al., 2009). However, there are factors contributing to the lower value of drainage density. Among others, the geology of the area such that a reduced D_d can be attributed to the presence of impervious rocky hill slopes, and therefore reduced storage volumes and resulted high flood peaks (Pallard et al., 2009). This is the characteristics of the study area. The area consists of hill slops of impervious basaltic rocks to its west and north western part where there is relatively high drainage network (Fig. 3.10).

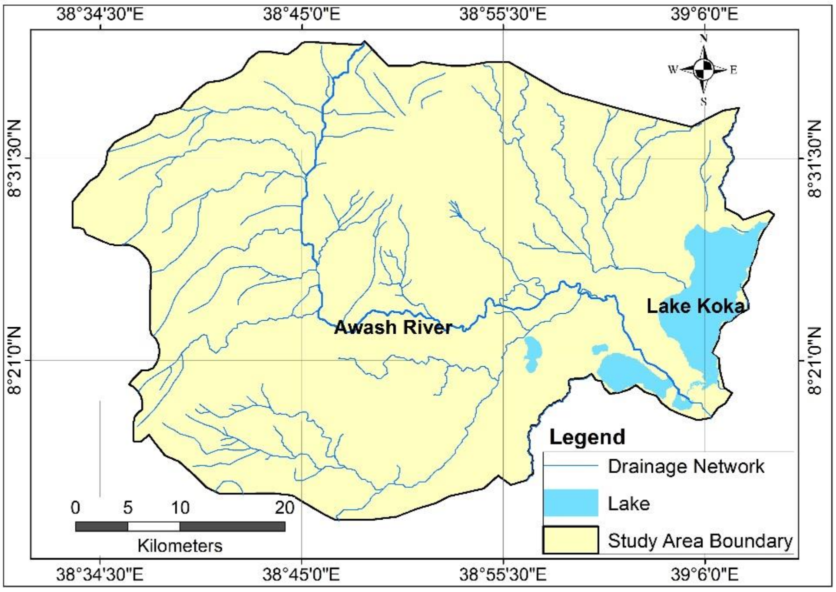

Figure 3.10: The drainage network of the study area.

The hilly and lower plain nature of the area towards the Lake Koka region results in the high velocity of the stream flow which affects concentration time and therefore causes the peak flow magnitude to its lower part of the study area. Besides such factors, the main cause of flood in the study area is the over flow of Awash River which drains from the western highlands of Ethiopia. Awash is the major River in the study area with its tributaries from the hill slopes of the surrounding catchments to the Lake Koka. The tributary Rivers drain from the high land areas of West and North West parts of the study area. The total drainage length accounts to 735.69 km flowing on the total basin area of 2109.12 km^2.

3.1.6 Land-use/Land-cover

Information regarding to the land-use/land-cover is essential in flood management as an initial step of planning for the flood impact monitoring. On the base of this, the land-use/land-cover classification for the study area was performed. This classification was based on two types of satellite data. These were the SAR microwave sensor and the Landsat8 optical sensor images. The images were preprocessed separately and stacked together for the ease of the land-use/land-cover classification of the study area. Supervised land-use/cover classification method was used for the present study. This classification method is a technique for extracting information from image data. The goal is to classify pixels in an image into different classes based on features of the pixels. In the supervised land class classification, there were two stages. The first one was preparing training or sample vectors of each land cover class. This is called training stage. Each training sample vector is made up of the class, the pixel belongs to and feature values of that pixel. The second was the classification stage where the trained classifier was used to group or classify the pixels with known feature but unknown class. After the classification process the unknown classes were assigned to the respective land-cover type using high resolution optical image and the GPS reading field verification data.

3.2 Materials

The dataset used in the present research incorporated space-borne images of Sentinel-1 and Landsat8 optical imagery. Three Sentinel-1 SAR images were utilized for flood mapping (Table 3.2). Sentinel-1 mission provides advantage of accessing frequently and timely radar data. The level-1 ground range detection (GRD) Sentinel-1 C-band data were collected in the Interferometric Wide Swath (IWS) mode. The data sets were ‘reference’ and ‘crisis’ images downloaded from the Copernicus sentinels scientific data hub of the European Space Agency (ESA).

3.2.1 Sentinel-1A Synthetic Aperture Radar (SAR) Imagery

The Sentinel-1A SAR imagery which is the first of the five missions that ESA is developing for the Copernicus initiative was launched on 3 April, 2014 on a Soyuz rocket from Europe's Spaceport in French Guiana for land and sea monitoring, natural disaster mapping, sea ice observations and ship detection (Sentinel-1 User Handbook, 2013). It is an outstanding example of Europe's technological excellence in natural disaster monitoring that has a dual polarization capability, very short revisit times and rapid product delivery. The Sentinel-1 is a radar imaging satellite which delivers images both at day and night under all weather conditions. Sentinel-1 continues the C-band SAR earth observation of ESA's ERS-1, ERS-2 and ENVISAT, and Canada's RADARSAT-1 and RADARSAT-2 missions (CCRS, 2013).

The Sentinel- 1A SAR satellite operates at the C-band wavelength and transmits and measures energy at the HH and VV polarization (Sentinel-1 User Handbook, 2013). The C-band has an internal calibration scheme, where transmit signals are routed into the receiver to allow monitoring of amplitude/phase to facilitate high radiometric stability (Suresh and Gehrke, 2016). It is in a sun synchronous orbit and all weather capable remote sensing system. Series of temporal images downloaded for this study were from the European Space Agency (ESA) through the Sentinels scientific data access available on the Copernicus scientific data hub.

The radar data used in the present study were the intereferometric wide swath (IW) ground range detection (GRD) products that contain amplitude and intensity images in the polarization of vertical transmission and vertical reception –VV (Table 3.4). The available datasets were processed up to level 1 processing stage and projected to ground range using an earth ellipsoid model, elevation antenna pattern and range spreading loss corrections and thermal noise removal at this level (Suresh and Gehrke, 2016).

Table 3.4 Sentinel-1 SAR product specification (ESA Sentinel-1 User Handbook, 2013).

Mode	Incidence Angle	Resolution	Swath Width	Polarization
Stripmap	20 - 45	5 x 5 m	80 km	HH+HV, VH+VV, HH, VV
IWS	29 - 46	5 x 20 m	250 km	HH+HV,VH+VV, HH, VV
Extra Wide Swath	19 - 47	20 x 40 m	400 km	HH+HV,VH+VV, HH, VV
Wave Mode	22 - 38	5 x 5 m	20 x 20 km	HH, VV

The time series images used in the present study were the reference (before flood) image acquired on 22 March, 2016 and the two crisis (during flood) images acquired 15 April, 2016 and 09 May, 2016 (Table 3.5).

Table 3.5 The description of Sentinel-1A data used in the present study.

Product properties	Reference Image	Crisis Image1	Crisis Image 2
Product Type	GRD	GRD	GRD
Sensing Start Time	22 March-2016 03:09:12.316597	15 April-2016 03:09:13.212918	09 May-2016 03:09:14.342327
Sensing Stop Time	22 March - 2016 03:09:37.315319	15 April-2016 03:09:38.211774	09 May-2016 03:09:39.341202
Mission	Sentinel-1A	Sentinel-1A	Sentinel-1A
Acquisition Mode	IW	IW	IW
Pass	Descending	Descending	Descending
Track	79	79	79
Orbit	10476	10826	11176

The IW data mode has a scene size of 250 km in range and 170 km in azimuth respectively. It is with incidence angle varying from 29° to 46° and pixel spacing of 10m in both range and azimuth (Sentinel-1 User Handbook, 2013).This mode images in three sub-swaths using the terrain observation with progressive scans SAR or TOPSAR. Using this data set is not only by its capability of acquiring images both at day/night and all-weather conditions but also its ability to sharply distinguish water from other classes, given by the high contrast that exists in between (Psomiadis, 2016). This is due to that the Sentinel-1 SAR data properties such as its different mode of scanning and viewing angles of the sensor.

The t_1 and t_2 images were used for the thresholding and change detection application and the classification of the study area as the normal open water, the flooded and non-flooded areas. The datasets are in IW mode with VV polarization and C-band (5.6 cm wavelength) which is the common mode over the land surface.

3.2.2 Optical Satellite Image

Optical remote sensor images, particularly the multispectral optical images, are important for land- use/land-cover mapping (Nizalapur, 2008). The Landsat 8 operational land imagery (OLI) multispectral image was used for the year 2016 land-use/land-cover (LULC) classification of the study area. The Panchromatic (band-8) portion of the OLI was extracted to use as resolution merge of OLI into 15 meter pixel spacing for ease of land cover visualization and classification process.

Table 3.6 Optical sensor data used for land-use/cover classification.

Product ID	LC81680542016088LGN00
Coordinates	8.67683.39, 39.2556
Acquisition date	28 MAR-16
Path	168
Row	54
Grid Cell Size Panchromatic	15.00 meter
Grid Cell Size Reflective	30.00 meter
Projection	WGS84 UTM ZONE 37

3.2.3 Digital Elevation Model (DEM)

The use of digital elevation data in such a way that floods are more likely to happen along River networks and in regions having specific geomorphological features is indispensable in flood detection analysis. Flat and concave regions have higher probability of being flooded. Thus, DEM is essential to support identifying the flood susceptible areas or flooding probability based on terrain, altitude and slope derived from it. Using DEM with satellite observations of inundation extent offers a promising approach in characterizing the spatial and temporal patterns of flood risk (Sanyal and Lu, 2005 as cited in Daniel, 2007). It is most obvious factor in controlling stream flow. The DEM used in the present study is from shuttle radar topography mission (SRTM) imagery with 30 meter spatial resolution.

The SRTM DEM can be obtained through SAR interferometry of C-band signals which is available in 30 and 90m spatial resolutions and an approximate vertical accuracy of 3.7m. The vertical accuracy of SRTM is higher in areas with gentle slopes than on steep slopes. On the low-lying floodplains, it has less than 2m accuracy (Musa et al., 2015).

3.2.4 Rainfall Data

The monthly rainfall data for the year 2014, 2015 and 2016 of study area were accessed from the Ethiopian National Meteorological Agency. This data was used to compute the monthly statistical record of the rainfall for the last three years. It is important to associate the flooding occurrence with the rainfall temporal behavior and its intensity.

3.2.5 Field Data

The filed survey was conducted from 17, April to 22, April, 2017. This time was selected because of that the flood was happed by this moth of 2016. As the study area has irrigation development potential, the field survey by this month helps observe the crop coverage of the time being.

The reference data were collected using the GPS reading for each feature class in the study area. For the land-use/land-cover classification, ten sample points of the representative land cover classes were selected. The area where the 15 April and 09 May, 2016 flood occurred, were also observed and the reference points on these area were collected and compared with the identified flooded areas of the SAR time series images.

3.2.6 Software Packages and Tools used in the Present Study

Software used in the present study were selected based on the capability to work on the existing problems in achieving the predefined objectives. The software and tool packages mainly used in the radar and optical data processing of the present study were: Arc GIS 10.2 packages. These packages were used to victories raster images and prepare the cartographic elements of maps in the documents. ERDAS IMAGINE 10.0 was used for image stacking and land-use/land-cover classifications of the study area. The other software used was SNAP version 4.0. This SAR processing tool was used to geocode, calibrate, co-register and process the statistical values of SAR images. PCI Geomatica version 16.00 was also provided the various SAR data filtering algorisms. It has robust capabilities for radar image processing. Microsoft packages were used for different statistical calculations, tables, graphs and the like.

3.3 Data Processing Methods

Detection of flood from SAR data involved intensive processing of SAR time series images to discriminate flood water from the normal water and other feature. Several sub processing were performed in each major SAR image processing steps. The following SAR image preprocessing and processing steps were performed to extract flood extent in the present study area. The processes focuses on the principle that calm open water and flood water (except its turbidity impact) act as a speculate reflector where the echo signal reflects away from the sensor and that appears dark in relation to other land surfaces due to the low backscatter signal to the radar sensor.

The general processes of the work in the present study included the SAR image calibration, speckle filtering, SAR time series image co-registration, multitemporal image stacking, statistical analysis of SAR image feature backscatters, backscatter extraction from region of interest (ROI), identification of changes in SAR multi look images, classification and producing of flood extent map. The overall procedures followed in the present study was demonstrated in Figure 3.11.

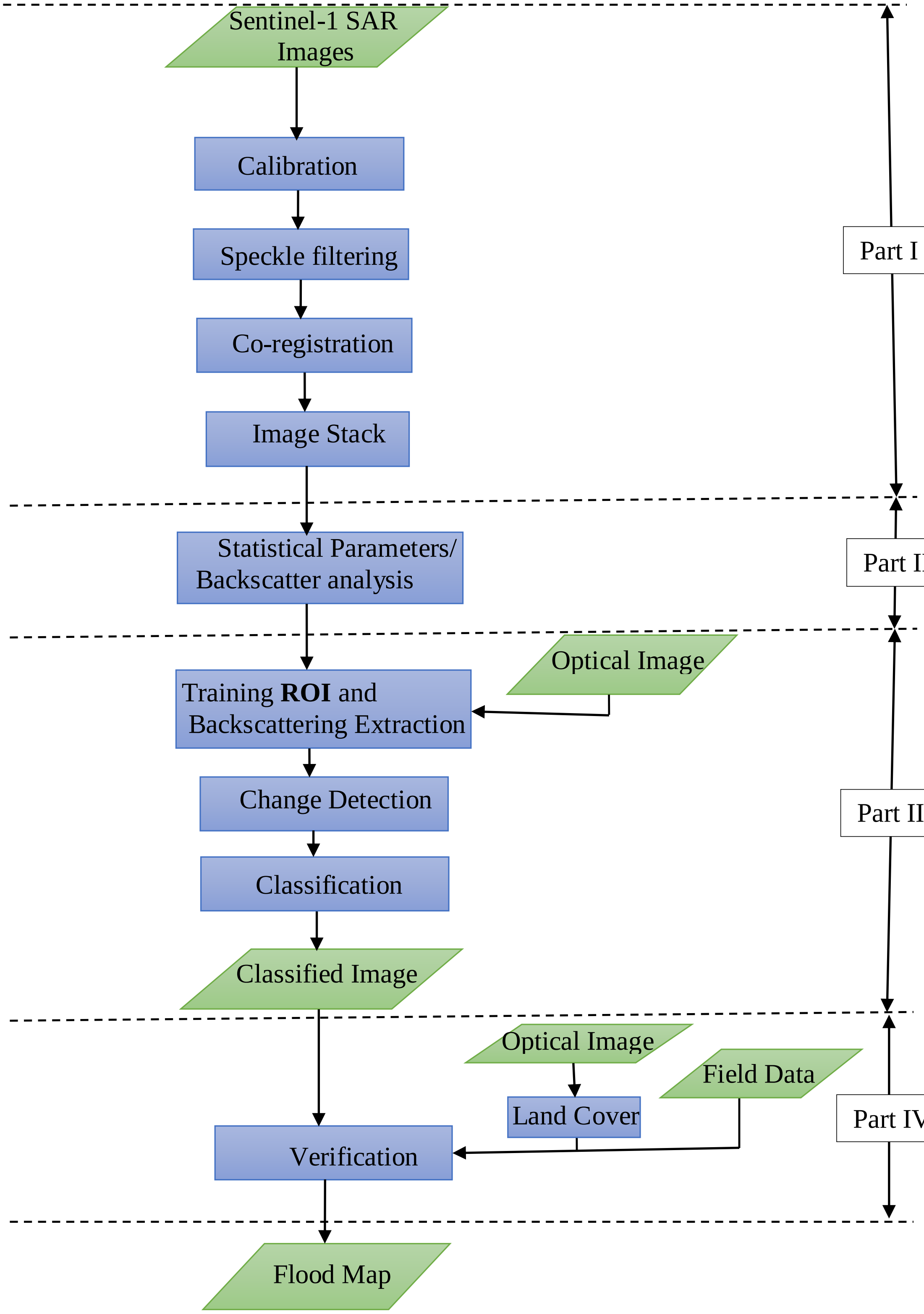

Figure 3.11: The general workflow of flood detection in the study area.

3.3.1 Synthetic Aperture Radar Image Calibration

It was performed as one of the SAR image preprocessing steps using sentinel application platform (SNAP). The objective of SAR calibration is to provide imagery in which the pixel values can be directly related to the radar backscatter (measured in dB) of the scene. Typical SAR data processing, which produces level 1 images, does not include radiometric corrections and significant radiometric bias remains. Therefore, it is necessary to apply the radiometric correction to SAR images by which the pixel values of the SAR images truly represent the radar backscatter of the reflecting surface. The data calibration compensates for the radiometric influences of different incidence angles- caused by the sensor geometry and topographic characteristics of the surface (Martinis and Rieke, 2015).

The radiometric correction is also necessary for the comparison of SAR images acquired with different sensors, or acquired from the same sensor but at different times, in different modes, or processed by different processors.

For converting digital pixel values to radiometrically calibrated backscatter, all the required information can be found in the product metadata. A calibration vector is included as an annotation in the product allowing simple conversion of image intensity values into sigma or gamma nought values.

The level- 1 products are provided with dedicated calibration annotation data set (CADS) in the product metadata, providing the necessary information to convert the radar reflectivity into physical units (in dB) or digital numbers (DN).The CADS provides four look up tables (LUTs):
$A\beta$: to transform the radar reflectivity into beta β^0 where the area normalization is aligned with the slant range.
$A\sigma$: to transform the radar reflectivity into radar cross-section σ^0 where the area normalization is aligned with ground range plane.
$A\gamma$: to transform the radar reflectivity into gamma γ^0 where the area normalization is aligned with a plane perpendicular to slant range.
A_{dn}: to revert for the final pixel scaling. The final products are coded in 16 bits integers (signed for single look complex product (SLC) and unsigned for GRD). The LUTs apply a range-dependent gain including the absolute calibration constant (in case of the present study, the original GRD SAR data has a calibration constant value of 1.000000e+00). The Earth model used in the CADS is the ellipsoid inflated with an average height such that the area normalization factor can be simplified to:

- $\sin(\alpha)$ in the σ^0 case
- $\tan(\alpha)$ in the γ^0 case, where α is local incidence angle of the earth model used.

In the present study the radar reflectivity beta β0 and radar cross-section sigma nought (σ0) were used as sentinel-1 data calibration product. It is possible to calibrate the sentinel-1 GRD product using SNAP toolbox automatically with the following equation:

$$\sigma^0 = \frac{DN^2}{A_\sigma^2} \tag{3.3}$$

$$\beta^0 = \frac{DN^2}{A_\beta^2} \tag{3.4}$$

where; DN: is the pixel digital Number of GRD pixel amplitude directly taken from the measurement file

A : is the value of sigma nought (σ^0) and beta nought (β^0) in the product metadata

The radar backscattering coefficient σ^0 is related to the radar brightness β^0 as follows:

$\sigma^0 = \beta^0 \times \sin\alpha$, where α is the local incidence angle. The backscattering coefficient is usually expressed in decibels:

$$\sigma^0\ (\mathrm{dB}) = 10.\log_{10}{}^{\sigma 0} \tag{3.5}$$

As shown in Figure 3.11 below calibrating the row radar image into surface reflectance results in variation of features response to the radar signal in the area of interest.

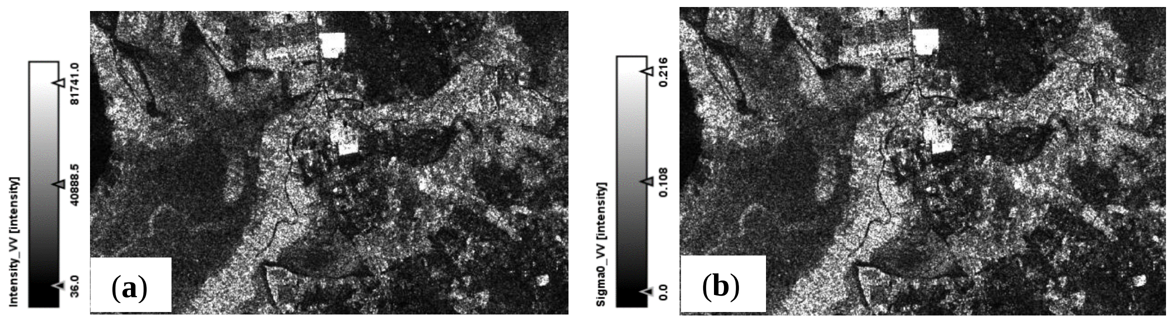

Figure 3.12: **a**) Original SAR intensity image and **b**) the radar backscattering coefficient sigma (σ^0) image near Lake Koka.

3.3.2 Synthetic Aperture Radar Speckle Filtering

Speckle is a signal-dependent noise which is natural to any images obtained by coherent radiation, including SAR. Unlike optical remote sensing images which are characterized by very neat and uniform features, SAR images are affected by speckle (Babu et al., 2013). It is a granular disturbance, usually modeled as a multiplicative noise that affects SAR images and all coherent images (Argenti et al., 2013). It reduces the readability and decreases the usefulness of the images for both human and automatic interpretation (Dekker, 1997). Many researches have been done concerning speckle and its characteristics (Huang and Genderen, 1996; Dekker, 1998; Raju et al., 2013; Hatwar and Kher, 2015) on satellite imageries particularly in SAR technology images.

Therefore, there are techniques that were applied in SAR image used to remove speckle noise which are termed as speckle filtering. Speckle filtering is a preprocessing step that is applied on each temporal or time series SAR images.

The speckle filtering suppresses the noise that eases the better backscatter analysis and thus, it turns out to be a critical pre-processing step for detection or classification optimization. To eliminate the effect of speckle noise in the context of change detection using multitemporal SAR images, two scenarios were tested (as in Yousif, 2015).

The first scenario was that the SAR image despeckling takes place after merging of SAR time serious images. This is called multi-temporal speckle filtering. For a sequence of N registered multitemporal images, with intensity at position (x, y) in the k^{th} image denoted by $I_k(x, y)$, the temporal filtered images are given by:

$$J_k(X,Y) = \frac{\mathrm{E}\,[I_K]}{N}\sum_{i=1}^{N}\frac{I_i(X,Y)}{E[I_i]} \tag{3.6}$$

where; $k = 1, 2 ..., N$,
$E\,[I_i]$ is the local mean value of pixels in a window centered at (x, y) in image I.

The multitemporal filtering algorithm has basically two preprocessing steps. The first step is calibration in which σ^0 is derived from the digital number at each pixel. This ensures that values from different times and in different parts of the image are comparable. And the second step is registration of the multitemporal images. Then after the merged images of t_1, t_2…n, the stacked image was filtered once.

The second scenario, as depicted in Figure 3.13, is filtering of individual single time SAR images and then merging together for the application of change detection. This method was selected to filter the SAR images for the present study purpose.

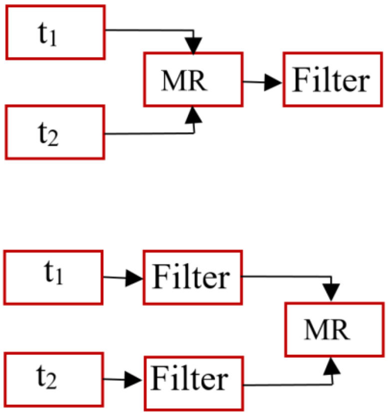

Figure 3.13: The scenarios of SAR time series image despeckling.

The speckle filtering consists of moving kernel over each pixel in the image and applying a mathematical calculation using the pixel values under the kernel and replacing the central pixel with the calculated value (Mansourpour et al., 2011). The kernel is moved along the image's one pixel at a time until the entire image has been covered. By applying the filter a smoothing effect is achieved and the visual appearance of the speckle is reduced. Several standard filtering algorithms are available in PCI geomatica SAR analysis algorism library. The following are some of the adaptive SAR image filtering techniques used by the researchers in the field of SAR image processing dedicated to flood detection and mapping.

Median filter

The median filter is a simple filtering method and simply removes pulse or spike noises. Pulse functions of less than one-half of the moving kernel width are suppressed or eliminated but step functions or ramp functions are retained (Mansourpour et al., 2011). For certain types of random noise and particularly the pulse noise, they provide excellent noise-reduction capabilities, with considerably less blurring than linear smoothing filter (Dong and Ping, 2015). The median is an edge preserving filter and is less influenced by extreme values (peaks). This filter allows reducing abnormal peaks and holes and homogenises surfaces. Furthermore, edges between water and land as well as linear elements such as streams and dykes are well preserved. Water surfaces as well as some land features appear more homogeneous (Dong and Ping, 2015).

Lee-sigma filter

This filter utilizes the statistical distribution of the DN values within the moving kernel to estimate the value of the pixel in the region of interest (ROI). The gaussian distribution is assumed for noise suppression in the image data. The Lee filter is based on the assumption that the mean and variance of the pixel of interest is equal to the local mean and variance of all pixels within the user-selected moving kernel, i.e. 3×3, 5×5 and 7×7 (Lee, 1981 as cited in Mansourpour et al., 2011). The formula used for the Lee filter is:

$$DN_{out} = [Mean] + K\,[DN_{in} - Mean] \qquad (3.7)$$

where; Mean = average of pixels in a moving window

$$K = \frac{V(x)}{[Mean]^2\sigma^2 + V(x)} \quad \text{and}$$

$$V(x) = \left[\frac{(Variance\ with\ in\ window) + (\text{Mean with in window})}{[Sigma]^2 + 1}\right] - [\text{Mean with in window}]$$

The Lee-sigma filter is based on the probability of a gaussian distribution. It is assumed that 95.5% of random samples are within a 2 standard deviation range. This noise suppression filter replaces the pixel of interest with the average of all DN values within the moving kernel that fall within the designated range (Mansourpour et al., 2011).

Gamma-MAP filter

The Maximum A Posteriori (MAP) filter is based on a multiplicative noise model with non-stationary mean and variance parameters. In this filtering case, the process assumes that the DN value of the original image lies between the DN of the pixel of the interest and the average DN of the moving kernel. This filter is designed to smooth out noise of the SAR image while keeping edges or shape features in the image (e.g. Argenti et al., 2013). It is highly dependent on the filter window kernel sizes. The smaller filter size results in ineffective noise filtering algorism and if the filter size is too large detail information of the image will be lost. Thus, for the gamma-map filtering method it is important to decide an optimum filtering window kernel size. Most studies (e.g. Argenti et al., 2013; Babu et al., 2013) used a 7×7 kernel size filter that usually gives the best tradeoff. The gamma-map algorithm has the following formula (Mansourpour et al., 2011).

$$\widehat{I}^3 = \bar{I} + \sigma(\bar{I} - DN) = 0 \qquad (3.8)$$

Where; $\widehat{I}$ = sought value

$\bar{I}$ = local mean

DN = input value

σ = the original image variance

A Posteriori (MAP) filter is based on a bayesian analysis of the image statistics. It assumes that both the radar reactivity and the speckle noise follow a gamma distribution.

Frost filter

This type of SAR image filtering replaces the pixel of the ROI with a weighted sum of the values in the n×n moving window kernel. The weighting factors decrease as the distance decreases from the pixel of the interest. However, the weighting factor for the central pixel increases with the increase of the variance in a kernel. This filter assumes multiplicative noise and stationary noise statistics and follows the following formula (Mansourpour et al., 2011).

$$\mathrm{DN} = \sum_{n \times n}^{n} \mathrm{k}\alpha e^{-\alpha|\mathrm{t}|} \tag{3.9}$$

Where; $\alpha = (4 / n\sigma^2)\ (\overline{\sigma}^2/\bar{I}^2)$

k = normalization constant

$\bar{I}$ = local mean

σ=local variance

$\overline{\sigma}$= image coefficient of variation value

$|t| = |X-X_0| + |Y-Y_0|$, and

n = moving kernel size

Boxcar filter

The boxcar (mean) filter is a simple despeckling method which does not remove the speckles of the SAR image. It simply averages the noise into the data. Thus, boxcar filter is the least satisfactory method of speckle noise reduction as it results in loss of detail information and resolution. However, it can be used for applications where resolution is not the first concern.

Standard deviation filter

The standard deviation speckle filter is primarily used on SAR data to remove high-frequency noise (speckle), while preserving high-frequency features (edges).

Kuan filter

Kuan filter is used to filter speckled SAR data. This filter smoothed the image data without removing edges or sharp features in the images. It is only applicable for radar-intensity images. The Kuan filter first transforms the multiplicative noise model into a signal-dependent additive noise model. Then the minimum mean square error criteria is applied to the model. The resulting filter has the same form as the Lee filter but with a different weighting function.

Generally, different filter sizes can greatly affect the quality of processed images. If the filter is too small, the noise filtering algorithm is not effective. If the filter is too large, subtle details of the image will be lost in the filtering process. The 7x7 krnel filter usually gives the best results (Mansourpour et al., 2011). In the present study different noise reduction algorithms were applied with similar window kerenel size i.e.7×7. Each filter size was tested by visually and statistical comparison of the results. After comparing the filter results, the gamma map filtering method was applied to the present study as a speckle filtering technique. The selection of this filter over the other was because of that the gamma map filter is suitable for a wide range of gamma distributed scenes, such as vegetation and agriculture areas; water and dry lands which are the dominant features in the study area. The filter preserves the observed pixel value for non-gamma distributed scenes. The filtering process was performed by PCI geomatica version16.00.

3.3.3 Synthetic Aperture Radar Image Co-registration

The essential step for image staking to remove geometric difference between time series images is co-registration. When multiple images cover the same region and a speckle filtering on time-series images are required, SAR images must be co-registered (sarmap, 2009). The SAR input images for stacking must belong to the same coordinate system and as it is important to obtain a high quality radar data, individual images need to be co-registered. The SAR interferometry requires pixel-to-pixel match between common features in SAR image pairs and thus it is an essential step for the accurate determination of phase difference and for noise reduction (Li and Bethel, 2008). The sub-pixel co-registration of SAR images is a strict requirement and critical component of any interferometric processing chain. When multiple images for the analysis of various applications cover the same region which requires intensive speckle filtering, SAR images co-registration is a pre-request. It is essential for applications such as speckle filtering, change detection and interferometric deformation analysis (Li and Bethel, 2008). It is also important for spatial registration and potentially resampling (in cases where pixel sizes differ) to correct for relative translational shift, rotational and scale differences of SAR images (sarmap, 2009).

Synthetic Aperture Radar co-registration process has the coarse co-registration and fine co-registration systems. In the SAR coarse co-registration, the registration is up to the pixel level accuracy including searching for coarse image offsets and shifting the slave images. The coarse registration is achieved using a cross correlation operation between the images. It is where the integer shifts between the two images in range and azimuth are computed. This could be done by cross-correlating the amplitudes of the images or maximizing a spectral signal to noise ratio. Fine co-registration is a process to find the sub pixel tie points on two SAR images (Li and Bethel, 2008).

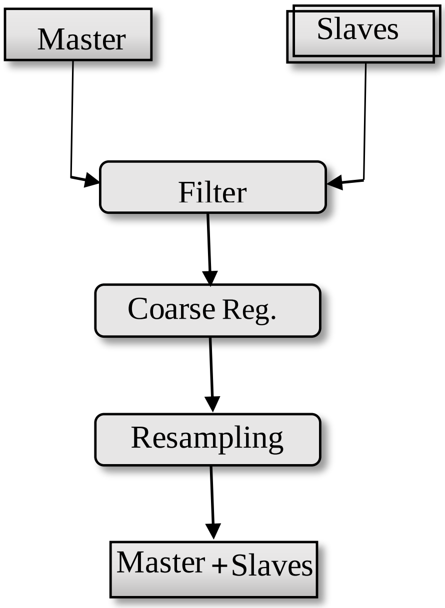

Figure 3.14: Flowchart for SAR image co-registration.

Input SAR images have to be from acquisitions taken at different times using compatible interferometric sensors, and must belong to the same type (i.e., they must be detected or complex). The data used in the present study were from the same sensor but from at different time of acquisition. In the process of co-registration, one original SAR image- slave was re-projected with respect to the other SAR image- master (Fig. 3.14). The registration is fully automatic with cross correlation operator in the sentinel application platform (SNAP) SAR co-registration available tools. It aligns one or more slave images with a master image in such a way that each pixel from the co-registered slave image represents the same point on the earth surface as its corresponding pixel in the master image.

3.3.4 Image Stacking

For the analysis and production of statistical parameters or backscatter properties, image stacking is compulsory. It involves the combination of more than one co-registered images. The SAR image stack is a component of co-registration. The create stack operator (CSO) allows collocating two spatially overlapping products where collocating two products implies that the pixel values of one product (the slave) are resampled into the geographical raster of the other (the master).

3.3.5 Backscatter Analysis of SAR Images

Synthetic aperture radar image is usually presented as a grey scale, with the intensity of each pixel representing the amount of energy returned from that area on the ground (Al-Ali, 2011). It is very important technique in active remote sensing for flood detection study analysis. An analysis of multi-temporal synthetic aperture radar data was performed to investigate the backscatter behavior of various classes of the study area in the context of flood mapping using single polarized SAR data. This analysis focused on the comparison of feature backscatter characteristics at different time and conditions (i.e., before flood and after flood). The SAR data set was converted to sigma nought (σ^0) to ensure that the different feature classes are statistically comparable. Backscatter is usually expressed in decibel (backscattering coefficient) which is given by:

$\sigma°$ (dB) = $10*\log10\sigma°$(energy ratio), whereby;

$$\text{Energy Ratio} = \frac{\text{Received energy by the sensor}}{\text{Energy reflected in an isotropic way}} \qquad (3.10)$$

The backscattered coefficient can be a positive number if there is a focusing of backscattered energy towards the radar or the backscattered coefficient can be a negative number if there is a focusing of backscattered energy away from the radar (Moreira, 2013). Positive values are almost for dense built up urban areas where double bouncing reflectance is common on such areas.

Backscatter coefficient ($\sigma°$) in decibels (dB) represents target backscattering area (radar cross-section) per unit ground area. Because it can vary by several orders of magnitude, it is converted to dB as $10*\log10\sigma°$. It measures whether the radiated terrain scatters the incident microwave radiation preferentially away from the SAR sensor (dB < 0) or towards the SAR sensor (dB > 0). This scattering behavior depends on the physical characteristics of the terrain, primarily the geometry of the terrain elements and their electromagnetic characteristics (Bartsch et al., 2012).

The backscatter analysis in SAR images provides ease in identification of changes happened over a period of time. For different applications, change detection in remote sensing images becomes more and more important (Dong et al., 1997). Two pre-processed images are taken as input and compared pixel by pixel and thereafter another image is generated, called the difference image (Pooja et al., 2014). This is done by the thresholding where its values are determined by spectral signatures or backscatter values from the before and after flood images to detect the changes.

For the radar backscatter analysis of the study area, six land cover classes were defined, based on high resolution optical images and knowledge of the region from the field survey. The land-cover classes were:1) open water; permanent free surface region, 2) agriculture land; both the dry farm land and irrigated land, 3) bare soil; areas of bare soil during the acquisition time, 4) vegetation cover; the upland and Riverine vegetation, and 5) areas on before flood and after flood event. For each class, radiometric samples were defined manually, based on visual interpretation of SAR, Landsat8 and high-resolution images available on Google Earth. After identification of the desired features for statistical backscatter analysis, the change detection and change classification process took place.

3.3.6 Change Detection

Image change detection is a process that analyzes images of the same scene taken at different times in order to identify changes that may have occurred at a considered acquisition dates (Gong et al., 2012). Different techniques have been used successfully in many applications, such as environmental monitoring, on land-use/land-cover dynamics, analysis of forest or vegetation changes, damage assessment, agricultural surveys and analysis of urban changes. It is widely applied in SAR domain to analyze the backscatter of different date images in the study of flood area identification (Abubakr, 2013). The backscatter of the SAR image is associated with the roughness of the terrain and water body (Devi1and Jiji, 2015). The radar antenna receives no backscatter from the calm water and it appears in dark tone in the SAR image. However, rough water surface appears in brighter tone. During floods the windy condition and the turbidity which are common in flood water, cause relatively higher backscatter than normal water.

Intensity and amplitude techniques are the commonly used change detection methods (Al-doski, 2013). In the intensity approach areas are generally identified as flooded where the intensity radar backscatter from before and after flood imagery is very different in backscatter values. Before flood images are always taken as reference image in the change detection of time series images of the same scene.

3.3.6.1 Change Detection Techniques

Different methods were proposed to flood mapping using satellite imagery. European space agency (ESA) uses a multi-temporal technique to the flood extent extraction from SAR images. This technique used SAR images of the same area taken on different dates (one image during flooding and the second on normal conditions).

The resulting multi-temporal image clearly reveals change in the earth’s surface by the presence of color in the image (Sergii, 2010). To extract the changes from multitemporal images, researchers have been using various techniques. The following are some of the methods used.

3.3.6.1.1 Image Texture Analysis

Due to the surface properties such as roughness, humidity and orientation every object in the SAR scene can have its own unique backscattering properties. Texture analysis is one of an effective way of flood detection from SAR imageries. It is a robust method to distinguish the classes in the SAR image which records the backscatter that carry information of kind, direction, heterogeneity and relationships of the features (Pradhan et al., 2013). Prasad et al. (2009) also described texture analysis as an important image analysis for supervised classification system that fuses texture information from the HH, HV, and VV polarizations of SAR images. As Kiema (2002) noted that topographic features such as water, crops, roads, settlements, etc. can be automatically extracted from satellite images using texture analysis.

3.3.6.1.2 Image Algebra Change Detection

The change algebra or image differencing method of change detection is the subtraction of two spatially co-registered imageries (Al-doski et al., 2013). Image differencing is performed by subtracting the DN value of one date for a given band from the DN value of the same pixel for the same band of another date which results in a new image (Devi and Jiji, 2015). Mathematically, image differencing is given by:

$$I_d\,(x,y) = I_1(x,y) - I_2(x,y) \tag{3.11}$$

Where I_1 and I_2 are images from time t_1 and t_2 and (x,y) are coordinates and I_d is the difference image. It is pixel by pixel process to identify where the change has or has not occurred. The pixels of changed areas are expected to be distributed in the two tails of the histogram of the resultant image, and the unchanged areas are grouped around zero (Al-doski et al., 2013). This simple method eases the interpretation of the resultant (the difference) image. The very important aspect in image differencing is in defining the threshold to detect the change from non-change classes. The image algebra involves one of two methods. The first one is band subtraction and the second method is band ratio (Devi and Jiji, 2015).

Image subtraction method

It results positive and negative values where changes have occurred and zero values where changes have no occurred. The pixels of changed area are expected to be distributed in the two tails of the histogram of the resultant image, and the unchanged area is grouped around zero. This simple method easily interprets the resultant image. However, it is crucial to properly define the thresholds to detect the change from non-change areas (Al-doski et al., 2013).

Band rationing method

This method can be computed in similar way as image subtraction. The only exception is that the division function is employed in the image rationing method. And the resulting ‘no change’ brightness values are represented by a value of 1. Change results are expressed as a ratio between two co-registered images. It can be expressed as:

$$I_r=I_1(x,y)/I_2(x,y) \qquad (3.12)$$

The advantage of this method is that it handles calibration (including sun angle, shadow and topography impact) errors efficiently (Devi and Jiji, 2015). An important element in the band rationg as that of both band subtraction is properly placing the threshold value in the decision of ‘changed’ and ‘not changed’ pixels of the input SAR images. Thresholding involves the selection of an optimum value that can be applied to an image in order to separate an object from a background. It is an active research area in the digital image processing field, and several techniques, with varying degrees of success, have been developed (Yousif, 2015). Thresholding algorithms differ in terms of the assumptions upon which they have been developed. Automatic thresholding techniques have the advantage that no training or prior knowledge about the properties of the object and background are required. The automatic algorithm often uses image content (e.g., its histogram) to estimate an optimum threshold (Yousif, 2015). For the binary distinction of change or no-change, threshold value should be determined. However, selecting of a thresholds is generally depend up to analyst’s ability or skill in identifying changed area. The threshold value is usually chosen as multiplies of the standard deviation of digital numbers of the difference image.

3.3.6.1.3 Principal Component Differencing (PCD)

Principal component differencing is often as accepted as an effective transforms to derive information and compress dimensions. Most of the information is focused on the first two components. Particularly, the first component has the most information. According to Al-doski et al. (2013), the difference of the first PCA component of two dates has the potential to improve the change detection results. It is expressed as:

$$PCD = PC1\,(t_1) – PC1\,(t_2) \qquad (3.13)$$

Two dates of image data were superimposed and treated as a single dataset. The PCA is implemented on the stacked datasets of SAR t_1 and t_2. The main component images often contain the overall radiation difference that reflects different land cover types. However, it is often not easy to determine the change areas in the absence of a careful and complete examination of the resultant image and field data or in combination with visual interpretation of the multi-date composite image (Al-doski et al., 2013). The present study used the image algebra and the PCD change detection methods since they are easy to compute and quantify the change devoted to flood extent mapping. In the image algebra change detection, both image subtraction and image rationg algorithms were used. The results from these methods, were presented individually and compared with one another.

CHAPTER FOUR

4. RESULTS AND DISCUSSIONS

4.1 Results

4.1.1 Synthetic Aperture Radar Speckle Filtering

The speckle filtering carried out in this study was based on two scenarios. The first one focused on the single date SAR image filter using various filtering types with the same window kernel size (7×7) which is the optimal SAR filtering kernel (Fig. 4.1). Each filtered image has shown different smoothed gray value levels with each respective filtering type. The noisy original SAR image was suppressed to smooth a grainy, salt and pepper appearance which are the dominating factors in radar imagery. Figure 4.1 showed the filtered SAR image by various speckle filtering types.

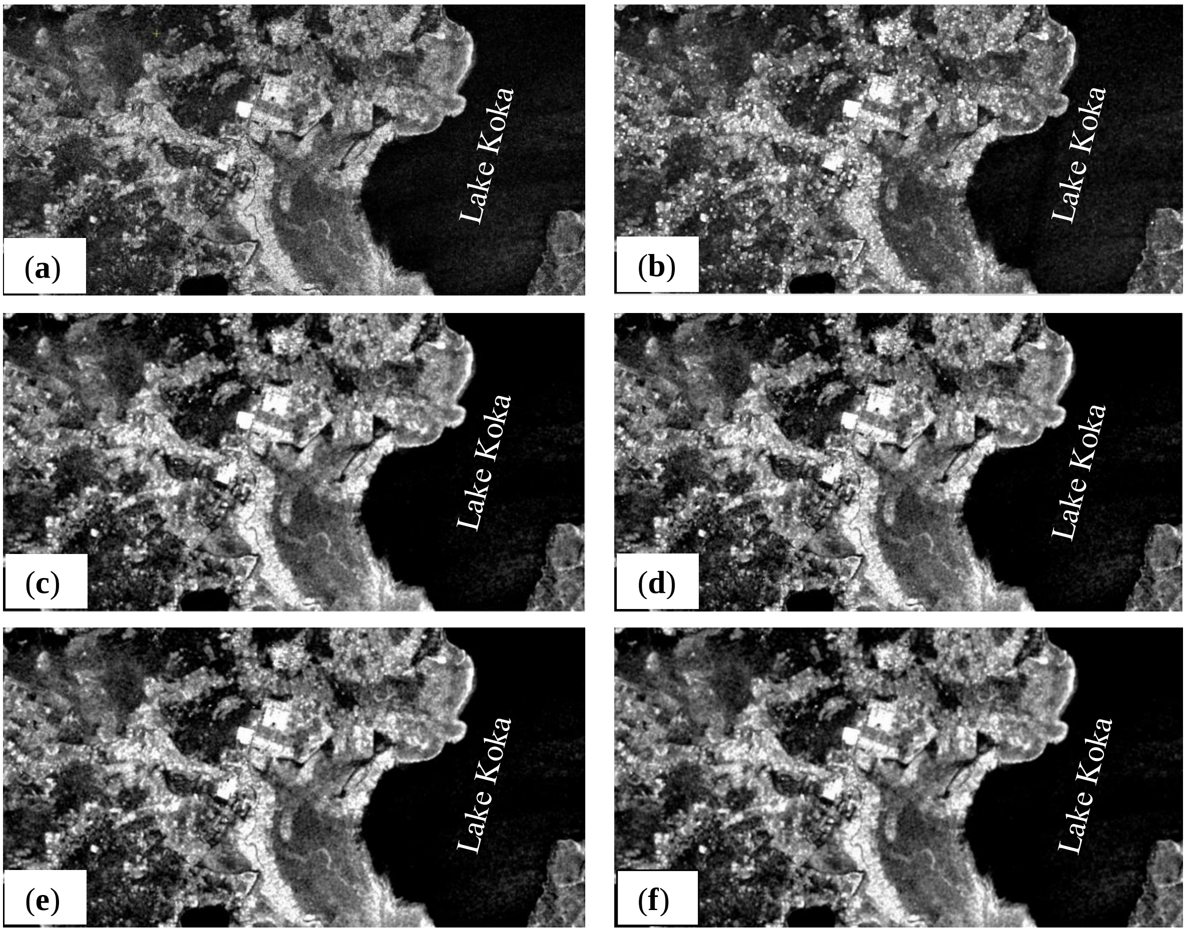

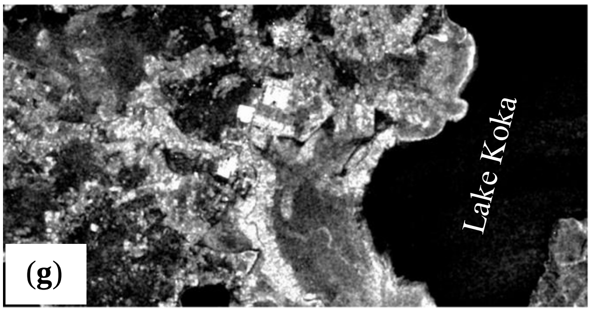

Figure 4.1: Original SAR image and filtered images with various filter types of a 7×7 kernel window size: **a**) represented the original SAR image, **b**) is the standard deviation filter, and **c**) showed the kuan filter, **d**) represented frost filter, **e**) showed the gamma map filter, **f)** represented median filter, **g**) showed lee filter of the SAR image of Lake Koka area.

The despeckling of SAR image involved in the smoothing of gray values contained in the original image. Figure 4.2 below showed the suppressed noisy SAR image in to better interpretable image. In the Figure 4.2a which is the original non-filtered image, the gray values are highly concentrated each other. This thick concentration of gray values hide the required information from the image for visual interpretation and classification purpose. Figure 4.2b represented the gamma map 7×7 window kernel size filtered image profile. It depicted that the grainy, salt and pepper appearance on the original SAR image were smoothed. The filtered image profile graph showed the smoothed gray values. The gray values in the filtered image are less concentrated each other unlike that of the non-filtered image (Fig2a).

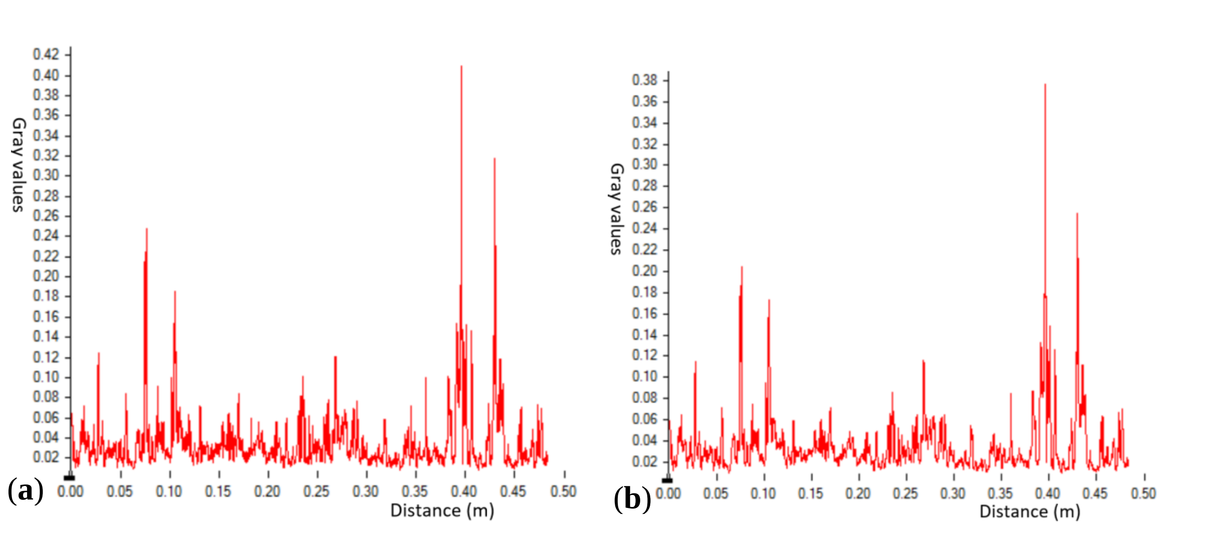

Figure 4.2: **a**) The gray value profile of original non-filtered SAR image and **b**) gamma map 7×7 filtered image

The second filtering scenario applied in the present study was based on stacked time series SAR images. In this case the original row time (t_1 and t_2) images were co-registered and stacked together on which the multi-temporal despeckling algorithm was applied (Fig. 4.3).

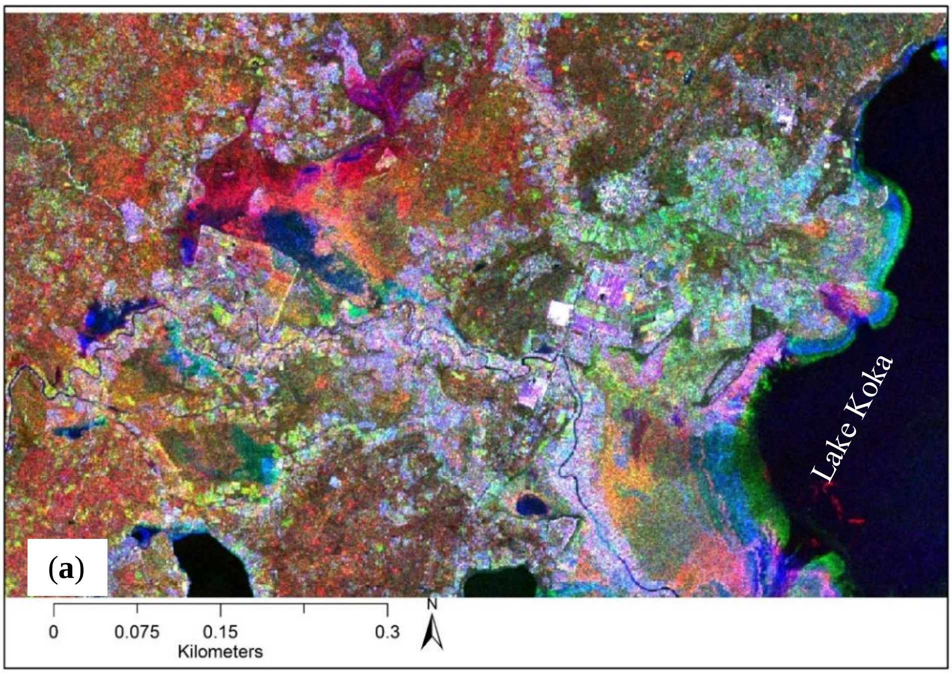

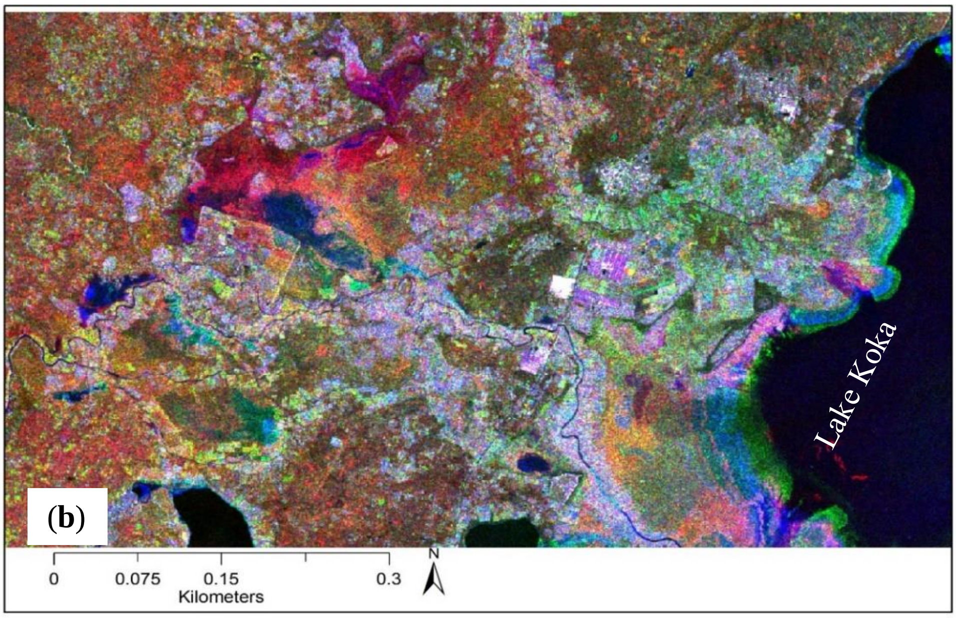

Figure 4.3: **a**) RGB (Red: May 2016, Green: April 2016 and Blue: March 2016) composite of original stacked image and **b**) multi-temporal gamma map7×7 filtered image.

The important aspect in image filtering is selection of the appropriate filter type depending on the type of SAR image application. The gamma map filter was chosen as a SAR image filtering method for the present study. This selection was based on the quality of the filter which was measured by the equivalent number of looks- ENL (as in Santoso et al., 2016). The ENL as a parameter represents the equivalent to the number of independent intensity values averaged per pixel. The signal to speckle ratio provided how the filtered image quality is better.

The higher the ENL value from the signal to speckle ratio image for a filter is the higher image quality. This implies that the higher in ENL is better filtering algorism. The ENL characterizes the smoothing effects of post-processing operations of image filtering. According to the statistical results of each filter type presented below in Figure 4.4, the ENL value for gamma map filter is higher than the other filtering types. This statistical comparison between the different filter types provided that the optimal filtering type for the SAR image in the present study was gamma map 7×7 filtering method. The histogram of the gamma map filter (Fig. 4.4b) depicted the distributed pixel values, not concentrated in the either tail of the histogram. The gray tonal values of each pixel is well distributed throughout the SAR image.

#Pixels total:	42010344
Minimum:	2.1897E-4
Maximum:	5.3752
Mean:	0.9706
Sigma:	0.3354
Median:	0.9301
Coef Variation:	0.7160
ENL:	1.9508
P75 threshold:	1.1666
P80 threshold:	1.2311
P85 threshold:	1.3063
P90 threshold:	1.4085
Max error:	0.0054

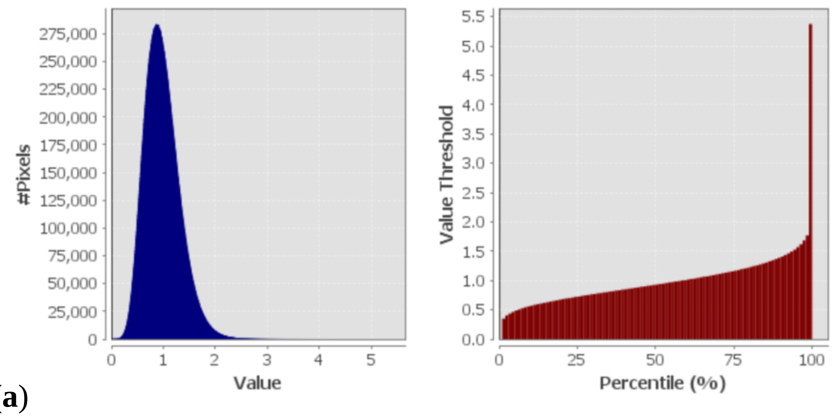

(a)

#Pixels total:	42010348
Minimum:	3.9727E-4
Maximum:	2.9984
Mean:	0.9701
Sigma:	0.3359
Median:	0.9268
Coef Variation:	0.7020
ENL:	2.0294
P75 threshold:	1.1726
P80 threshold:	1.2386
P85 threshold:	1.3195
P90 threshold:	1.4275
Max error:	0.0030

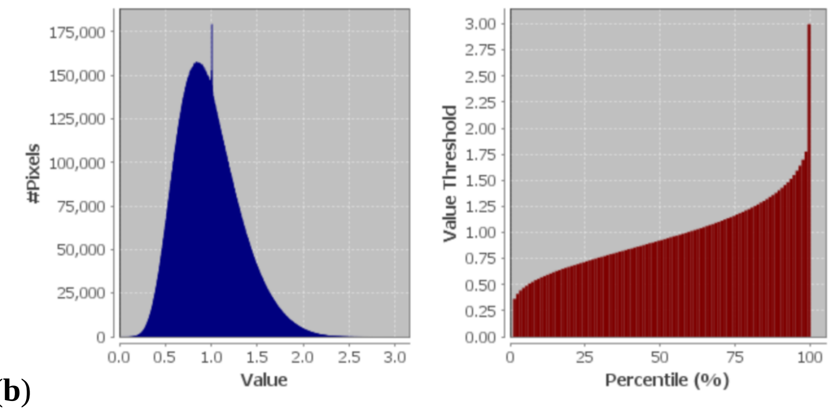

(b)

#Pixels total:	42010358
Minimum:	9.283E-5
Maximum:	10.3860
Mean:	0.9766
Sigma:	0.4122
Median:	0.9140
Coef Variation:	0.9533
ENL:	1.1004
P75 threshold:	1.1945
P80 threshold:	1.2776
P85 threshold:	1.3710
P90 threshold:	1.5060
Max error:	0.0104

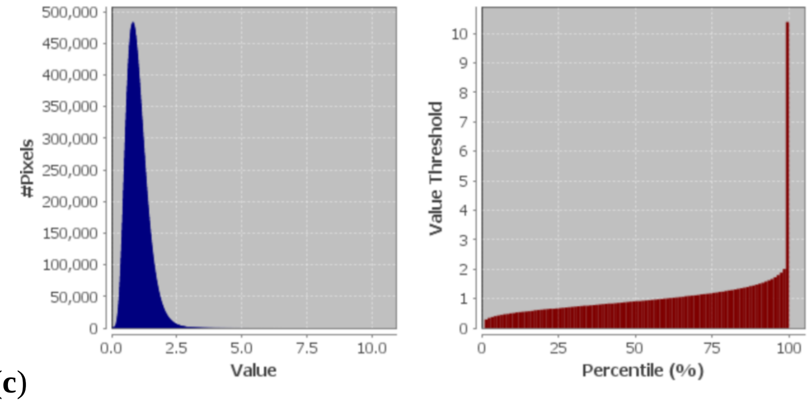

(c)

#Pixels total:	42010366
Minimum:	4.2965E-5
Maximum:	14.6916
Mean:	2.3162
Sigma:	1.1337
Median:	2.1597
Coef Variation:	0.9313
ENL:	1.1529
P75 threshold:	3.0412
P80 threshold:	3.2909
P85 threshold:	3.5554
P90 threshold:	3.9080
Max error:	0.0147

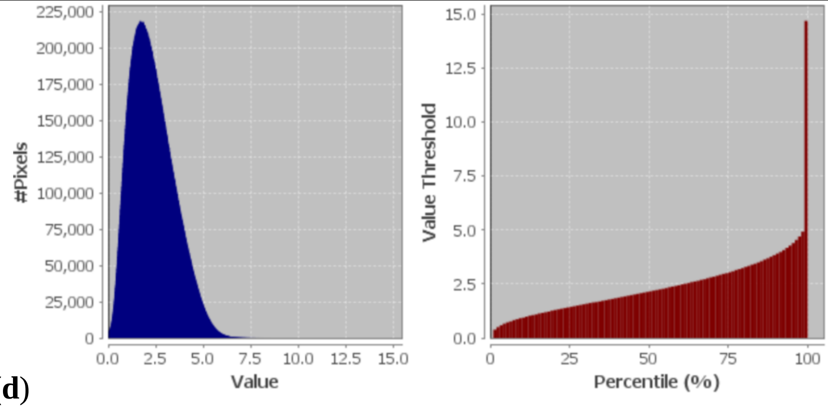

(d)

#Pixels total:	42010366
Minimum:	7.3125E-5
Maximum:	12.1433
Mean:	0.9764
Sigma:	0.4158
Median:	0.9108
Coef Variation:	0.9786
ENL:	1.0442
P75 threshold:	1.1901
P80 threshold:	1.2751
P85 threshold:	1.3723
P90 threshold:	1.5058
Max error:	0.0121

(e)

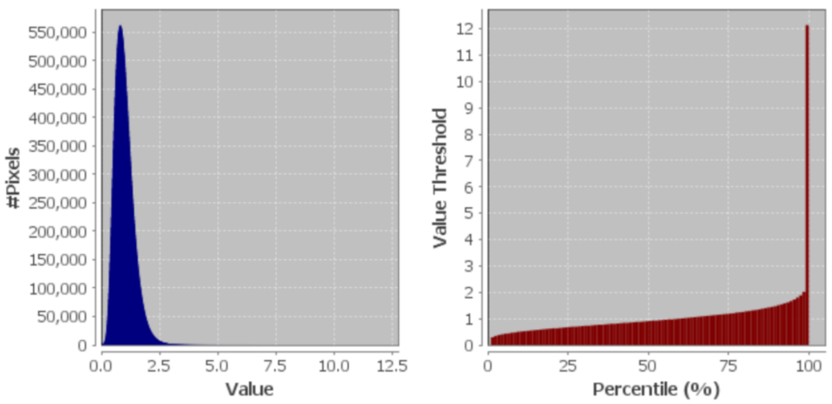

Figure 4.4: Filtering statistics of SAR image: **a**) Frost, **b**) Gamma map, **c**) Lee sigma, **d**) Standard deviation and (**e**) Median 7×7 kernel size filters.

The ENL value of the filters mentioned in Figure 4.4 above was 1.9508, 2.0294, 1.1004, 1.1529, and 1.0442 for frost, gamma map, Lee sigma, standard deviation and median filters respectively. The value of ENL for gamma map is higher than the other i.e. it resulted better image quality.

Table 4.1 Performance test of speckle filtering types for SAR image.

No.	SAR image Filter Type	Equivalent Number of Look
1	Frost	1.95
2	Gamma map	2.03
3	Lee sigma	1.10
4	Standard deviation	1.15
5	Median	1.04

In the present study, the first scenario of filtering was applied (i.e. filtering individual images and then co-register the images). This was because of that as the aim of the study was to extract flooded pixels from non-flooded, the information degraded by co-registration process after individual filter was insignificant (Fig. 4.5).

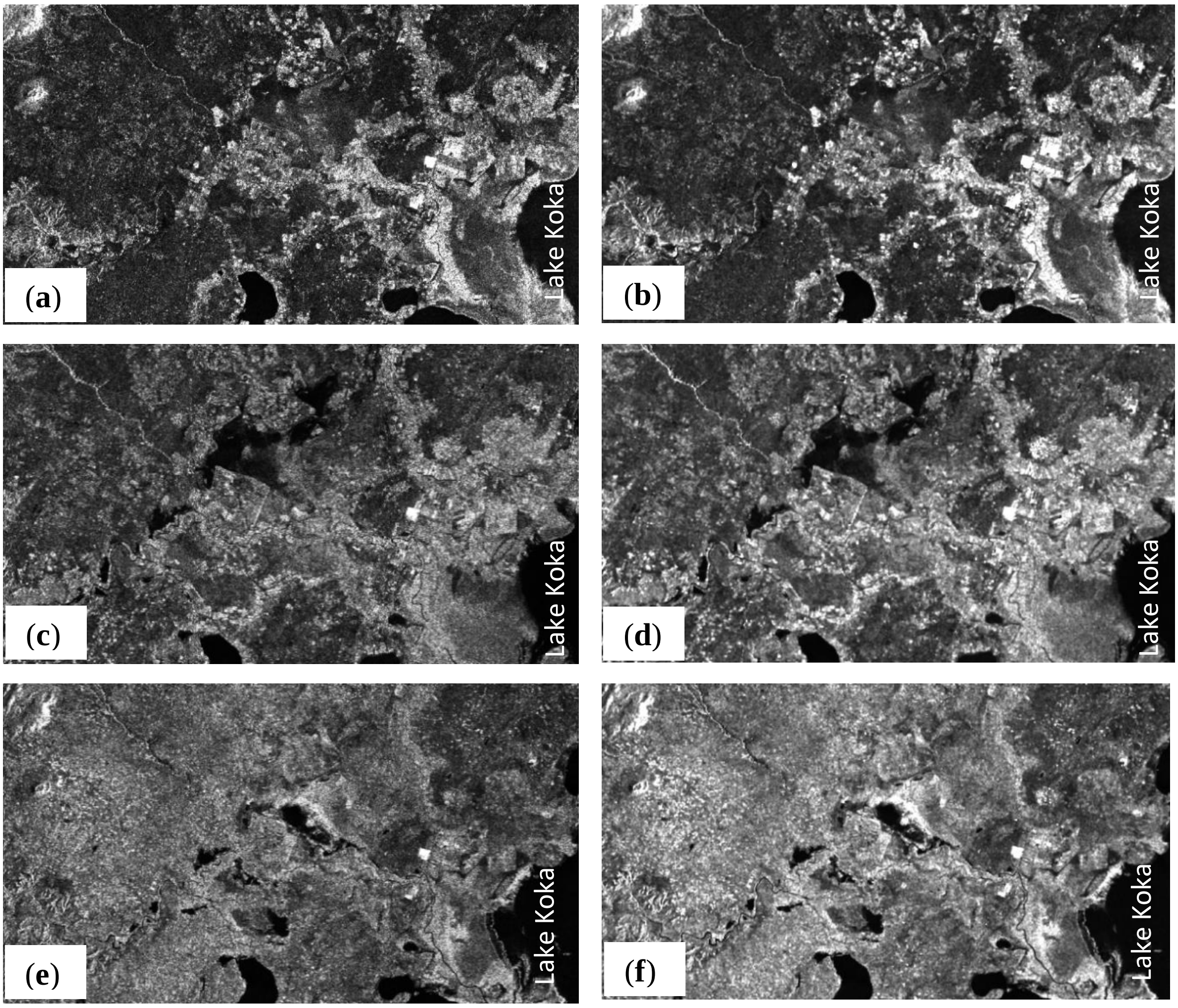

Figure 4.5: Time series original images and single product gamma map filtered SAR images: **a**) 22 March, 2016 reference, **c**) 15 April, 2016 crisis, **e**) 09 May, 2016 crisis SAR image and **b, d, f**) gamma map 7×7 kernel size filtered images.

Each individual SAR images were filtered first and stacked together for time series analysis. The filtered SAR images (Fig.4.5) showed smoothed pixels with deep black color represented permanent water body and flood water, light black color of soil and the brighter tone represented agriculture and vegetation areas. The gamma map filtered sharply discriminated flood and permanent water from the other feature classes. Figure 4.6 presented the filtered sigma0 nought (a) and backscatter coefficient (b) of the 22 March 2016 (reference), 15 April, 2016 and 09 May, 2016 crisis images. The time series filtered SAR images were stacked and the RGB composite channel was made. It was used for the visualization of the change happed over a time t_1 and t_2 between the reference and crisis SAR images.

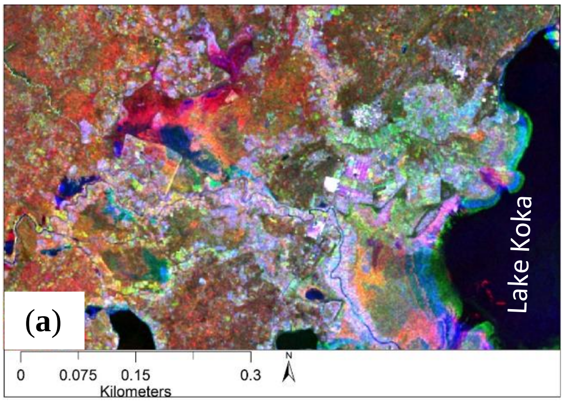

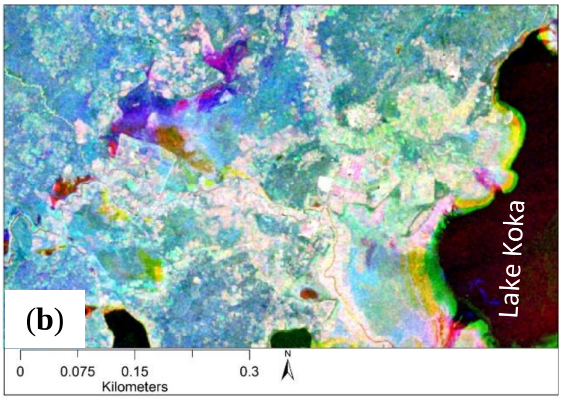

Figure 4.6: **a**) Time series RGB image of co-registered sigma0 and **b**) backscatter coefficient in dB of SAR images.

The RGB color composite (Fig.4.6) showed the difference between flood and dry conditions. Changed areas identified in purple color of the RGB composite image (Fig.4.6, b) is the flood of 15 April, 2016 and the pixels highlighted by yellowish orange color in figure 4.6b represented the flood of 09 May, 2016.

4.1.2 Land-use/land-cover Classification

The land-use/cover of the study area was derived from stacked images of optical and radar sensor data. The RGB composite of these two images was used for better visualization for the classification process. The SAR amplitude sigma nought (σ^0) and the Landsat8 displayed the composite image of the red, green and blue image planes (Fig. 4.7). The RGB composite helped the visualization of different features for the ease of land-use classification. This technique is particularly useful as an exploratory method for identifying features in fused different sensor images as a representative samples. This specific combination of the spectral bands from SAR and Landsat imageries were considered as quite suitable for the classification of land-use because of that the SAR images clearly show the water body, settlement and dense vegetation while the Landsat image can provide soil information with its band 7 that has spectral regions of absorption for water and reflectance for soil.

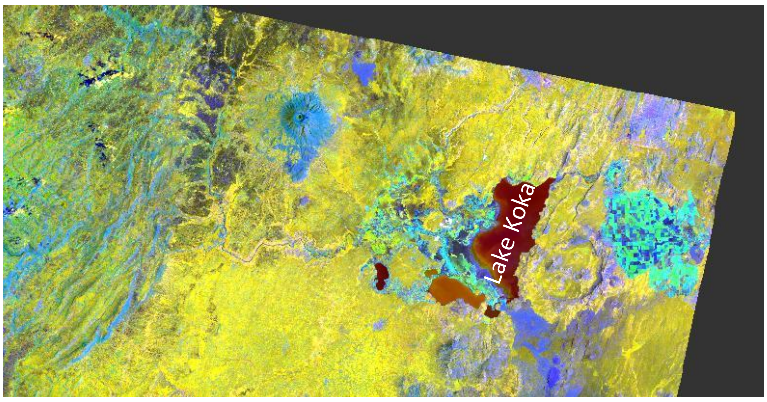

Figure 4.7: RGB composite of SAR amplitude sigma nought (blue) and Landsat 8 OLI band 2(red) and band 7 (green).

The land-cover classification was based on supervised maximum likelihood algorithm. Six major land-use/land-cover types were identified. These were dry agricultural land, bare land, irrigation land, water body, settlement and vegetation (Table 4.2).

Table 4.2 Land-use classes and areal extent of the study area.

Land Use Type	Area (km^2)	(%)
Agriculture Field	1736.16	82.35
Bare Land	48.82	2.31
Irrigated Land	56.82	2.69
Water Body	113.02	5.36
Settlement	9.98	0.47
Vegetation	143.25	6.79
Total	**2108.067**	**100**

The major land-use/cover of the study area is agricultural land. It covers 1792.98 km^2 area including the irrigated land at the time of image acquisition. The second largest land-use/cover is vegetation which is mainly distributed in the highland and along the Rivers and has an area of 143.25 km^2. The other land cover is settlement accounted for 9.98 km^2 area. Water body, and bare land have 113.02 km^2 and 48.82 km^2 area coverage, respectively. Figure 4.8 below depicted the land-use/land-cover map derived from the supervised classification method.

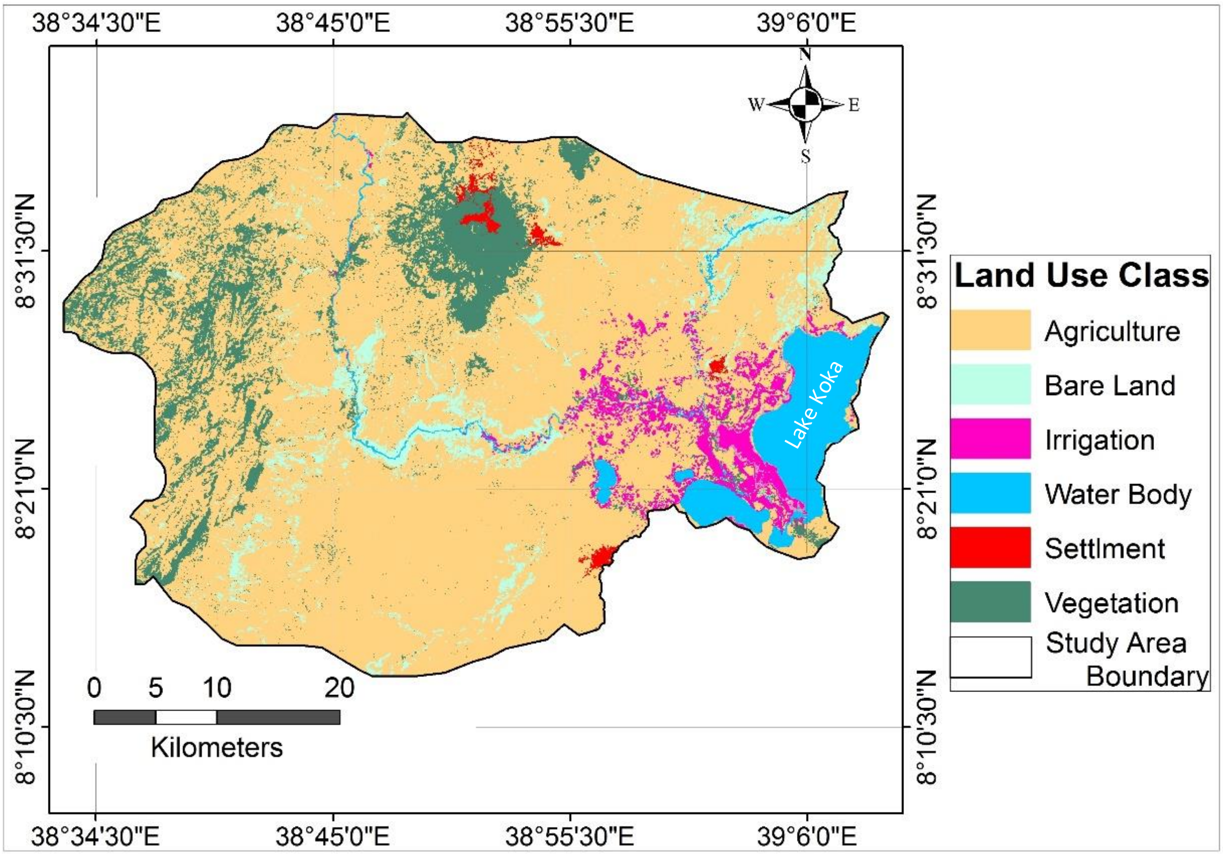

Figure 4.8: The Land-use/cover of the study area

The proportion of the land-use/land-cover indicated in Figure 4.9, showed that the dominant land-use/cover in the study area is agricultural land.

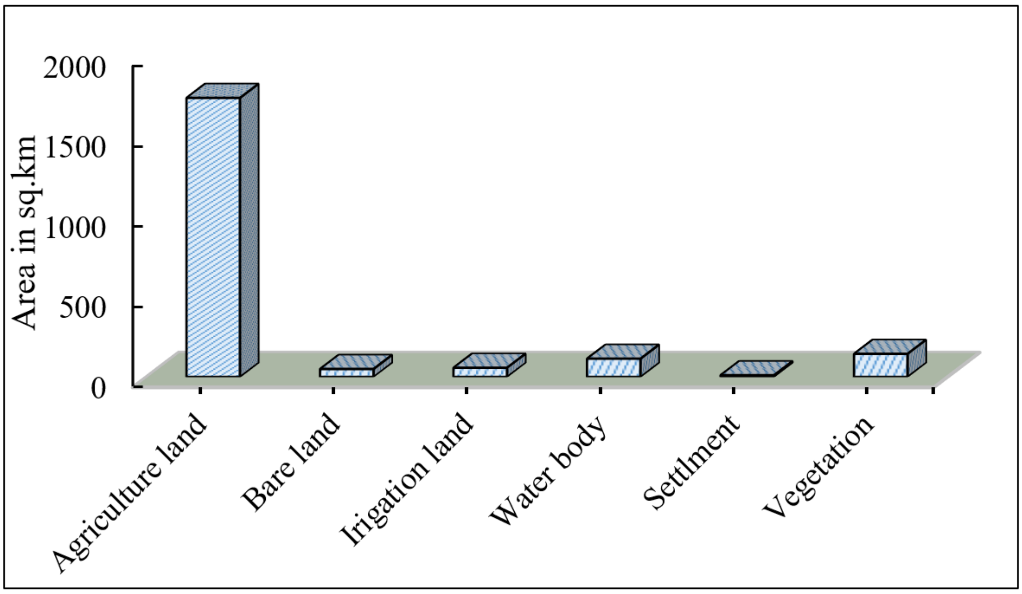

Figure 4.9: The land-use/cover class area coverage chart

4.1.2.1 Accuracy Assessment of Land-use/cover Classification

The supervised classification accuracy described in Table 4.3 was based on the 60 test samples of the land-cover classes. As the area has not complex land-use/land-cover types, such medium size of reference classes were selected for the accuracy assessment.

Table 4.3 Confusion matrix for the classified image.

	Reference Classes								
Classified Classes	Agriculture	Vegetation	Bare land	Irrigation	Settlement	Water	**Row total**	**Producers accuracy (%)**	**Users accuracy (%)**
Agriculture	**21**	0	0	1	1	0	**23**	95.45	91.30
Vegetation	0	**5**	0	0	0	0	**5**	83.33	100
Bare Land	0	0	**1**	0	0	0	**1**	100	100
Irrigation	0	0	0	**6**	1	0	**7**	75.00	85.71
Settlement	1	1	0	1	**19**	0	**22**	90.48	86.36
Water Body	0	0	0	0	0	**2**	**2**	100	100
Column total	**22**	**6**	**1**	**8**	**21**	**2**	**60**		

The overall classification accuracy which is 90.0% and the overall Kappa statistics (0.86) indicated that the land-use/land-cover classification accuracy was an acceptable result.

4.1.3 Backscatter Analysis of Land-cover Test Classes

The analysis of multi-temporal synthetic aperture radar data was performed to investigate the general backscatter behavior of several land-cover classes in the context of flood mapping. This statistical analysis of the time series data was carried out for six test classes of land cover types, each consisting of several test areas. The test class polygon areas were selected and manually digitized after review of available high resolution optical sensor - Google Earth image. These test classes were then validated with the field observation conducted from 17 April to 22 April, 2017 for five days. The test class (Table 4.4) were: 1) open water; permanent free surface region, 2) agriculture land; both the dry farm land and irrigated land, 3) bare soil; areas of bare soil during the acquisition time, 4) vegetation cover; the upland and Riverine vegetation, and 5) areas on before and after flood event.

Table 4.4 Mean backscatter coefficient (σ^0) of test classes in dB.

Test Class	22-03-2016 backscatter value (dB)	15-04-2016 backscatter value (dB)	09-05-2016 backscatter value (dB)	Change in backscatter value (ΔdB)
Vegetation	-11.48	-8.43	-10.50	Δ-3.05 – Δ-0.98
Open water	-22.33	-21.84	-21.58	Δ-0.49 – Δ-0.75
Agricultural land	*-12.32*	-8.73	-10.03	Δ-3.59 – Δ-2.29
Bare soil	-15.66	-11.31	-9.82	Δ-4.35 – Δ-5.84
Flooded area	-	-19.98	-21.97	Δ-7.68 –Δ-8.59

The mean backscatter coefficients of the five main land cover types were presented in Figure 4.10. It represents the time series of the mean backscatter coefficients for each land cover type. It is observed that the backscatter coefficient of the test classes have shown temporal variation in their reflectance value towards the SAR C-band sensor. The backscatter value of test classes except the open water test class, showed increment in April and May, 2016 seasons.

Open water has the lowest backscatter value which is below -20 dB. This indicated that the water surface has a specular reflectance property as the transmitted signal is reflected away from the SAR sensor. This has resulted in black appearance of the permanent open water surface. The vegetation test class is concentrated between -11.48 dB – -10.50 dB. Agricultural land and bare soil has relatively wider variation than vegetation. These two classes range from -12.32 dB up to -10.03 dB and -15.66 dB up to -9.82 dB, respectively.

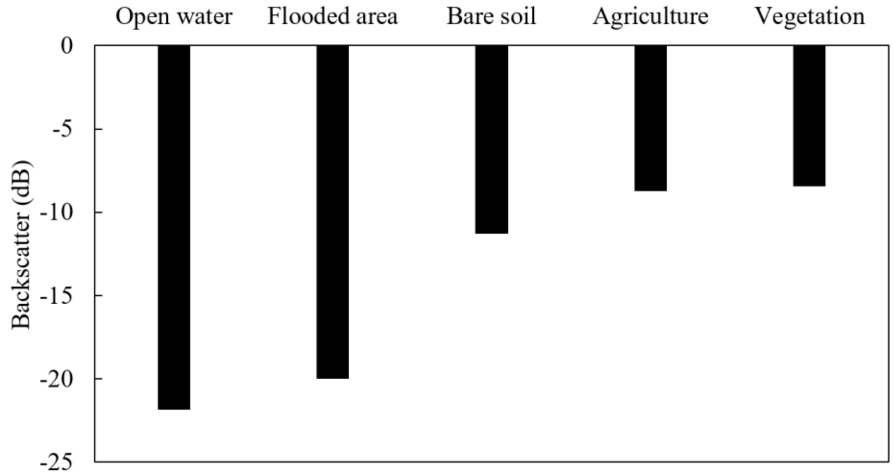

Figure 4.10: The temporal mean backscatter coefficient of the test classes.

Flooded area showed highest backscatter variation from its counter non-flooded area. It is about -20 dB with the variation of Δ-7 dB intensity value from the non-flooded value of -13.0 dB.

The vegetation test class showed the lowest temporal backscatter coefficient variation from -11.48 on 22 March to -8.43 dB on 15 April, 2016 and from -11.48 on 22 March to -10.5 dB on 09 May, 2016 (Fig.4.11). Its seasonal variations is about Δ-3.05 and Δ-0.98 for April and May, respectively from the reference 22 March image. Slightly the highest value occur in 15 April, 2016 (i.e. -8.43 dB).

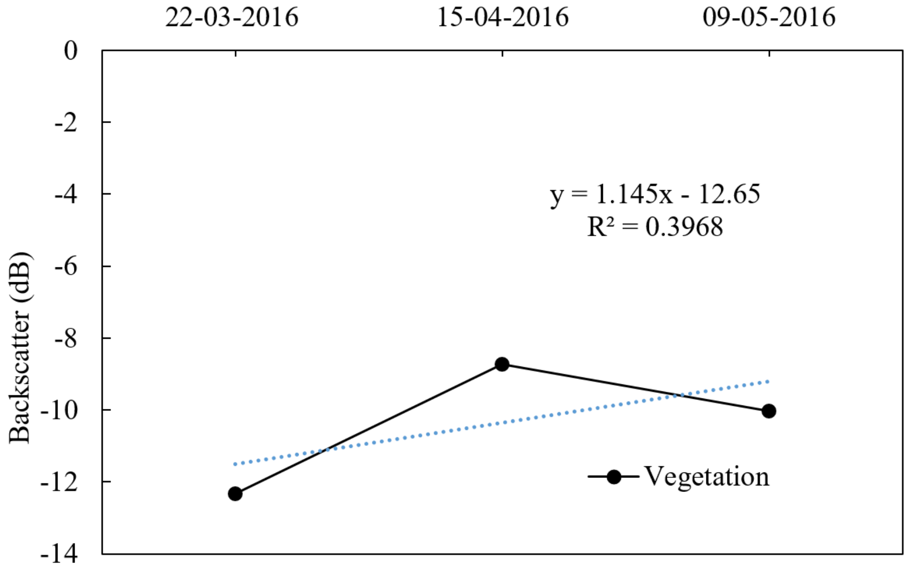

Figure 4.11: Seasonal mean backscatter of vegetation.

On the other hand, it is observed that the backscatter value of vegetation test class has shown decrement from -8.43 dB to -10.50 dB. This reduction in intensity may be due to the vegetation condition such as the decrease in canopy density or the start of leaf-off period.

Figure 4.12 below showed that the temporal variation of backscatter value of the agricultural land test class ranges from its lower value of -12.32 dB to the maximum value of -8.73 dB. The highest σ^0 value was recorded on 15 April 2016 (-8.73 dB) and the lowest was in 22 March, 2016 (-12.32 dB). The lower backscatter observed in May, 2016, was due to that, the test class taken for agricultural land were from the irrigation farm land at the time of acquisition. This month is usually when temporal changes in irrigation crop condition takes place. At a final date of production the leaf area index and biomass level is reduced. This crop condition has resulted less backscatter of the SAR pulse towards the sensor.

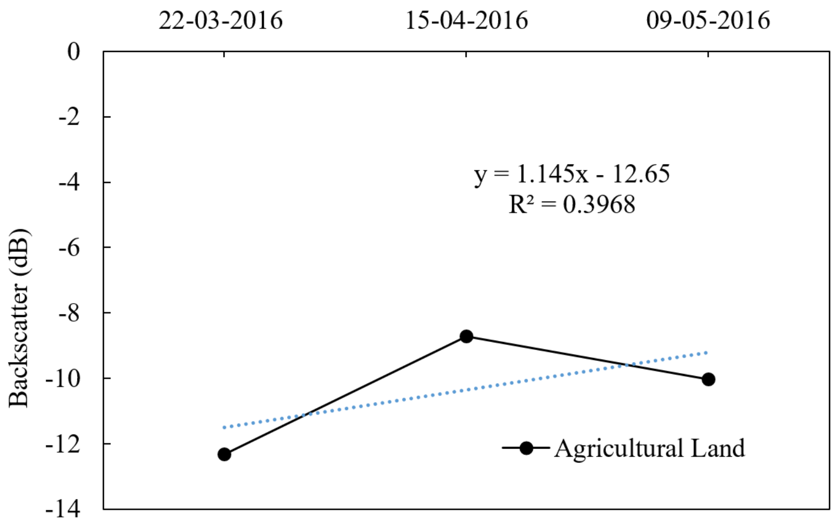

Figure 4.12: Seasonal mean backscatter of agriculture.

Due to the moisture property of the soil, the test class of bare soil has shown higher backscatter values compared to bare soil values during the low water season. The higher backscatter value could be the covering of the soil with newly growing of seeds of different weeds and crops. The flat dry bare soil is usually considered as lower backscatter feature. The bare soil showed a continuous increase throughout the time series of the SAR C-band sensor images in the present study. It reached its peak on 09 May, 2016 with the value of -9.82 dB (Fig. 4.13). The lowest seasonal intensity were observed for the 22 March, 2016 with -15.66 dB during the low water season.

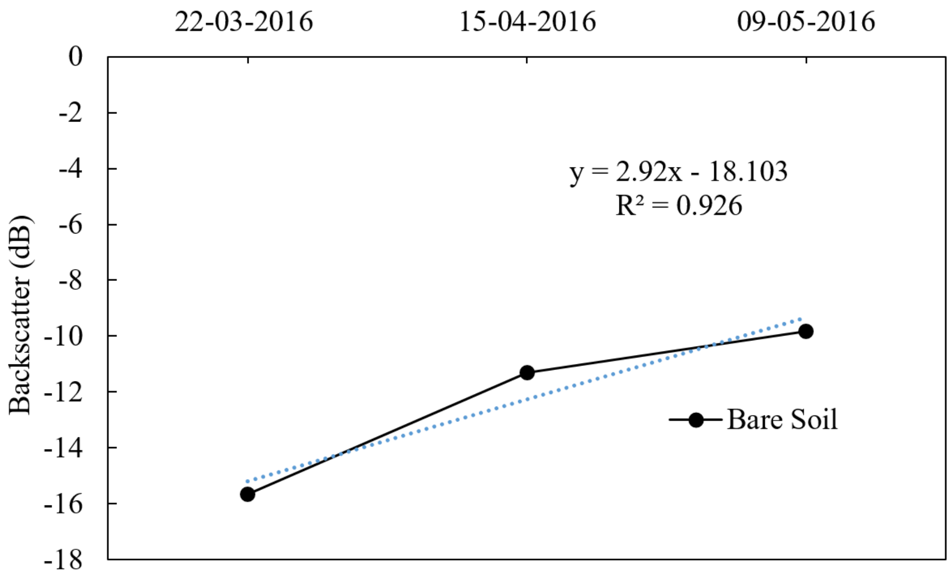

Figure 4.13: Seasonal mean backscatter of bare soil.

Permanent water shows a fluctuation of σ^0 over the three months course of the time series SAR images (Fig. 4.14). To eliminate the effects of inflows, Riverine vegetation and water level changes, only big isolated water bodies (Lakes) were selected as test class of open water. Accordingly, the mean backscatter for these big water bodies varies between −22.33 dB −21.84 dB and -21.58 dB for March, April and May, 2016 respectively. As all data were acquired within the same incidence angle range this fluctuation can be related to different surface roughness conditions due to wind effects (turbidity) and seasonal freezing effect of flood water entering to the open stable water bodies - Lakes. In addition to this, the presence of floating materials on the open permanent water bodies resulted in changes of the high value of σ^0.

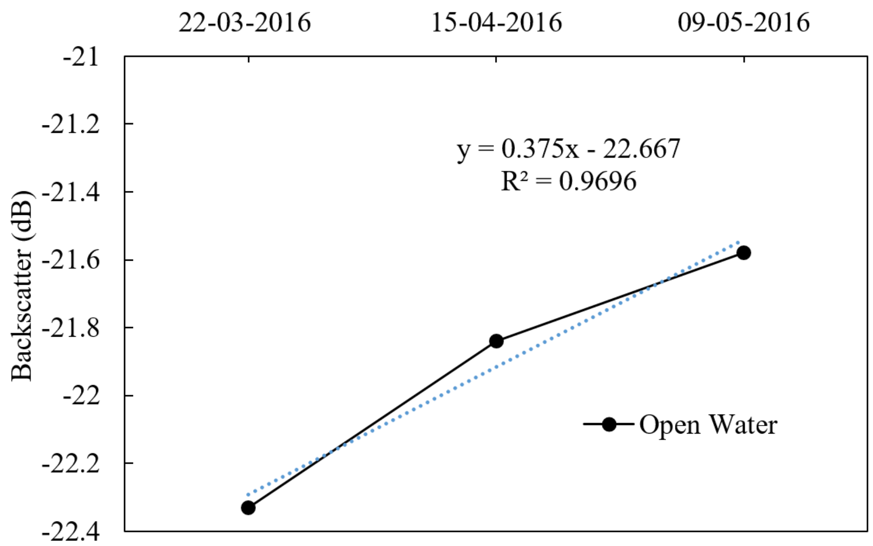

Figure 4.14: Seasonal mean backscatter of open water.

The maximum backscatter value of the open water surface was set as a threshold for separation of water surfaces from all other land cover classes. It was assumed that values below the defined backscatter limit corresponded to specular reflection from open, calm water surfaces. It is important to take the maximum value of σ^0 as a separating point of water and non-water class.

The comparison between the backscatter value of the flood area test classes and the non-flooded condition provides the separability of the two classes (Fig. 4.15). The backscatter value for the two crisis SAR images were -19.60 dB and -19.60 dB for 15 April and 09 May, 2016 respectively. The flooded area test class shows the highest change in σ^0 value. The mean backscatter differences ($\Delta\sigma^0$) between the flooded and the non-flooded areas of April and May, 2016 were -7.30 and -6.57 dB respectively. The reference test area for flooded pixels were observed with a value of -12.30 dB backscatter for April flood time , and the reference test class area that was flooded in May, 2016 accounted for a value of -13.39 dB. The test class areas were selected from the reference image with the same location in the crisis images.

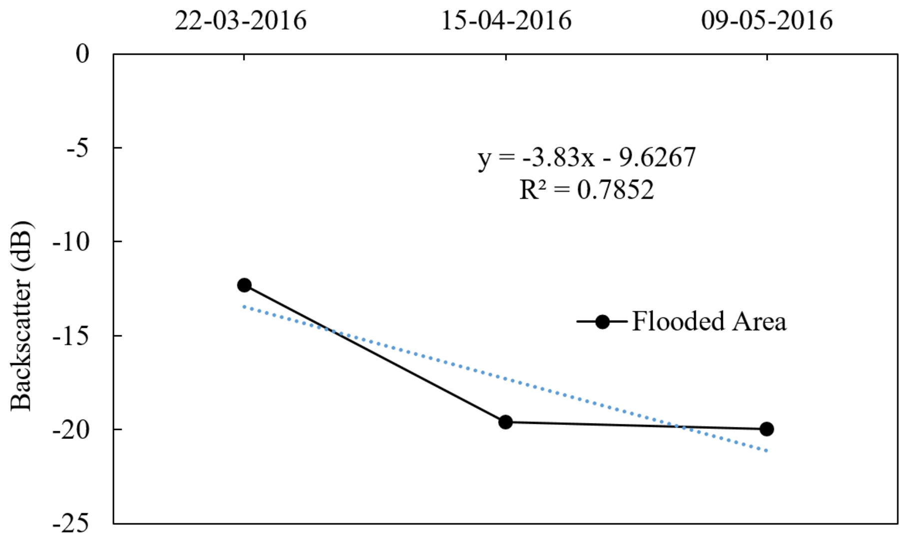

Figure 4.15: Seasonal mean backscatter of flooded area.

The flooded test classes can be easily distinguished with the threshold of the variation in the backscatter values of the time series images. In Figure 4.16, it is observed that the backscatter value of water lies in between the -15.25 dB and -24.38 dB. The optimum threshold value was -19.96 dB (Fig.4.17b).

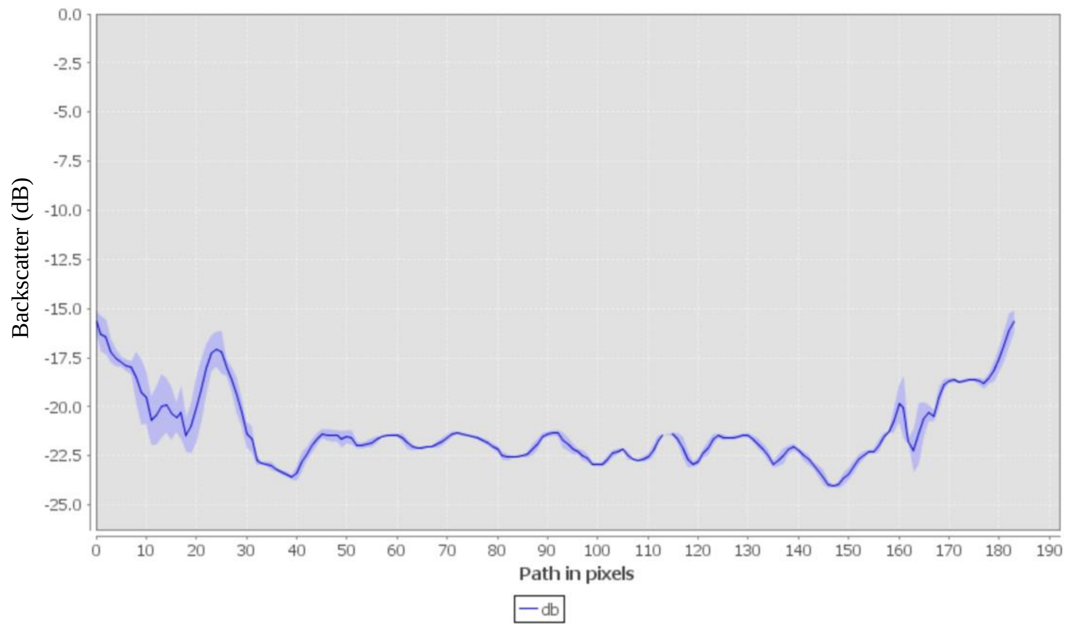

Figure 4.16: Profile of flooded area test class.

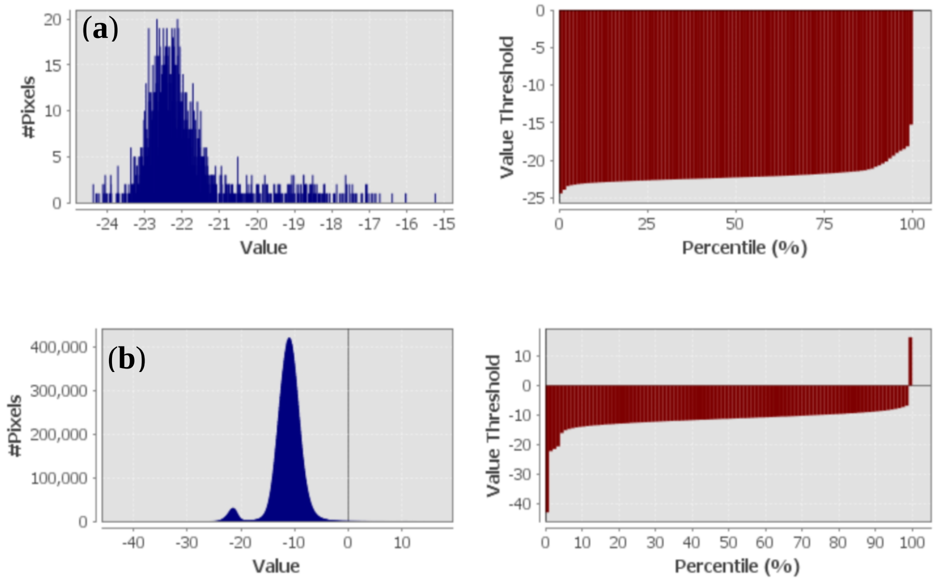

Figure 4.17: Histogram and threshold percentile of **a**) flood mask test area and **b**) the whole crisis image.

The image histogram which is a graphical representation of the tonal distribution in a digital image provided an ease in the histogram based threshold setting process (Fig. 4.17). Particularly in time series SAR images, the gray tonal variation of the images of the same scene acts as a better way of histogram thresholding system. Table 4.5 showed the threshold value that identified the discrimination point of flood water (short time change) from other dry surfaces.

Table 4.5 Backscatter statistics of the flooded area test class.

	Backscatter value(in dB)
Minimum	-24.3892
Maximum	-15.255
Mean	-21.980
Median	-22.26
Coefficient of variation	-0.0542
P75*	-21.75
P80	-21.59
P85	-21.37
P90	-19.97
Maximum error	0.009

P75*: Percentiles in threshold value.

The maximum percentile (P90) provides the optimum backscatter threshold value of the flooded area test class which is about -19.97dB. With the visual analysis of the histogram of the crisis and reference SAR time series images, the automatic threshold value was assigned. Using this threshold (-19.97dB), the permanent and flood water classes were discriminated.

4.1.4 Backscatter Thresholding using SAR Image Histogram

Thresholding was used to create binary images from a grayscale SAR images. As thresholding is the key parameter process in the choice of the threshold value, manually user chosen and automatic thersholding systems were applied. The histogram of the time series images below in Figure 4.18 showed the point where the changes in the pixel values takes place in the crisis image.

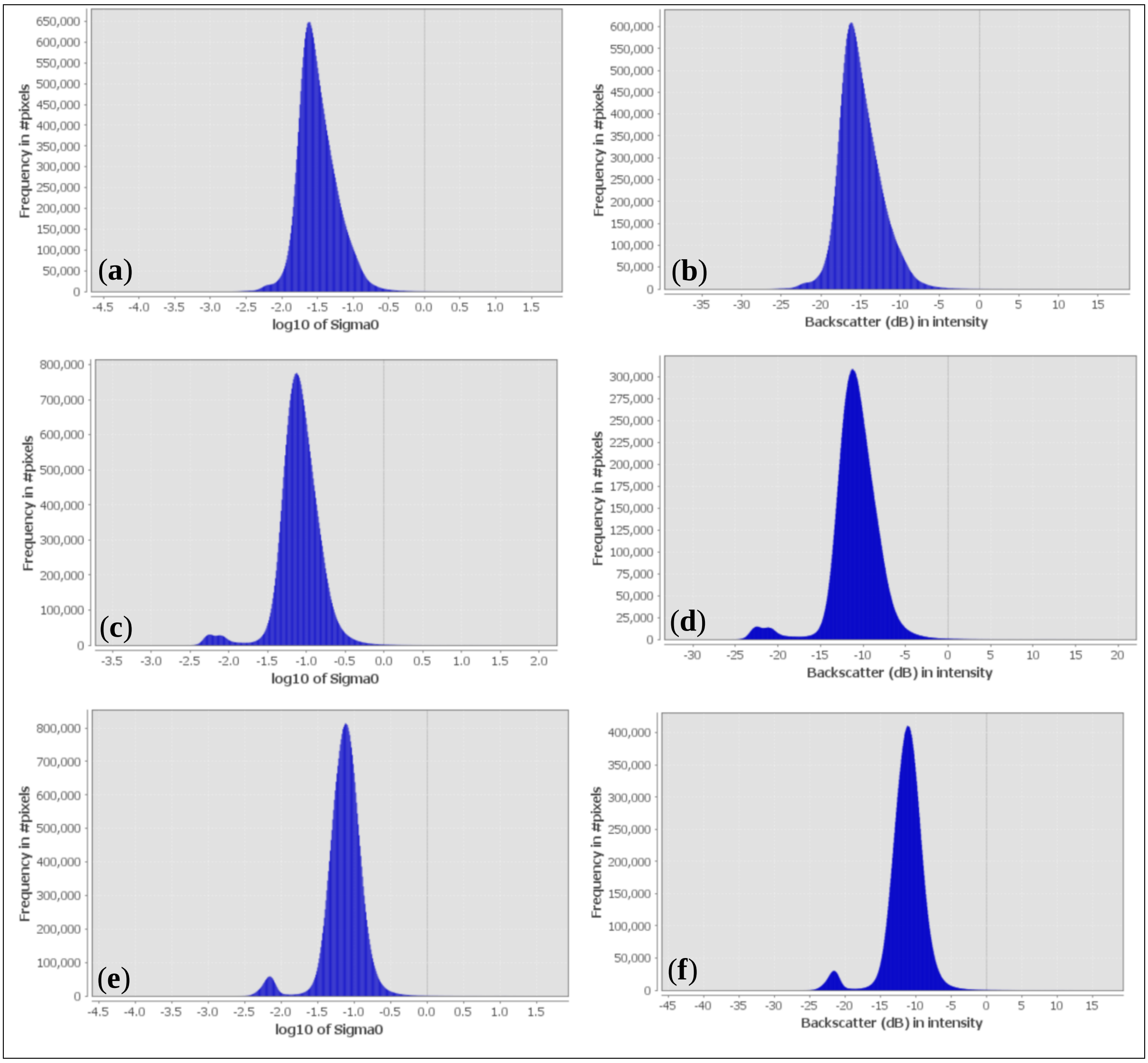

Figure 4.18: Histogram of **a)** sigma0 for 22 March 2016 reference image, **c**)15 April, 2016 crisis image, **e**) 09 May, 2016 crisis image and logarithmic backscatter of **b**) reference image **d**) April and **f**) May crisis image.

The manual selected threshold was almost similar with that of the highest percentile threshold of the backscatter value of the crisis image statistics. The manual selected threshold value is lied at the valley of the histogram which is approximately -19.5 dB (Fig. 4.18 d, f).

In the automatic threshold selection, a simple method was chosen. This was based on the maximum percentile threshold value of the filtered SAR crisis image statistics. In the present study, the threshold value for discrimination of the flooded water from non-flooded was set as -19.97 dB. It is obtained from the flood image statistics. The threshold value indicated fits the characteristic of SAR image histogram and behavior of water object in the SAR sensor. The backscatter below this value of the intensity of the crisis images was regarded as water, whereas pixels with intensities of above this threshold were regarded as other land surfaces.

4.1.5 Extraction of Flooded Areas from SAR Image

In flood extraction three tests have been carried out using SAR images acquired during different flood events. In this paper the results related to a flood event occurred in Awash River on 15 April and 09 May, 2016 were extracted and mapped. The images used were Sentinel-1 IW descending mode of VV polarization. The three methods applied on SAR images were band subtraction, band ratio and principal component difference. The flood extent map obtained from the three different methods were compared and evaluated. Each flood detection method was applied on the two crisis image of 15 April and 09 May, 2016 with reference SAR image of the 22 March, 2016.

To extract the flood inundation pixel from permanent open water, a mask which comprises the water bodies, River and Lakes areas were applied to the output layer derived from thresholding process. Mask layer is prepared from pre-flood SAR data. Finally, a single bit flood inundation layer was exported to geotiff format from its BEAM DIMAP format of the SNAP. Then using Arc GIS 10.2, flood extent image was generated containing flooded (grid code = 1) and non-flooded (grid code = 0). This raster image was converted into vector polygon features and further refining of the flood inundation layer is carried out by Arc GIS environment. It was done by grouping and removing falsely detected pixels as flooded. To decide which polygons are candidates for being flood water surface or to avoid depressions (pits) that collect water, the flood polygons were overlaid on the high spatial resolution optical image acquired after the flood occurrence.

In the band subtraction method, the 22 March, 2016 reference image was subtracted from crisis image of 15 April, 2016. The PCA was applied on the reference and April crisis images. The first component of the reference and crisis images were taken and staked for PCD. The results of the 15 April, 2016 flood, using the three change detection approaches are demonstrated in Figure 4.19 (d, e, and f) as change log rato image, where the inundated area appears in white while all the other coverage appears in black of the change log ratio images. In particular, for method of band subtraction, illustrated in Figure 4.19d, the detected flooded area was comparatively continuous in its extent.

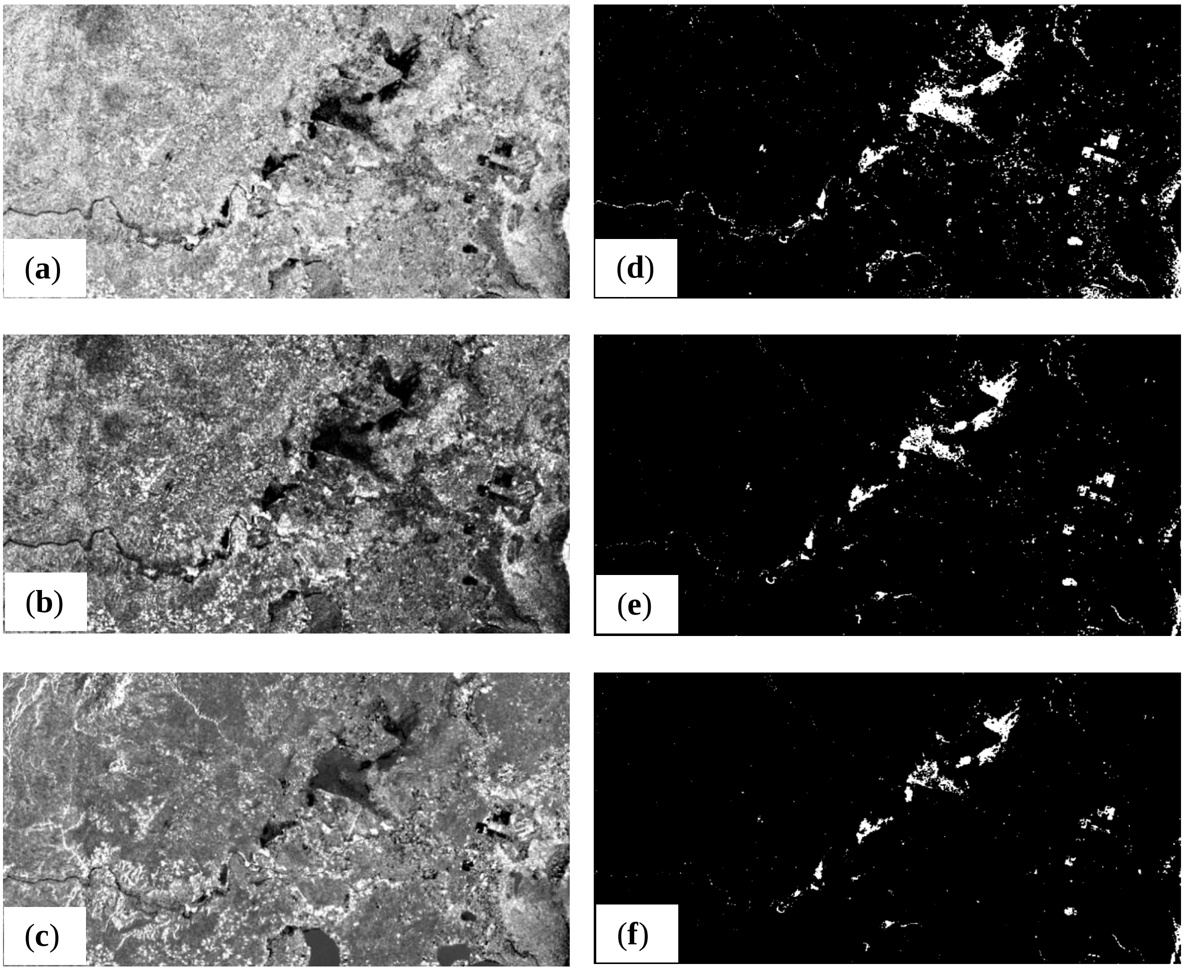

Figure 4.19: **a**) Band difference, **b**) band ratio, **c**) PCD and **d, e, f)** change log ratio images of the reference and 15 April, 2016 crisis images.

It was observed that the flood extent of the first method the band subtraction was calculated to be 24.12 km^2. The flooded area in the band ratio and PCD methods was calculated as 23.22 km^2 and 20.67km^2 respectively. The total flood extent occurred on 15 April, 2016 by band subtraction and ratioing was almost similar. The comparison of these two methods confirms that in the present case study the flooded area derived from the SAR images had almost the same quality and differences between the two maps are rather insignificant (Fig.4.20). However, the result of the third method, the PCD approach, shown in Figure 4.19f, exhibits variation compared to the other two methods. It showed the variation of 3.45 km^2 from the band subtraction and 2.55 km^2 from the band ratio method. Figure 4.21 demonstrates the comparison between the three flood extent mapping approaches for April, 2016 flood.

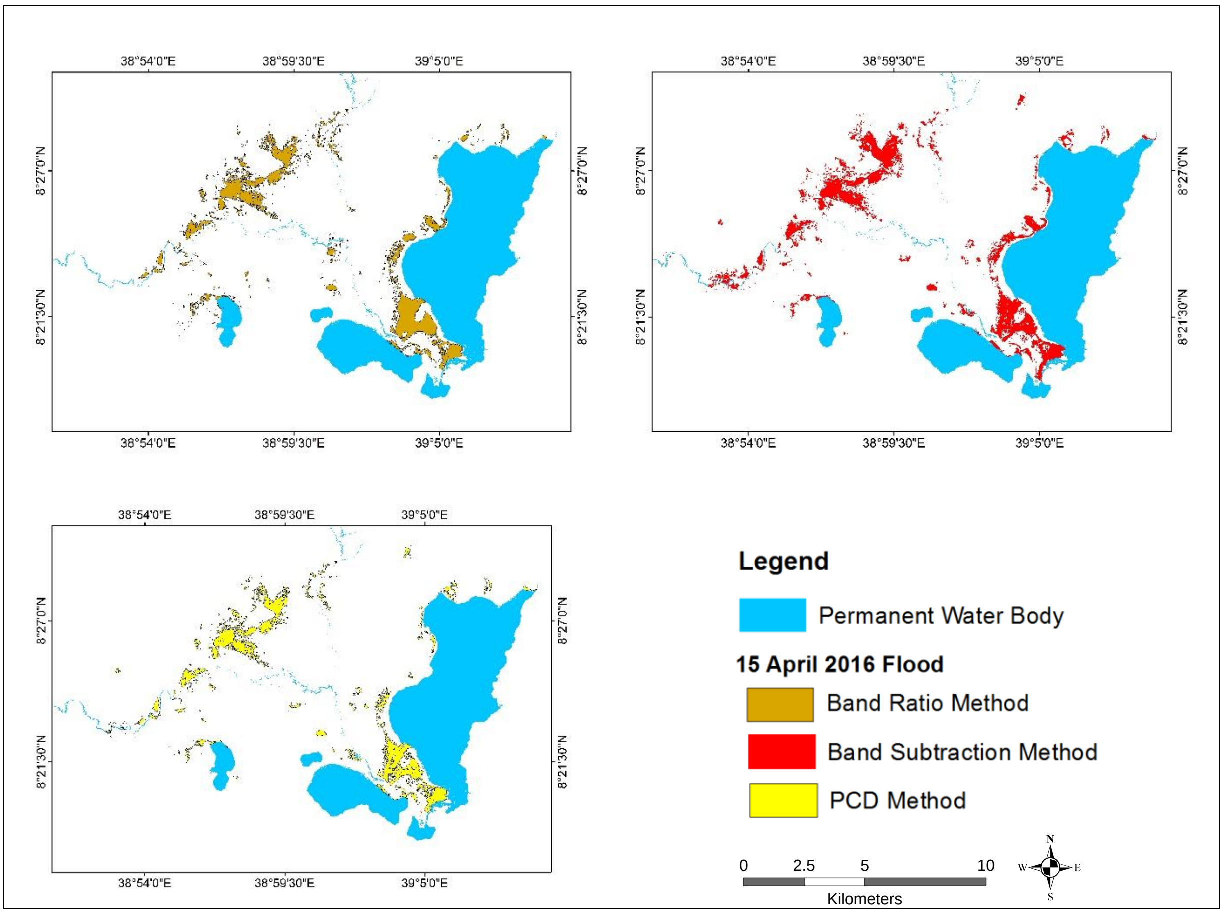

Figure 4. 20: The 15 April, 2016 flood extent map of the study area using band ratio, band subtraction and Principal component differencing methods.

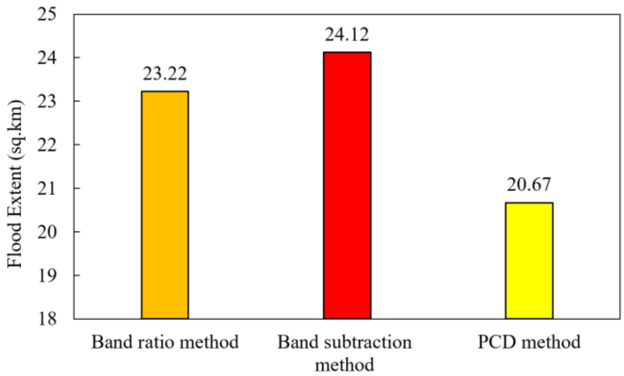

Figure 4.21: The 15 April, 2016 flood extent calculated from the three change detection approaches.

The reduction of the flood extent map using the PCD method could be accounted from the data dimension reduction or to the data decorrelation in the process of PCA. As data compression or data dimension reduction is the distinct function of PCA for feature extraction, the decrement in flood extent of the present study might stem from the compression of the information in to one containing major component of the SAR image.

In the same way the three change detection methods were applied on the 09 May, 2016 crisis image. Results from the three different approaches for SAR image were presented for analysis and comparison. The comparison is based on the flooded areas detected from each algorithm. Figure 4.22 showed extracts of the flooding areas of 09 May, 2016 derived from the aforementioned approaches.

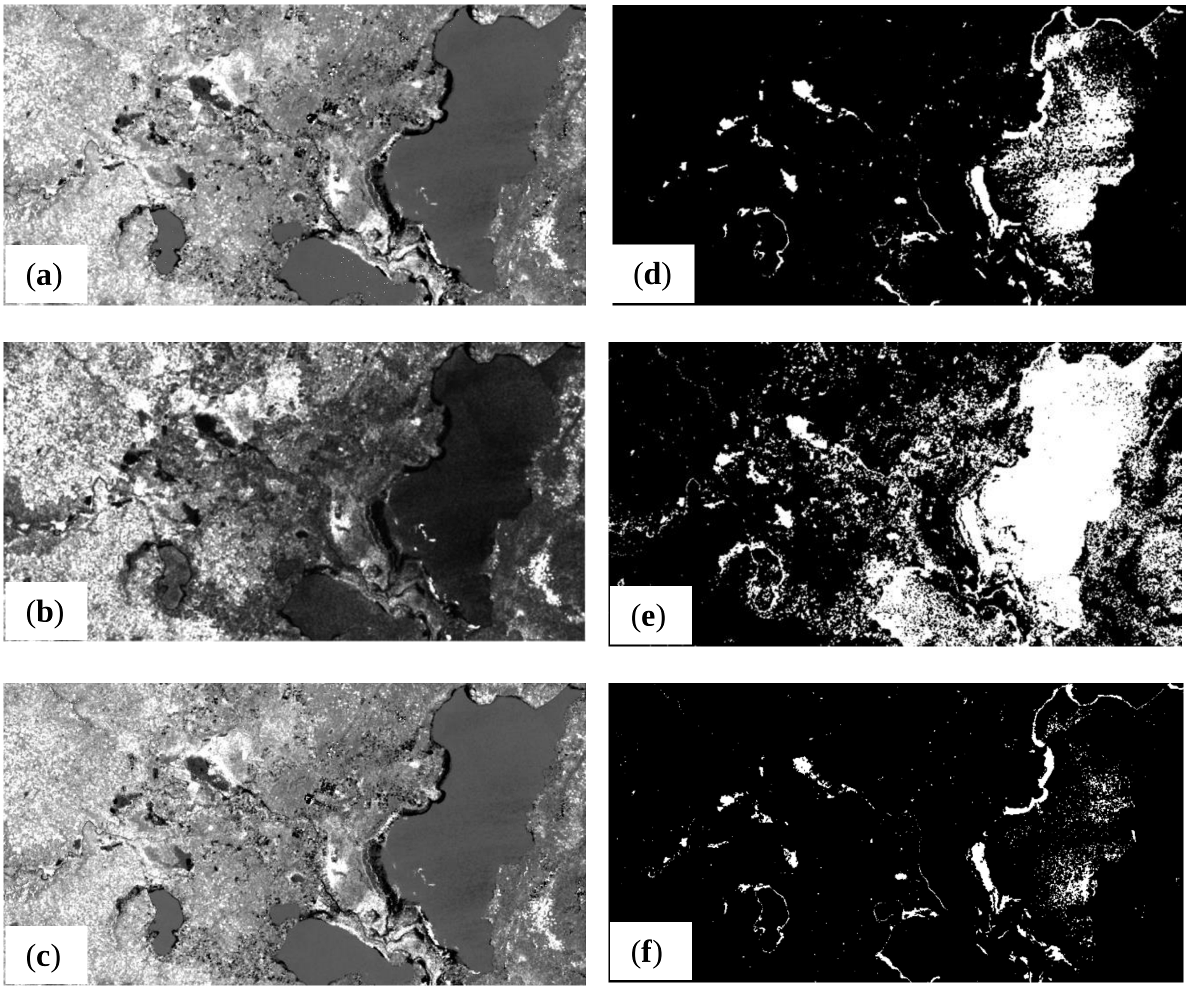

Figure 4.22: **a**) Band difference, **b**) band ratio, **c**) PCD and **d, e, f)** change log ratio images of the reference and 09 May, 2016 crisis images.

The results of the change log ratio images of band subtraction and PCD methods relatively match the geometry and appearance of the flooding zones (Fig. 4.22 d and f) of the difference images. However, the band ratio method, demonstrated in Figure 4.22e, showed highly disturbed change log ratio image. The change detection algorithm highlights the effect of turbidity on the water surface as a change. This needs caution in extraction of the actual flooded pixels. The flood extent of May, 2016 is portrayed in Figure 4.23. The flood extent map derived from the band subtraction was calculated to be 17.63 km^2. The other methods band ratio and PCD accounted for 17.3 km^2 and 15.7 km^2, respectively.

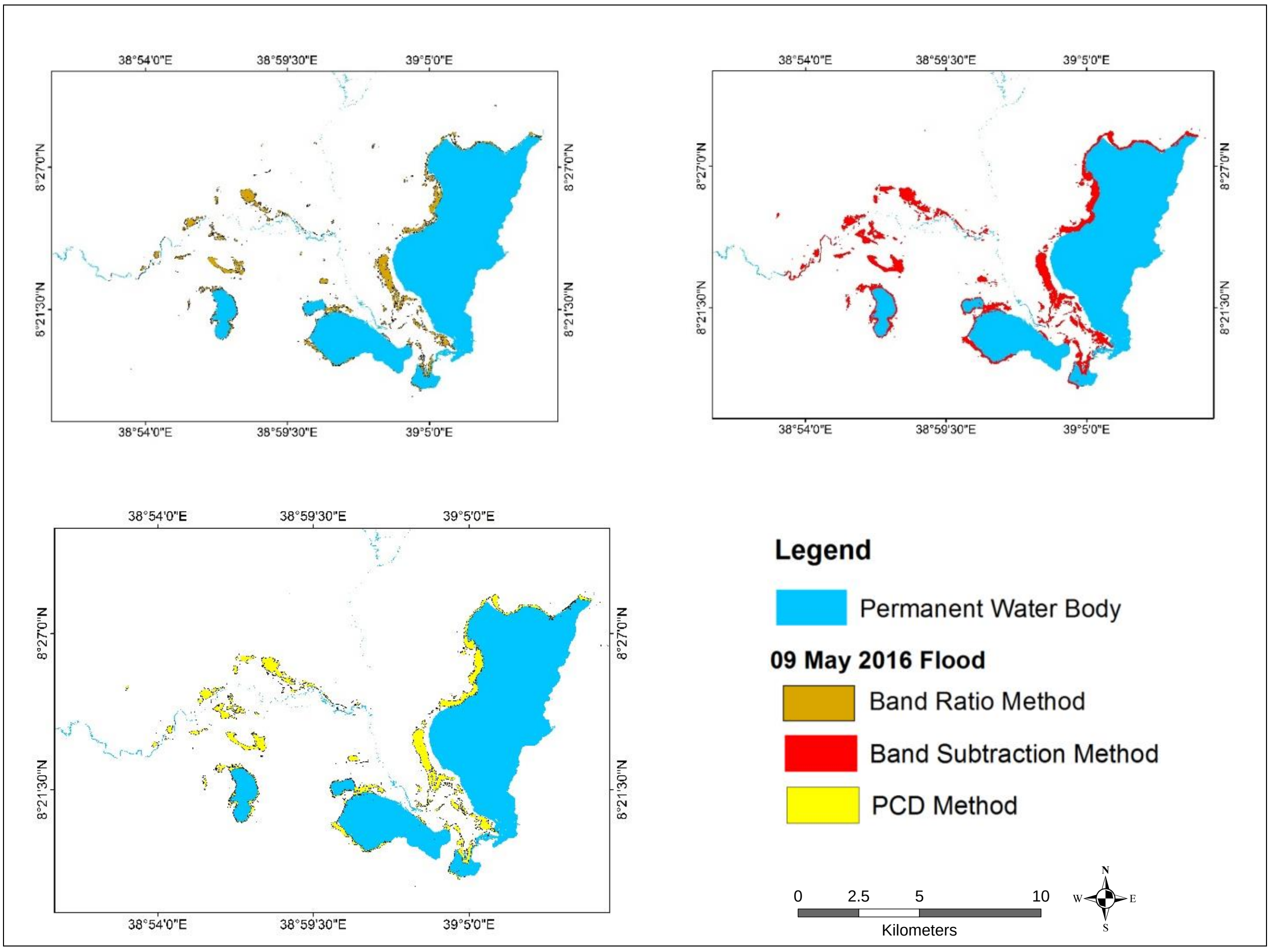

Figure 4. 23: The 09 May, 2016 flood extent map of the study area using band ratio, band subtraction and Principal component differencing methods.

In the band ratio method which resulted noisy and false alarm flood area pixels, a detail user intervention refinement was performed with visual interpretation of the filtered SAR reference and crisis images. The extracted flood areal coverage using the three change detection methods is shown in Figure 4.24.

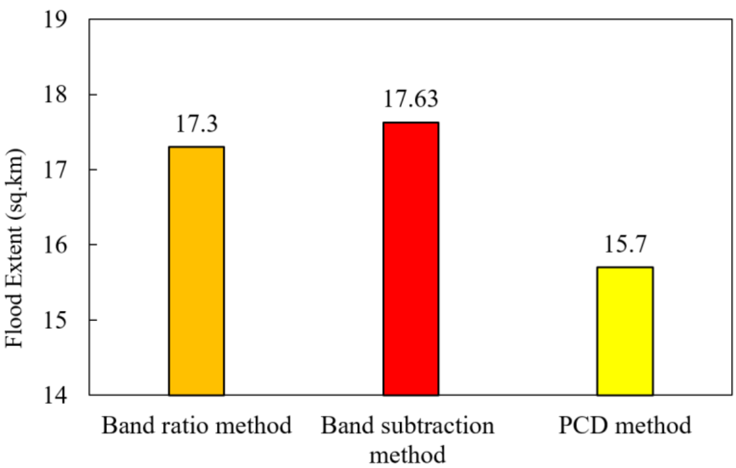

Figure 4.24: The 09 May, 2016 flood extent calculated from the three change detection approaches.

The comparison of these methods demonstrates that the effectiveness of the change detection dedicated to flood mapping lead to better performance with the band subtraction and band ratioing approaches (Fig. 4.25).

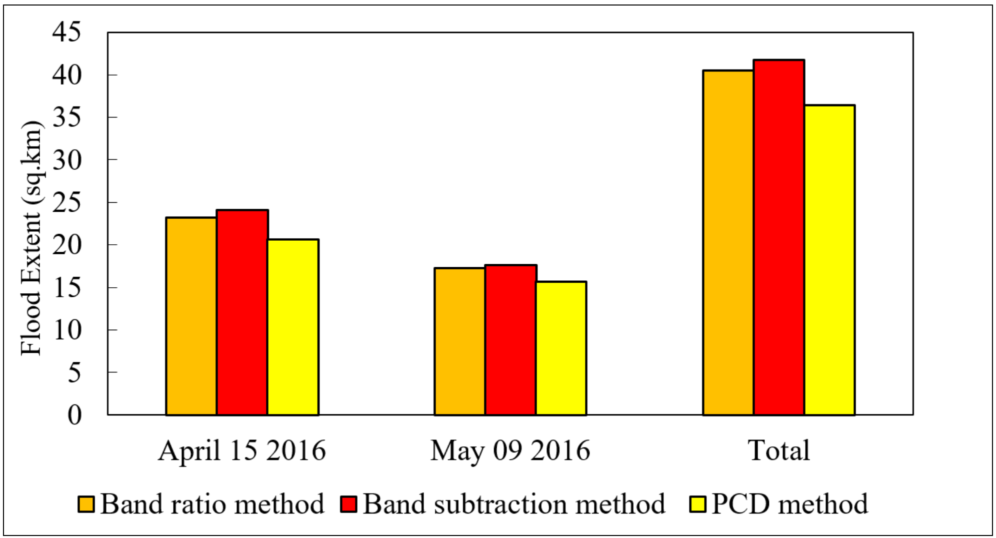

Figure 4.25: Comparison of the performance of the three change detection methods.

The total flood extent occurred on April and May, 2016 calculated from each methods showed that band subtraction algorithm exhibited better performance, i.e. the flooded area was 41.75 km^2 (Table 4.6) followed by band rationg (40.52 km^2) and PCD (36.37 km^2) . The flood extent of 15 April, 2016 was higher than that of 09 May, 2016.

Table 4.6 Flood extent of 15 April and 09 May, 2016 using the three methods.

Flood Detection Methods	**15 April 2016 flood Area (km^2)**	**09 May 2016 flood Area (km^2)**	**Total Area**
Band ratio method	23.22	17.30	40.52
Band subtraction method	24.12	17.63	41.75
Principal component difference method	20.67	15.70	36.37

In each of change detections method, it was observed to be higher. The proportion of the total flooded area from the total land area of the present study was 1.98 %. The total flooded area by 15 April, 2016 was 40.52 km^2, 41.75 km^2 and 36.37 km^2 for band subtraction, band ratio and PCD methods, respectively. For 09 May, 2016 it was 17.63 km^2, 17.3 km^2, 15.7 km^2 from band subtraction, band ratio and PCD algorithms, respectively. Figure 4.26 represented the flooded area extent of the two crisis months of the year 2016 in the study area.

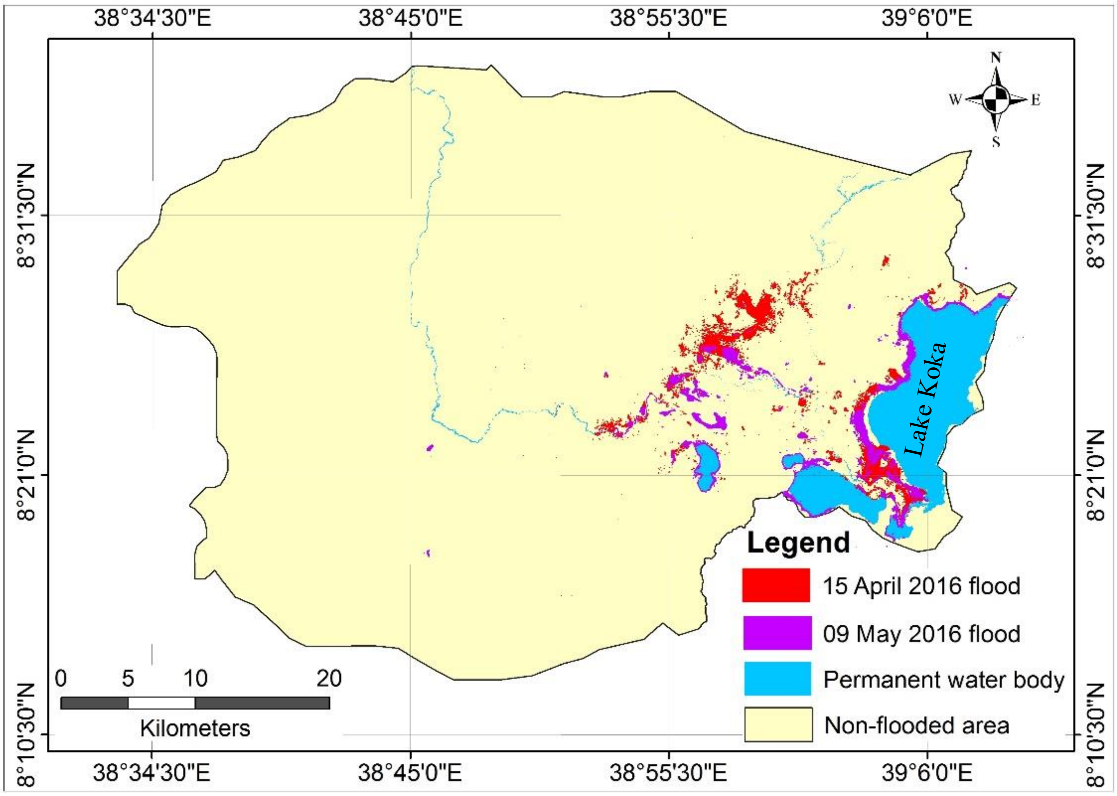

Figure 4.26: Flood extent map of the study area

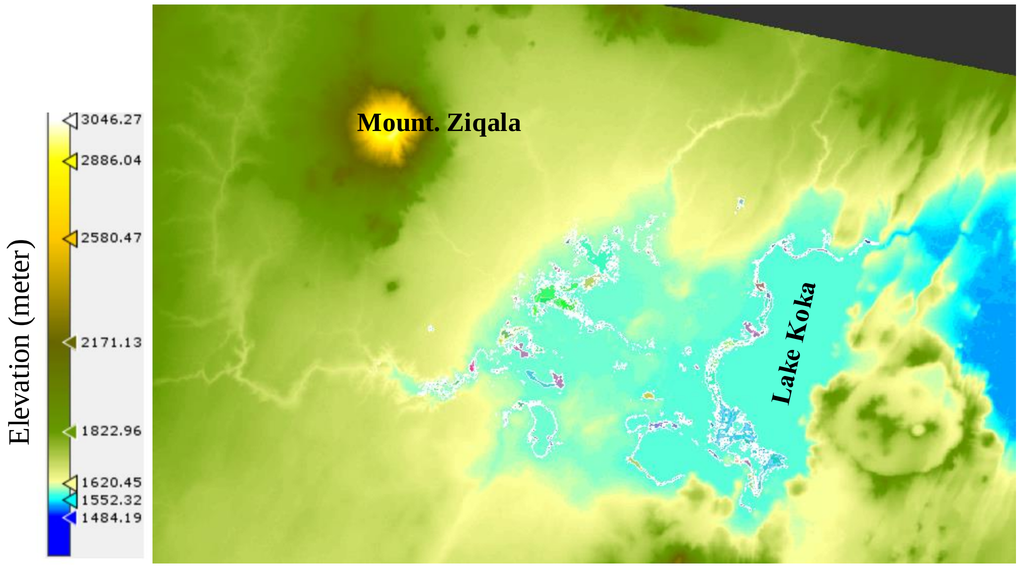

Figure 4.27: Flooded area polygon overlaid on the elevation of the study area

The flooded areas have an elevation ranging from 1552. 32 to 1620.45 meters above mean sea level with less than 3º slope. The area below this slope is regarded as highly vulnerable for flooding.

4.2 Discussion

The use of sentinel-1 C-band microwave image in flood detection and mapping has various advantages. In the first place the energy from the radar signals can penetrate through the cloud and rainfall. Its ability to detect features at day and night is another instance of the preferability of using the microwave technology for near real-time flood detection. Flood inundation mapping using SAR sensors is preferred to visible and infrared band sensors. As explained in work of Giustarini (2015), because of their ability to penetrate clouds that are often present at times of flood and the ability to obtain a synoptic view of the inundation extent, regardless the light and weather conditions, SAR represents an extremely important feature for operational flood relief management.

The investigated methods used in the flood detection and mapping of the present study was based on the generation of change SAR time series images. The study of Benoit (2007) implied that the use of multi-temporal SAR data provides more accurate flood detection and mapping. The single date SAR image flood detection and mapping could result in miss-assignment of radar image pixels unless other reference image is used. The reference high spatial resolution radar image should always be used in the processes of masking out the flooded area from the non-flooded.

The horizontal-transmission and horizontal-reception as well as vertical-transmission and vertical-reception polarizations provide a more suitable discrimination of flooded areas than other combinations, such as horizontal-transmission and vertical-reception, vertical-transmission and horizontal-reception and the vice versa. The vertical-vertical polarization that was used in the present study, provided confidential flood extent results from the multi-temporal Sentinel-1SAR images.

Change detection technique is the robust approach for flood area identification and mapping. As in the work of (Al-doski et al., 2013) for change detection using radar technology, the reference time (t_1) and crisis time (t_2) images are important in the processes of analyzing the change occurred at a particular time. The reference image provides the knowledge of the dry or non-flood scenes of the SAR image (Long et al., 2014). Change detection algorithms analyze multiple images of the same scene taken at different times to identify regions of change. The change detection methods adopted in the present study were fast and robust techniques in microwave remote sensing for flood detection which is in line with the previous works of (Devi and Jiji, 2015; Psomiadis, 2016). Hence, through change detection it is possible to know the status of flooding of areas visualizing it in two different times-the before and after flood events. Automatic SAR change detection from images acquired from the same scene but different time is one of newly emerging topic in the near real-time flood extent mapping (Thankachan and Jose, 2014). The Synthetic aperture radar flood extent mapping through change detection from the analysis of crisis intensity test class and reference intensity class provides the better change metric flood extent (Long et al., 2014).

In the present study, the change detection for flood mapping was based on the assigned threshold value. It is the most frequently used technique to separate flooded from non-flooded areas in a SAR image (Voigt et al., 2008). The thresholding method has a main advantage of computationally relatively inexpensive and suitable for rapid mapping of the flood extent. The results from this method are reliable and commonly imperative for inundation area extraction (Krishna and Babu, 2013). It works satisfactory in flood and calm water surface extraction where water body has a specular reflection with low backscatter value of the radar wavelengths. The change detection methods the band subtraction, the band rationg and PCD are robust for short duration changes of the same scenes acquired at different time intervals (Long et al., 2014). The results of the present study derived from such change detection methods were presented in Figure.4.20 and Figure. 4.23 for the two time flood events.

These change detection techniques can be applied directly to the multiple dates of SAR imagery (Al-doski et al., 2013). The ratio and difference images are used for suppressing background information and enhancing change information (Ajadi et al., 2016). The change images from band difference, band ratio and PCD methods of flood mapping using SAR data were more effective in detecting flooded pixels in the study area. The study showed that there exists a good correlation between difference in flood inundation area and the radar backscatter values. The backscatter values of areas before flood have indicated higher backscatter value whereas the same areas after flood event showed lower radar backscatter signals.

As explained before, for the better change area identification, the threshold values for image differencing and image rationg are critical considerations. This is because of that these change detection methods showed significantly different status of change and no-change based on the threshold values (Abubakr et al., 2013). In case of the present study, the optimum threshold was selected after detail analysis of the statistical properties and histogram of each of the time series Sentinel -1 SAR images.

CHAPTER FIVE

5. CONCLUSOINS AND RECOMMENDATIONS

5.1 Conclusions

The use of SAR imagery has proven useful for a variety of flood extent mapping methods. The study investigated the potential of multi-temporal C-band SAR data for flood detection on the Awash River in the Koka catchment. The new possibilities in polarimetry, wavelength, spatial resolution and other characteristics given by the current available microwave sensors are emerging on space based flood monitoring. Microwave remote sensing data are effective means for flood hazard management. The radar systems are more advantageous in data providing related to the floodplain than the optical remote sensing systems. The capability of acquiring data at all weather and time with its shorter revisit time makes the radar sensor data preferable over optical satellite data.

In the present study, the main objective was to develop the flood extent map from multi-temporal sentinel-1 SAR images for the Awash River in Koka catchment. The advantages and challenges of the use of the very high resolution sentinel-1 SAR imagery for the analysis of flood extent in the study area was carried out. The SAR provides improved spatial and temporal resolution that resulted in better accuracy of flood extent maps and enables the possibility to represent the temporal dynamics of flood events more accurately.

Due to the existence of speckle noise in SAR images, the study presented and compared five main despeckling algorithms. The comparative test of the speckle filtering types have shown that the gamma map 7×7 filter performed better for the present study purpose. The filtering performance measurement, the equivalent number of look (ENL) for gamma map filter was observed to be higher that indicates the high quality of filtered SAR image.

This thesis also presented the general backscatter behavior of several semantic classes in the context of flood extent mapping. The backscatter coefficients were extracted for different land cover classes and traced changes of backscatter coefficients in time series SAR images. The backscatter statistical analysis of the features from SAR sensor provides useful information for the identification of the water surface from the other classes. The temporal variation in intensity (measured with σ^0) of the features of before flood and after flood occurrence provides the ease in the identification of where the changes happened in the time series images. The backscatter difference between the flooding in 15 April and 09 May, 2016 and the mean backscatter of the time course under non-flooded conditions were clearly identifiable. Flood maps were derived from the sentinel-1 SAR data and validated using a reference dry season SAR dataset. The flood area extraction technique used in the present study was the change detection which is one of the robust methods in the field of remote sensing. Several change detection methods are available, of which the methods used in this paper were band subtraction, band rationg and principal component differencing. The result of each change detection method was presented separately and compared one another.

The results from such methods demonstrated a confidential performance of SAR images for flood detection and extent mapping. Both the band subtraction and band ratioing algorithms appear to have almost similar satisfactory results. The flood extent of 15 April, 2016 were 40.52 km^2 and 41.75 km^2 for band subtraction and band ratio respectively. The PCD method showed slight flooded area decrement (i.e. 36.37 km^2). In 09 May, 2016 the flood coverage was 17.63 km^2, 17.3 km^2, 15.7 km^2 area calculated from band subtraction, band ratio and PCD methods, respectively.

5.2 Recommendations

The present study has analyzed and evaluated the microwave remote sensing for flood detection and mapping. Based on the findings of the study, the following recommendations can be drawn for future works in the so called field of study.

- Problems encountered due to the lack of acquiring regular high resolution SAR images at a peak flood time could be in some extent overcome through the use of time series SAR images as the multiple images can increase the accuracy and reliability than using single image. In addition to this, when the chance of capturing a peak flood event with the free available SAR image is low, the on-demand SAR data acquisition could be the solution.
- Polarization is one of the decisive factors in the analysis of the SAR image for extraction of flood area. The present study used the VV mode of polarization which in some extent lacks acquisition of the full flood water extent due to the horizontal nature of the flood water. Although the results from the VV polarization were promising, it could be better to use of HH polarization (if available) than VV and other dual combinations such as HV, VH, VH+VV, HH+ HV. The mode (HH) can fully capture the peak flood extent by its capability of horizontal transmission and horizontal reception of SAR signals.

- The availability of flood observation from space is of high relevance, particularly at a time of a flood disaster. The need for quick overview of the situation and detail insight of the affected area has a far-reaching relevance in the flood monitoring. It is also very important to archive to the database of the incidence of the flood over an area which is the first step in the flood monitoring and management processes. It helps decision makers and relief organizations to allocate their resources in the prevention and risk minimizing activates. Therefore, hopefully the output of this research will benefit by providing some useful reference for the flood monitoring plan in such a way that where the flood has happened and to what extent it was occurred.

REFERENCES

Abubakr, A. A. Al-Sharif, Pradhan, B., Hadi, S. J., Mola, N. (2013). Revisiting methods and potentials of SAR change detection. *Proceedings of the World Congress on Engineering*. **3:** London, U.K., 7 pp.

Aggarwal, S. (2013). Principles of Remote Sensing. Indian Institute of Remote Sensing, Dehra, Dun, India, 24−34 pp.

Ajadi, A.O., Meyer, F. J. and Webley, P.W. (2016). Change detection in synthetic aperture radar images using a multiscale-driven approach. *Remote Sensing*, **8**: 482−493.

Akbari, V. (2013). *Multitemporal Analysis of Multipolarization Synthetic Aperture Radar Image for Robust Surface Change Detection*. University of Toronto, Canada, 256 pp.

Al-Ali, Mohamed, S., Mohamed, Q. (2011). Assessment of high resolution SAR imagery for mapping food plain water bodies: A comparison between radarsat-2 and TerraSAR-X, Durham theses, Durham University, 264 pp.

Alberto M. (2013). *Synthetic Aperture Radar (SAR)*: *Principles and Applications*. Harokopio University, Greece, 342 pp.

Al-doski, J., Mansor, S. B. and Shafri, H. Z. (2013). Change detection process and techniques. *Civil and Environmental Research,* **3: 10**, 37−45.

Argenti, F., Lapini, A., Bianchi T., Alparone, T. (2013). A tutorial on speckle reduction in synthetic aperture radar images. *Geoscience and Remote Sensing*, **1: 3**, 6−35.

Arianespace Service and Solution (2016). Sentinel-1B Launch kit.

B¨uchele, B. (2006). Flood-risk Mapping: Contributions towards an Enhanced Assessment of extreme Events and Associated Risks. Natural Hazards and Earth System Sciences, Technical University of Karlsruhe, Germany, 123 PP.

Babu, M., Subramanyam, M.V., Prasad, G. (2013). Effect of speckle filtering on SAR high resolution data for image fusion. *International Journal of Engineering and Innovative,* **3: 1**, 143−153.

Bakker, H., Janssen, L.F. (2001). *Principle of Remote Sensing*. An introductory textbook. The international institute for Aerospace survey and Earth Sciences (ITC), The Netherlands, 409 pp.

Bartsch, A., Trofaier, A. M., Hayman, G., Sabel, D., Schlaffer, S., Clark, D. B and Blyth, E. (2012). Detection of open water dynamics with ENVISAT ASAR in support of land surface modelling at high latitudes. *Bio-geoscience*s, **9: 7**, 703−714.

Bayati, M. A. and Zaart, A. E. (2013). Automatic thresholding techniques for SAR images. *Computer Science and Information Technology* (CS and IT), **8: 4**, 75−84.

Benoit, R. (2007). Determination of flood Extent using remote sensing. Ph. D term paper, Department of Civil and Environmental Engineering, University of, Alberta, Canada, 17 pp.

Berberoglu, S. and Akin, A. (2009). Assessing different remote sensing techniques to detect land Use/cover changes in the eastern Mediterranean. *International Journal of Applied Earth Observation and Geoinformation*, **11:** 46−53.

Bhattacharya, A. (2014). Basics of Microwave Remote Sensing, 69 pp.

Biswajeet, P. (2009). Flood susceptible mapping and risk area delineation using logistic regression, GIS and remote sensing. *Journal of Spatial Hydrology,* **9: 11**, 775−786.

Boorman, D.B., Hollist J.M. and Lilly A. (1995). Hydrology of soil types: a hydrological based classification of the soils of the United Kingdom, Institute of hydrology, report no. 126.

Brown, B., Unger, D. and Rogers, J. A. (2000). Analysis of change in Central Texas using image differencing and unsupervised classification. Faculty presentations, Conference Paper.

Carver, K., Elachi, C. and Ulaby, F.T. (1985). Microwave remote sensing from Space. *Proceeding of IEEE*, **73: 6**, 970−996.

CCRS (2013). Fundamentals of remote sensing. Natural Resource, Canada.

Calla, O.P.N. (2013). Applications of microwave in remote sensing. *Indian Journal of Radio and Space Physics (IJRSP)* **19**: 343−358.

Chamindi, K. (2012). Flood mapping using synthetic aperture radar in the Kelani Ganga and the Bolgoda Basins, Sri Lanka.

Dagnachew Legesse and Coulomb, C.V. (2003). Analysis of the hydrological response of a tropical terminal Lake, Lake Abiyata (Main Ethiopian Rift Valley) to changes in climate and human activities. *Hydrological Processes*, **18**: 487–504.

Daniel Alemayhu (2007). Assessment of flood risk in Dire Dawa town, Eastern Ethiopia, using GIS, Addis Ababa University, Addis Ababa. 75 pp.

Dekker, R.J. (1997). SAR change detection techniques and applications. *International Journal of Remote Sensing*, **19: 6**, 1133 –1146.

Dekker, R. J. (1998). Speckle filtering in satellite SAR change detection imagery. *International Journal of remote sensing,* **19: 7**, 1143 –1151.

Devi, R.N. and Jiji, G. (2015). Change detection techniques – a survey. *International Journal on Computational Science and Applications (IJCSA)*, **5: 2**, 45−57.

Dong, Y. Forster, B. and Ticehurst, C. (1997). Radar backscatter analysis for urban environments. *International Journal of Remote Sensing*, **18: 6**, 1351−1364.

Dong, W. Ping, Q. (2015). A Rapid method for water target extraction in SAR image. *The International Archives of the Photogrammetry, Remote Sensing and Spatial Information Sciences*. **36**: **6**, 57−63.

European Space Agency-ESA (2013). Sentinel-1 User Handbook.

Giustarini, L. (2015). Integrating remote sensing information from SAR sensors and hydraulic modelling, University of Trier.

Gedern, J. L and Huang, Y. (1996). Evaluation of several speckle filtering techniques for ERS-1and2 Imagery. *International Archives of Photogrammetry and Remote Sensing*, **31:2**, 164−168.

Gong, M., Zhou, Z. and Ma, J. (2012). Change detection in synthetic aperture radar images based on image fusion and fuzzy clustering. *International Journal of Science and Research,* **3: 5**, 201-206.

Guidelines for Soil Description (2006). Food and Agriculture Organization of the United Nations, Rome.

Hurstcalderone, S. (2016). Flood. American Geosciences Institute, Washington.

International Organization for Migration- IOM (2016). ACAPS Briefing Note: Ethiopia Floods.

Jenn, D. (2015). *Radar Fundamentals*. Monterey, California, 219 pp.

Jongman, B. and Koks, E. (2014). Increasing flood exposure in the Netherlands: implications for implications for risk financing. Natural Hazards and Earth System Sciences, VU University, Amsterdam, *Natural Hazards Earth System Sciences*, **14**: 1245−1255.

Kiema, J. B. K. (2002). Texture analysis and data fusion in the extraction of topographic objects from satellite imagery. *International Journal of Remote Sensing*, **23: 4**, 767−776.

Kher, H.R. and Hatwar, P. A. (2015). Analysis of speckle noise reduction in synthetic aperture radar images. *International Journal of Engineering Research and Technology (IJERT*), **4:1**, 508-5012.

Klemas, V. (2015). Remote sensing of floods and flood-prone areas, an overview, Coconut Creek (Florida). *Journal of Coastal Research,* **31: 4**, 1005–1013.

Krishna, T. V. Babu, A.Y. (2013). Synthetic aperture change detection. *International Journal of Computer Applications*, **78: 5**, 1−6.

Krishnama, P., Prasada, B. and Kumar, P. (2013). Image fusion on ratio images for change detection in SAR images using DWT and PCA, **3: 6**, 1242-*1246.*

Kusky andTimothy, M. (2003). Geological Hazards. A sourcebook. Greenwood Press, 341 pp.

Kussul, N., Shelestov, A. and Skakun, S. (2008). Flood monitoring from SAR data. Use of Satellite and in-situ data to improve sustainability. NATO Science for Peace and Security Series C: Environmental Security. Springer, Dordrecht, 19-25 pp.

Li, Z. and Bethel, J. (2008). Image co-registration in SAR interferometry. *The International Archives of the Photogrammetry, Remote Sensing and Spatial Information Sciences*, **36: 1**, 433−438.

Liu, C. (2016). Analysis of Sentinel-1 SAR data for mapping standing water in the Twente region, The Netherlands, 37 pp.

Long, S., Fatoyinbo, T. E. and Policelli, F. (2014). Flood extent mapping for Namibia using change detection and thresholding with SAR. *Environmental research letters*, **9**: 1−9.

Lu, D., Mausel, P., Brondízio, E. and Moran, E. (2004). Change detection techniques. *Journal of International Remote Sensing*, **25: 12**, 2365−2401.

Mansor, S., Zulhaidi, H., Shafri, M., Al-doski, J. (2013). Change detection process and techniques. *Civil and Environmental Research*, **3: 10**, 37−45.

Martinis, S. and Rieke, C. (2015). Backscatter analysis using multi-temporal and multi-frequency SAR Data in the Context of Flood Mapping at River Saale. *Journal of Remote Sensing*, **7: 5**, 7733−7752.

Mason, D. and Garcia-Pintado, J. (2014). Improving flood inundation monitoring and modeling, Chartered Institution of Civil Engineering Surveyors, University of Reading, Britain, 1-9 pp.

Mason, D. and Garcia-Pintado,J. (2015). The potential of flood forecasting using available-resolution global digital terrain model and flood extents from synthetic aperture radar images. *Frontiers in Earth Science*. **3: 43**, 46−52.

Mata, H. and Alvino, A. (2013). Impacts of natural disasters on environmental and socio economic systems: What makes the difference? Ambiente and Sociedade, São Paulo, 20 pp.

Merin, A. Imran, B. M. (2013). An efficient approach for change detection in SAR images based on contourlet fusion. *International Journal of Advanced Research in Electrical, Electronics and Instrumentation Engineering*, **2: 1**, 217−226.

Musa, Z. N. (2015). A review of applications of satellite SAR, optical, altimetry and DEM data for surface water modeling, mapping and parameter estimation.

Nizalapur, V. (2008). Land cover classification using multi-source data fusion of Envisat-ASAR and IRS P6 LISS-III satellite data, a case study over tropical moist deciduous forested regions of Karnataka, India. *The International Archives of the Photogrammetry, Remote Sensing and Spatial Information Sciences*, **36: 6**, 78−96.

O'Neill, O.P., Chauhan, N., Joseph, A., De Lannoy, G. (1996). Use of active and passive microwave remote sensing for soil moisture retrieval through a growing season. *International Journal of Remote Sensing*, **17**: 1851−1865.

Pallard, B. and Castellarin, A. (2009). A look at the links between drainage density and flood statistics. *Hydrology and Earth Systems Science*, **13**: 1019–1029.

Pradhan, B., Hagemann, U., Tehrany M.S., Prechtel, N. (2014). An easy to use Arc Map based texture analysis program for extraction of flooded areas from TerraSAR-X satellite image. *Computers and Geosciences*, **63**: 34−43.

Prasad, M. and Ravikumar, A.V. (2013). Robust technique for change detection in multitemporal synthetic aperture radar images. *International Journal of Scientific and Engineering Research*, **4: 7**, 2228−2235.

Psomiadis, E. (2016). Flash flood area mapping utilizing sentinel-1 radar data. *Earth Resources and Environmental Remote Sensing*, **5**: 1005−1051.

Raju, S., Nasir, M. and Devi, T. (2013). Filtering techniques to reduce speckle noise and image quality enhancement methods on satellite images. *Journal of Computer Engineering*, **15: 4**, 10-15.

Sandro, M., Rieke, C. (2015). Backscatter analysis using multi-temporal and multi-frequency SAR data in the context of flood mapping at River Saale. *Journal of Remote Sensing*, **7**: 7732−7752.

Santoso, A.W., Bayuaji, L., Sze, T. L., Lateh, H., Zain J. M. (2016). Comparison of various speckle noise reduction filters on synthetic aperture radar image. *International Journal of Applied Engineering Research*, **11: 15**, 8760−8767.

Sanyal, J. and LU, X. X. (2004). Application of remote sensing in flood management with special reference to monsoon Asia: A review, *Natural Hzards*, **33**: 283−301.

Sarmap (2009). Synthetic aperture radar and sarscape - SAR guidebook, 120 pp.

Schlaffer, S., Matgen P., Hollaus, M., Wagner, W. (2014). Flood detection from multi-temporal SAR data using harmonic analysis and change detection. *Journal of Applied Earth Observation and Geoinformation*, **5**: 2−33.

Sergii, S. (2010). A neural network approach to flood mapping using satellite imagery. *Journal of Computing and Informatics*, **29**: 127−136.

Shakti, G. (2013). Determination of Surface water area using multitemporal SAR imagery.

Pooja, H., Dhanushree, M. (2014). Change Detection in synthetic aperture radar image based on image fusion and fuzzy clustering. *International Journal of Science and Research*, **3: 5**, 201−206.

Sharma, S. (2006). Soil moisture estimation using active and passive microwave remote sensing techniques. Andhra University, Indian Institute of Remote Sensing, Dehradun, India, 139 pp.

Skolnik, M. I. (2008). Radar handbook. The McGraw-Hill, USA, New York, 1351 pp.

Suresh, G. and Gehrke, R. (2016). Synthetic Aperture Radar (SAR) based classifiers for land applications in Germany. *Remote Sensing and Spatial Information Sciences*, **5**: 1187–1197.

Thankachan, L.M. and Jose, J. (2014). Joint change detection and image registration method for multitemporal SAR images. *International Journal of Advances in Engineering and Technology*, **7: 3**, 765−772.

The UN Office for the Coordination of Humanitarian Affairs-OCHA (2016). ACAPS Briefing Note: Ethiopia Floods.

Toan, T. (2007). Introduction to SAR remote sensing. Advanced Training course in Land Remote Sensing, 75 pp.

Vanzyl, J. (2006). Radar Remote Sensing for Earth and Planetary Sciences, 216 pp.

Vilches, J. P. (2013). Detection of areas affected by flooding River using SAR images. Master in Space Applications for Emergency Early Warning and Response, Seminar paper, 5-27 pp.

Voigt, S., Martinis, S., Zwenzner, H., Hahmann, T., Twele, A. and Schneiderhan, T. (2008). Extraction of flood masks using satellite based very high resolution SAR data for flood management and modeling, 4th International symposium on flood defense, Toronto, Canada, 1-3 pp.

Wubet Gashaw (2007). Flood hazard and risk assessment in Fogera Woreda using GIS and Remote Sensing, Addis Ababa University, Addis Ababa, Ethiopia, 1-2 pp.

Yousif, O. (2015). Urban change detection using multitemporal SAR images. Royal Institute of Technology (KTH), Stockholm, Sweden.

http://copernicus.eu, accessed on February 03, 2017.

http://www.bbc.com/news/world-africa-36255476, accessed on December 18, 2016.

http://www.crisp.nus.edu.sg/~research/tutorial/freqpol.htm, accessed on November 25, 2016.

http://www.reuters.com/article/us-ethiopia-drought-floods-idUSKCN0Y22DH, accessed on January 06, 2017.

https://en.wikipedia.org/wiki/Drainage_density, accessed on March 16, 2017.

APPENDICES

Annex I: Sentinel-1 SAR Product Description

1) <u>March 22, 2016 reference image product description</u>

Acquisition Type: NOMINAL

Cycle number: 74

Format: SAFE

Ingestion Date: 2016-03-22T16:24:06.322Z

JTS footprint: POLYGON ((40.324085 6.777394, 38.094105 7.232562, 38.410595 8.737841, 40.649742 8.286581, 40.324085 6.777394))

Mission data take id: 63697

Orbit number (start): 10476

Orbit number (stop): 10476

Pass direction: DESCENDING

Phase identifier: 1

Polarisation: VV

Product class: S

Product class description: SAR Standard L1 Product

Product composition: Slice

Product level: L1

Product type: GRD

Relative orbit (start): 79

Relative orbit (stop): 79

Resolution: High

Sensing start: 2016-03-22T03:09:12.316Z

Sensing stop: 2016-03-22T03:09:37.315Z

Slice number: 6

Start relative orbit number: 79

Status: ARCHIVED

Stop relative orbit number: 79

Timeliness Category: Fast-24h

Carrier rocket: Soyuz

Launch date: April 3rd, 2014

Mission type: Earth observation

NSSDC identifier: 0000-000A

Operator: European Space Agency

2) April 15, 2016 flood time product description

Acquisition Type: NOMINAL

Cycle number: 76

Format: SAFE

Ingestion Date: 2016-04-15T06:10:03.450Z

JTS footprint: POLYGON (40.324875 6.777514, 38.094818 7.232753, 38.411346 8.738025, 40.650570 8.286693, 40.324875 6.777514)

Mission data take id: 66336

Orbit number (start): 10826

Orbit number (stop): 10826

Pass direction: DESCENDING

Phase identifier: 1

Polarisation: VV

Product class: S

Product class description: SAR Standard L1 Product

Product composition: Slice

Product level: L1

Product type: GRD

Relative orbit (start): 79

Relative orbit (stop): 79

Resolution: High

Sensing start: 2016-04-15T03:09:13.212Z

Sensing stop: 2016-04-15T03:09:38.211Z

Slice number: 6

Start relative orbit number: 79

Status: Archived

Stop relative orbit number: 79

Timeliness Category: Fast-24h

Carrier rocket: Soyuz

Launch date: April 3rd, 2014

Mission type: Earth observation

NSSDC identifier: 0000-000A

Operator: European Space Agency

3) <u>May 09, 2016 Flood Time Product Description</u>

Acquisition Type: NOMINAL

Cycle number: 78

Format: SAFE

Ingestion Date: 2016-05-09T06:47:26.409Z

JTS footprint: POLYGON (40.324699 6.777465, 38.094547 7.232690, 38.411053 8.737967, 40.650372 8.286649, 40.324699 6.777465)

Mission data take id: 69129

Orbit number (start): 11176

Orbit number (stop): 11176

Pass direction: DESCENDING

Phase identifier: 1

Polarisation: VV

Product class: S

Product class description: SAR Standard L1 Product

Product composition: Slice

Product level: L1

Product type: GRD

Relative orbit (start): 79

Relative orbit (stop): 79

Resolution: High

Sensing start: 2016-05-09T03:09:14.342Z

Sensing stop: 2016-05-09T03:09:39.341Z

Slice number: 6

Start relative orbit number: 79

Status: ARCHIVED

Stop relative orbit number: 79

Timeliness Category: Fast-24h

Carrier rocket: Soyuz

Launch date: April 3rd, 2014

Mission type: Earth observation

NSSDC identifier: 0000-000A

Operator: European Space Agency

Annex II: Sample points for backscatter (σ^0) of test feature classes in the study area

1) March 22, 2016 SAR image

Test classes		**Location**	
		Latitude	**Longitude**
Vegetation	test class 1	8°35’44’’	38°55’40’’
	test class 2	8°28'26"	38° 51'41"
	test class 3	8°36'10"	38°56'33"
Agricultural land	test class 1	8°20'33"	38°58'17"
	test class 2	8°20'29"	38°59'0"
	test class 3	8°19'39"	38°55'40"
Bare soil	test class 1	8°21'37"	38°55'03"
	test class 2	8°20'06"	38°55'03"
	test class 3	8°19'39"	38°53'21"
Area before flood	test class 1	8°55’20’’	38°58’39’’
	test class 2	8°23’15’’	38°57’30’’
	test class 3	8°24’18	38°56’48’’

2) April 15, 2016 SAR image

Test classes		**Location**	
		Latitude	**Longitude**
Vegetation	test class 1	8°35'44"	38°55'49"
	test class 2	8°28'26"	38° 51'41"
	test class 3	8°36'10"	38°56'33"
Agricultural land	Test class 1	8°20'33"	38°58'17"
	test class 2	8°20'29"	38°59'0"
	test class 3	8°19'39"	38°53'21"
Bare soil	test class 1	8°21'37"	38°55'03"
	test class 2	8°20'06"	38°55'03"
	test class 3	8°19'39"	38°53'21"
Area after Flood	test class 1	8°27'37"	38°59'12"
	test class 2	8°26'28"	38°57'10"
	test class 3	8°24'51"	38°55'40"

3) May 09, 2016 SAR image

Test classes		**Location**	
		Latitude	**Longitude**
Vegetation	test class 1	8^{0}35'44"	38^{0}55'49"
	test class 2	8^{0}28'26"	38^{0} 51'41"
	test class 3	8^{0}36'10"	38^{0}56'33"
Agricultural land	test class 1	8^{0}20'33"	38^{0}58'17"
	test class 2	8^{0}20'29"	38^{0}59'0"
	test class 3	8^{0}19'39"	38^{0}59'0"
Bare soil	test class 1	8^{0}21'37	38^{0}55'03"
	test class 2	8^{0}20'06"	38^{0}55'03"
	test class 3	8^{0}19'39"	38^{0}53'21"
Area after Flood	test class 1	8^{0}55'20"	38^{0}58'39"
	test class 2	8^{0}23'15"	38^{0}57'30"
	test class 3	8^{0}24'18"	38^{0}56'48"

Annex III: Land-use/cover classification accuracy assessment confusion matrix

Class Name	Reference Totals	Classified Totals	Number Correct	Producers Accuracy	Users Accuracy
Unclassified	0	0	0	---	---
	0	0	0	---	---
Agriculture	22	23	21	95.45%	91.30%
Vegetetion	6	5	5	83.33%	100.00%
Bare Land	1	1	1	100.00%	100.00%
Irrigation	8	7	6	75.00%	85.71%
Settlment	21	22	19	90.48%	86.36%
Water Body	2	2	2	100.00%	100.00%
Totals	60	60	54		

Overall Classification Accuracy = 90.00%

KAPPA (K^) STATISTICS

Overall Kappa Statistics = 0.8583

Declaration

I, hereby declare that the thesis entitled "Flood Detection and Mapping using Microwave Remote Sensing, a case study on Lake Koka catchment Awash River basin, Ethiopia" has been carried out by me under the supervision of Dr. Binyam Tesfaw, School of Earth Sciences, Addis Ababa University from the year 2016–2017 as a part of Master of Science program in Remote Sensing and Geo-informatics. I further declare that this work has not been submitted to any other University or Institution for the award of any degree or diploma.

Getu Tessema

Signature____________

Date_____________

Addis Ababa University

Certificate

This certified that the thesis entitled "Flood Detection and Mapping using Microwave Remote Sensing, a case study on Lake Koka catchment Awash River basin, Ethiopia" is an original work done by Getu Tessema Tassew for the partial fulfilment the Degree of Masters of Science in Remote Sensing and Geo-informatics under my supervision.

Dr. Binyam Tesfaw

Assistant Professor,

Signature_______________

School of Earth Science,

Addis Ababa University